https://ntrs.nasa.gov/search.jsp?R=19970014011 2020-06-16T03:00:49+00:00Z

NASA-CR-203966

021358

FINAL REPORT

SPATIAL AND TEMPORAL VARIATIONS OF SURFACE CHARACTERISTICS ON THE GREENLAND ICE SHEET AS DERIVED FROM PASSIVE MICROWAVE OBSERVATIONS

NASA GRANT NAGW-1266

January 1, 1992 - December 31, 1996

Mark Anderson, Clinton Rowe, Karl Kuivinen and Thomas Mote

Meteorology/Climatology Program
Department of Geography
University of Nebraska-Lincoln

Executive Summary

The primary goals of this research were to identify and begin to comprehend the spatial and temporal variations in surface characteristics of the Greenland ice sheet using passive microwave observations, physically-based models of the snowpack and field observations of snowpack and firn properties.

Passive microwave

To indentify surface melt using the passive microwave data a threshold value technique was developed. Varying snowpack conditions across the ice sheet do not allow the use of a single threshold value for all locations on the ice sheet. Instead, a different threshold value needs to be estimated for each location. This was accomplished by using a simple microwave emission model to simulate the brightness temperature for each grid cell assuming a 1% liquid water content in the snowpack. Melt is considered to take place when the observed 37H brightness temperature exceeds the calculated threshold value for that grid cell. Using this threshold technique, the occurrence of melt can be determined for any latitude, longitude and elevation location.

Daily, gridded SMMR and SSM/I brightness temperatures for the summers of 1979 to 1992, obtained from the National Snow and Ice Data Center were then compared to the threshold microwave brightness temperatures. The areas where observed brightness temperatures exceeded modeled values were summed to give the spatial extent of melt on a daily basis. The values were averaged on monthly and seasonal (May through August) bases. For comparison between the SMMR and SSM/I data sets the modeled results were adjusted to account for calibration and view angle differences between the two sensors. A comparison of the overlap period (July and August 1987) showed only a 1.2 percent difference in the mean melt area detected by the two sensors. The total area classified with at least one day of melt for the 13 year period was then used to produce a map of frequency of melt. This map compares favorably with previous maps of the percolation and ablation zones. The mean melt frequency map shows that melt occurs below 3000 masl in the south to approximately 2400 masl in the northwest. Along the western margin, greater than 50 percent of the days had melt, while in the southeast the frequency dropped to 30 percent. Only a few locations in the north had more than 20 percent of the days experiencing melt.

The annual areal melt extent was also calculated. This was accomplished by summing the area of the grid cells identified as undergoing melt for each day throughout a season. Melt generally begins in early to mid May, with maximum coverage during late July and rapidly decreasing until only intermittent melt occurs in late August. The period from initial melt to maximum extent for each year is much longer than the period from maximum melt to the end of the melt season. Large variations exist between the years, for example, 1988 through 1990 have a larger spatial coverage of melt than 1980 or 1982.

Daily melt extent values were then averaged into monthly and seasonal melt extents for the entire ice sheet. The most striking feature of the seasonal melt extent time series is an apparent trend toward increasing area of average daily surface melt extent. This trend is significant at the 95 percent confidence interval.

Melt extent has also been examined on monthly time scales. The results show that July has the largest monthly melt extent. June, July and August all have large interannual variability. As was shown for the seasonal analysis, all four months also exhibit an increase in melt over the period 1979-1992. The most substantial increases occur in July and August.

Once the threshold technique had been applied to determine melt for the entire ice sheet, an investigation was conducted to determine regional variability of the extent of melt on the surface on the ice sheet for both seasonal and monthly time scales. The ice sheet was divided into eight topographic regions. The southwestern regions have had a statistically significant increase in melt area while the regions to the north and southeast do not show statistically significant trends. In fact, the northeast region had a slight decrease in melt extent over the time period analyzed, although it is not statistically significant.

Snowpack modeling

SNTHERM, a one-dimensional energy and mass balance model developed at CRREL (Jordan, 1991, CRREL Report 91-16), was modified for use with snowpacks over ice. This model uses meteorological data and appropriate values for the surface properties to estimate the fluxes of shortwave and longwave radiation at the surface, sensible and latent heat transfers between the surface and the atmosphere, and the transfer of sensible heat into the snowpack. In addition, the profiles of temperature, density, grain size, thermal conductivity, specific heat, and liquid water content of the snowpack are estimated as the snowpack undergoes metamorphosis over time.

Preliminary simulations were made using meteorological and snowpack data collected during the summer of 1990 at the ETH camp near the equilibrium line on the west slope of the Greenland ice sheet. A subset of the data was extracted from the ETH data set to test the snowmelt model. Because the SNTHERM model assumes a constant snow albedo, the average albedo specified is initially too low, then becomes too high for the final portion of the simulation. This corresponds to the errors in the modeled mass balance, with mass being lost too quickly at the beginning of the run (i.e., absorption of solar radiation too high) and too slowly at the end of the run. To overcome this problem, the SNTHERM model was modified to use observed daily albedo. This modification resulted in better overall agreement with the observed snowpack height during the simulation period.

Simulations from the modified SNTHERM model can be used to compute, for example, the onset and rate of snowmelt. Since the emissivities of snow and liquid water are significantly different, especially in the microwave, these simulations can be used to help explain much of the temporal and spatial variation observed in brightness temperature by passive microwave techniques. In an attempt to address this part of our research, we collected the neccessary input data for the model during the 1993 field season and obtained microwave radiometric data for the same period. Meteorological observations were taken at Dye 2 during 10 June to 13 July 1993. The measurements included hourly values of surface air temperature, snowpack temperatures (to a depth of 2m), humidity, wind direction and speed, incoming and reflected shortwave radiation, and downwelling longwave radiation. These data were used to drive SNTHERM for the period of 21 June to 13 July, producing hourly time series that included, but were not limited to, depth profiles of temperature, liquid

water content, and snow density. Microwave radiometric data were obtained for June and July, 1993, from the SSM/I sensor aboard the DMSP F-11 satellite.

The time series of 37H brightness temperatures was compared to SNTHERM output of liquid water content averaged over the top 2 cm and the top 10 cm of the snowpack. These layers were selected because the model results indicate that liquid water often first appears 1-3 cm below the surface of the snowpack when the air temperature is below 0°C. This is due to radiation penetration into the snowpack and the evaporation of liquid water closer to the surface. As the model begins to indicate increased concentrations of liquid water, water becomes evident nearer to the surface and begins to percolate deeper into the snowpack. On several occasions during the time period simulated by the model, afternoon observations of the 37H brightness temperatures for exceed the threshold value of 201.1K that is associated with onset of snow melt for Dye 2. The average volumetric liquid water content in the upper 2 cm of the snowpack, as given by the model, shows the occurrence of melt during these afternoons. On several days, the liquid water content of the upper 2 cm of the snowpack during the time of the afternoon SSM/I overpass was greater than 6 percent.

Diurnal melt-freeze cycles that occurred during the field season are evident both by an increase in the microwave brightness temperatures and also from the formation of liquid water as shown in the model output. Additionally, the effects of melt-freeze metamorphosis of the snow and new snow accumulation are evident in the brightness temperature time series. These time series demonstrate that a brightness temperature threshold for a single channel of microwave data can be used for melt identification, particularly if other geophysical characteristics of the snowpack are also considered.

Field observations

As part of the field program during the summer of 1993, several shallow firn cores from two locations in the southern region of the Greenland ice sheet were obtained. In the field, the shallow firn cores were examined for stratigraphic evidence of past melt events. Next, each core was divided every 5cm along the length of the core into samples for density and later oxygen isotope analysis to delineate the annual accumulation layers in the snowpack. The relative intensity of each year's summer melt episode was compared to the corresponding melt frequency derived from microwave emissions. This comparison demonstrates that a linkage between the stratigraphic record and microwave data can be established. Both data sets indicate that there was less melt during the late 1970s and early 1980s than during the late 1980s, in general agreement with climate observations.

Summary

The purpose of our research project was to establish a better understanding of the timing and extent of surface snowmelt occurring on the Greenland ice sheet. Using passive microwave observation, computer models and field measurements, we have been able to increase out knowledge of snowpack characteristics during melt and our understanding of the temporal and spatial variations in snowmelt that take place over the Greenland ice sheet. In addition, the knowledge gained from this study has been applied to observations of snowmelt on sea ice and to deeper ice cores taken from the Greenland ice sheet.

ACCEPTED IN
ANNALS OF GLACIOLOGY

Determination of a melt onset date for Arctic sea ice regions using passive microwave data.

Mark R. Anderson
324 Avery Hall
Department of Geography
University of Nebraska-Lincoln
Lincoln, NE, USA 68588-0135
(402) 472-6656
(402) 472-1185 fax
mra@unlinfo.unl.edu

Abstract

Although the formation and melt of sea ice are primarily functions of the annual radiation cycle, atmospheric sensible heat forcing does serve to delay or advance the timing of such events. Additionally, if atmospheric conditions in the Arctic were to vary due to climate change it may have significant influence on ice conditions. Therefore, this paper investigates a methodology to determine melt onset date distribution, both spatially and temporally, in the Arctic Ocean and surrounding sea ice covered regions.

Melt determination is made by a threshold technique utilizing the spectral signatures of the horizontal brightness temperatures (19Ghz horizontal channel minus the 37Ghz horizontal channel) obtained from the Special Sensor Microwave Imager (SSM/I) passive microwave sensor. Passive microwave observations are used to identify melt because of the large increase in emissivity that occurs when liquid water is present. Emissivity variations are observed in the brightness temperatures due to the different scattering, absorption, and penetration depths of the snowpack from the available satellite channels during melt.

Monitoring the variations in the brightness temperatures allows the determination of melt onset dates.

Analysis of daily brightness temperature data allows spatial variations in the date of the snowmelt onset for sea ice to be detected. Since the data are gridded on a daily basis, a climatology of daily melt onset dates can be produced for the Arctic region. From this climatology, progression of melt can be obtained and compared interannually.

INTRODUCTION

Scientific interest in the potential effects of climate change on the polar regions has increased since computer simulations have shown that high latitudes are likely to experience enhanced warming. The response of sea ice regions to a projected warming has been of particular interest. To decide how snowmelt on the sea ice responds to climate variations, surface snowmelt must be examined. This project is a new approach to determine the date of snowmelt onset for the Arctic sea ice region using passive microwave data from Special Sensor Microwave Imager (SSM/I) platform. Previous work has shown strong variations in the date of the onset of snowmelt on sea ice from passive microwave remote sensing (Anderson et al.,1985, Anderson, 1987a,b) for different locations and from year to year. More recent research using similar passive microwave techniques on the Greenland ice sheet has determined variations in the date of melt onset and spatial coverage of the melting snowcover (Abdalati and

Steffen, 1995 and Mote and Anderson, 1995). Results from these studies are used here to produce a new algorithm that detects the onset date of snowmelt on sea ice. This is possible because of the large increase in emissivity that occurs when liquid water is present in the snowpack. The algorithm is suited for the entire Arctic basin since it works regardless of ice type (ice type was found to be an important factor in detecting melt). Melt onset is correlated with albedo changes. A better understanding of the albedo changes during the early spring and summer will allow computer models to better estimate surface energy balances.

ALGORITHM DEVELOPMENT

Several locations in the Arctic basin, including first-year and multiyear ice regions (Table 1) were used to develop an algorithm that would represent the onset date of snowmelt. These locations are the same as used in previous research (Anderson et al.,1985, Anderson, 1987a,b) allowing comparison with prior results. To develop an algorithm, SSM/I passive microwave brightness temperature(TB) data were obtained from the National Snow and Ice Data Center (NSIDC). These data are gridded into 25 km X 25 km grid cells and archived on CD-ROM. In the development of the algorithm, time series of the brightness temperatures were analyzed, however, an algorithm was not developed solely using an individual passive microwave channel. For example, the algorithm that detects melt onset on the Greenland ice sheet using a 37 GHz horizontal brightness temperature threshold technique (Mote and

Anderson, 1995), could not be used because sea ice brightness temperatures vary too much due to the presence of different ice types and open water. In contrast, on the Greenland ice sheet, the snowcover is thick enough that brightness temperature signatures are of snow only and do not reflect the underlying surface.

Time series of total ice (TI) and multiyear ice fraction (MYI), calculated using the NASA Team Algorithm (Cavalieri et al, 1984), were also examined to detect the onset of melt. As previous research has shown (Anderson et al.,1985, Anderson, 1987a,b) monitoring these parameters gives an indication of melt onset dates, however, advection of different ice types into the location might give similar results. Therefore, use of TI and MYI would help define melt onset, but would not be used in a new algorithm.

Several different published ratios as well as a new ratio were calculated to assist in detecting the melt onset date. For example, the polarization ratio (PR) and gradient ratio (GR) from the NASA Team sea ice concentration algorithm (Cavalieri et al, 1984) were examined. The expressions for PR and GR are:

$$PR = [TB(19V)-TB(19H)] \,/\, [TB(19V)+TB(19H)] \qquad (1)$$

$$GR = [TB(37V)-TB(19H)] \,/\, [TB(37V)+TB(19H)] \qquad (2)$$

Analysis of the PR and GR time series showed that these ratios were sea ice type dependent In addition, the cross polarization gradient ratio (XPGR) used by Abdalati and Steffen(1995)to show melt on the Greenland ice sheet was also investigated. The XPGR is defined by:

$$XPGR = [TB(19H)-TB(37V)] / [TB(19H)+TB(37V)] \quad (3)$$

The XPGR reduces the dependence of the spatial variability of physical temperatures compared to the single channel approach of Mote and Anderson (1995), however, the XPGR algorithm when applied to sea ice, was also found to be ice type dependent. These factors were determined to be important deficiencies, therefore these ratio algorithms were not pursued in the new algorithm development. Another ratio was calculated using the difference between the horizontal channels 37 and 19 GHz (XHGR) given by:

$$XHGR = [TB(37H)-TB(19H)] / [TB(37H)+TB(19H)] \quad (4)$$

Similar results were found for the XHGR as were observed with the XPGR algorithm: the XHGR was dependent on ice type.

For all of these passive microwave methods, it was fairly easy to determine visually the onset of melt because the parameters would start behaving differently. A threshold value for each technique could be set that determined melt onset,

allowing the process to be automated. However, the problem with these techniques and their thresholds was that sea ice type was needed to determine the direction of the parameter change.

The original brightness temperature time series were scrutinized further to determine if other relationships could be observed in the data that might suggest the melt onset and not be dependent on the sea ice type. A new melt algorithm using the difference between the 19 GHz and 37 GHz horizontally polarized channel (HG algorithm) was generated and is given by the following:

$$HR = TB(19H) - TB(37H) \tag{5}$$

The horizontal channels reflect a strong dependence on snow conditions during melt. Rapid changes in snow conditions are observed in the brightness temperatures. During melt conditions, the brightness temperatures first increase from liquid water within the snowpack, then a decrease occurs because of freeze/thaw cycles increasing the snow grain size (i.e. Matzler, 1987; Onset et al., 1987), allowing the HG algorithm to detect these variations.

A single threshold value was determined by examining regions in the Arctic basin (Table 1) for three years (1989-1991) when the HG algorithm exhibited a change in the brightness temperatures. Time series of the brightness temperatures, TI and MYI concentrations, various ratios and the HG algorithm were

analyzed for all sites. However, only two locations representing different ice types will be discussed. These two sites were chosen because they represent locations were variations with the algorithm existed and could be analyzed, compared to other sites where the algorithm was more consistent in determining the melt onset date. The first location is a first-year ice region located in the Laptev Sea. The three time series for this location shows general trends in brightness temperatures and ice concentrations that would be expected during the late winter through summer for a first-year ice region (Fig. 1-3). The brightness temperatures for all four channels (19 H,V and 37 H,V) average near 250 K during the winter period with little separation between horizontal and vertical channels. After a spring/summer melt period where brightness temperatures vary greatly, the temperatures are indicative of open water conditions (i.e. Cavalieri et al., 1984). This is observed in all three years, though large variations take place in the timing of the melt periods. The ice concentrations and ratios also exhibit variations during the melt period. The HG algorithm (top plot in Fig. 1-3) shows that during the winter period before melt takes place, the difference between the 19 and 37 GHz channels is fairly consistent between 4-7 K. Once melt takes' place the variations in the difference become quite large. However, in all three years the initial change was to increase the 37H GHz brightness temperatures, resulting in a decrease in the HG values.

Similar patterns were found for multiyear ice locations. For discussion purposes, one site will only be presented, although others were analyzed. The site, a multiyear ice location found in the central Arctic Ocean (seventh site, Table 1), also exhibits general seasonal trends in the parameters for the three years (Fig. 4-6). The brightness temperatures exhibit three distinct periods: winter conditions, with generally consistent temperatures, a melt period, where large variations are observed, followed by summer conditions, before returning to winter conditions. The multiyear ice concentrations and various ratios (PR, GR, XPGR, and XHGR) also exhibit fluctuations during the melt period. The HG algorithm also shows variations in the brightness temperature difference taking place during melt. The HG temperature variations are larger than the ones observed for the first-year ice regions (Fig. 1-3).

Using all sites (Table 1) it was determined that a melt threshold would be assigned when the HG was less than or equal to 2K with ice concentrations greater than 15%. When snowmelt takes place the snowcover should become nearly a perfect blackbody emitter and the difference between the 19 GHz and 37 Ghz channels should be very small. A 2K threshold was chosen because of the large SSM/I grid size and inhomogenties within any grid.

To help determine whether the HG algorithm is detecting the onset of melt, air temperatures have been obtained from the Polar Exchange at the Sea Surface (POLES) data set. The POLES temperature data are derived from Arctic buoy data, AVHRR surface

temperatures and land observations and averaged over a 24 hour period to correspond to the microwave data. When comparing the HG algorithm's determination of the melt onset date with the nearest grid point of the POLES temperature data, there is a strong association. The HG algorithm indicates melt onset when the POLES data approaches or reaches the freezing point (Fig. 1-6). The best relationships between the air temperature and HG algorithm are for the multiyear ice location. It should be noted that multiyear ice locations might be better depicted by the POLES data because of the way the air temperatures are generated. The POLES data are a combination of buoy, satellite and land surface observations. POLES temperatures are not as reliable for first-year ice regions, generally located along the coastline, since land surface temperature observations included in the calculation may not be representative of sea ice conditions (J. Maslanik, per comm, 1996).

Generally speaking, whenever a global threshold is applied to a data set, there will be times and locations when a single threshold will not represent all situations. For example, at the first year ice location discussed (Fig. 1-3) the HG threshold captures the start of the melt period two out of the three years (1990 and 1991). In the third year (1989), the HG algorithm indicates the melt onset while the temperatures are still well below freezing. However, there is an increase in the POLES temperature during that period, although the air temperatures do not approach the freezing point as closely as in the other years.

In 1991, the HG algorithm produces a melt onset that appears too early. The algorithm indicates melt, but the other microwave parameters do not display melt characteristics until later in time. The POLES air temperatures show a fairly strong increase in temperature during that time period, however the air temperatures are still below freezing. The discrepancies between the HG algorithm and the POLES air temperatures may be in the way the air temperatures are calculated, not representing the sea ice conditions.

The HG algorithm also captures melt two out of three years for the multiyear site (Fig. 4-6) compared to the POLES air temperatures. In this case, an earlier melt onset is missed in 1989 by the HG algorithm. The time series in 1989 shows a distinct melt event that the HG temperature difference did not meet or exceed the chosen threshold while air temperatures are very close to freezing. In the other two years, the HG algorithm indicates the melt onset when the air temperatures would also indicate melting in the snowpack.

To determine if these missed years could be detected better by the HG algorithm, the HG melt threshold was varied. If the threshold was increased (raised to 3 and then 4 K) the first-year ice locations usually showed earlier melt onset dates on the order of several weeks to months, although melt conditions were not observed in the other microwave parameters and considered not to have taken place. The earlier melt onset dates were indicated by HG algorithm because first-year ice regions usually varied

between 3 to 7 K throughout the winter. Increasing the threshold does not differentiate melt occurrences from winter conditions at the first-year ice location. When the HG threshold was increased for the multiyear ice location, an earlier melt date was also indicated, but only in 1989 (Fig. 4). In this case, the earlier melt onset date was probably justified. The HG threshold was also decreased (1 K) to determine a lower sensitivity. Very little variation was observed in the melt onset dates for the sites analyzed compared to the 2K value, since the 37 H GHz brightness temperatures was observed to became larger than the 19H Ghz brightness temperatures during melt episodes, producing a negative HG value. If there was a difference in onset date, the onset date was usually delayed only a day or two. In summary, increasing the threshold mainly affected first-year regions in a negative manner, although it might slightly benefit the multiyear location. Decreasing the threshold had little effect on onset dates for either ice type location. Therefore, to maintain a global threshold independent of ice type, the 2K threshold was retained.

Using the 2K threshold, dates of initial melt onset for the entire Arctic basin were produced from the three-year data set by the HG algorithm to show the spatial distribution of melt (Fig. 7). Several generalizations can be made from this analysis. The first shows the substantial nature of the algorithm. In each year, the melt onset dates are spatially consistent and show the poleward progression of melt taking place from the southern

first-year ice locations to later multiyear locations. However, linear features were observed for several locations among the years analyzed. These were further explored to determine a cause for the linear nature of the dates. For example, one of these features is located along the 135th meridian from the pole to the coast in 1991 (Fig 9). At several locations along this linear feature, perpendicular transects were made to analyze the melt onset dates and their brightness temperature time series. Examining the grid cells on either side of the linear feature, it was easy to determine why the feature existed. The grid cells to the west of the feature (later onset dates) exhibited changes in the brightness temperatures but these did not surpass the HG threshold criteria. It was not due to missing data, but to the region not meeting the HG threshold. Similar situations where found for the other years examined. The other major generalization would be that the HG algorithm is consistent from year to year in its determination of melt onset dates for the entire basin. There are small variations within regions between the years analyzed, but this would be expected.

The spatial analysis also demonstrates, however, that at many locations in the ocean region that do not have an ice cover, the algorithm still analyzed a melt date. These points usually south of 60 degrees need to be filtered and removed from the data set. It was originally thought that these points were removed through weather filters applied to the concentration data set before the HG algorithm was applied. However, the spatial

analysis gives a different picture. New filters will have to be developed and applied to insure an accurate melt data set in the open ocean regions.

To show that the variation in the threshold was mainly a first-year ice problem and not a result of the initial locations investigated, spatial maps of the Arctic basin were produced using the different threshold values for the three years studied. The first-year ice region onset dates were generally the most affected by the variation in the threshold value. In summary, using a global threshold value will not always give the most accurate response for all locations. However, using the 2K threshold appears to be the best value for the entire Arctic basin.

MELT ONSET VARIABILITY

To show the capabilities of the melt algorithm to produce a melt climatology, the two example sites will be further discussed although other locations have been investigated (Table 1). Again, these sites were chosen because they represent both first-year and multiyear ice conditions. The analysis was completed for three years, 1989-1991. The HG algorithm determined that the initial melt occurred between Julian days 123 thru 134 for the three years (Table 1 and Fig 1-3), an 11-day variation among the the years.

The time series for the multiyear ice location, found in the central Arctic Ocean (seventh site Table 1), shows similar

results (Fig. 4-6). The initial melt occurrences showed a greater range than at the first-year ice location. The HG algorithm indicated that melt occurred between Julian day 138 and 174, a 36-day variation among the three years analyzed.

It can be assumed that the actual range in dates among years for most locations is relatively small, although variations do exist. Again, this would enhance the current thinking that melt occurrence in the Arctic basin is mainly regulated by the radiational changes that take place in the Arctic throughout the spring period. However, the variations in initial date for each location are going to be driven by local annual variations controlling the amount of solar radiation received and the atmospheric sensible heat advected into the region to initiate melt.

SUMMARY

A study was launched to develop a new melt algorithm that would detect the onset of melt for the entire Arctic sea ice basin with no dependence on ice type. The HG melt algorithm developed produces initial melt onset dates when sea ice snowpack begins to show melt in the passive microwave remotely sensed data. The melt algorithm was then applied to three years of data to show the nature of the algorithm for different ice type locations. The results from this investigation show that the entire passive microwave brightness temperature data set can be analyzed to produce a melt onset date climatology. The

climatology can be derived from passive microwave brightness temperatures from SMMR and other SSM/I platforms. Once the climatology is produced, a more complete understanding of the relationships between the atmospheric effects and the ice conditions, especially considering modeled climate variations, can be investigated.

REFERENCES

Abdalati, W. and K. Steffen, 1995: Passive microwave-derived snow melt regions on the Greenland ice sheet. *Geophy. Res. Let.*, 22(7), 787-790.

Anderson, M.R., R.G. Crane and R.G. Barry, 1985: Characteristics of Arctic Ocean ice determined from SMMR data for 1979: Case studies in the seasonal sea ice zone. *Advances in Space Research*, 257-261.

Anderson, M.R., 1987a: The onset of spring melt in first-year ice regions of the Arctic as determined from SMMR data for 1979 and 1980. *J. of Geophyl Res*, 13,153-13,163.

Anderson, M.R., 1987b: Snow melt on sea ice surfaces as determined from passive microwave satellite data. *Large Scale Effects of Seasonal Snow Cover*, edited by B.E. Goodison, R.G. Barry and J. Dozier, IAHS Publication No. 166, 329-352.

Cavalieri, D., P. Gloersen, and W.J. Campbell, 1984: Determination of sea ice parameters with Nimbus-7 SMMR. *J. of Geophyl Res*, 88, 5355-5369.

Matzler, C., 1987: Applications of the interaction of microwaves with the natural snow cover. *Remote Sensing Rev.*, 2(2), 259-387.

Mote, T.L. and M.R. Anderson, 1995: Variations in snowpack melt on the Greenland ice sheet based on passive microwave measurements. *J. of Glaciol.*, 41(137), 51-60.

Onstott, R.G., T.C. Greenfell, C. Matzler, C. A. Luther, and E.A.

Svendsen, 1987: Evolution of microwave sea ice signatures during early summer and midsummer in the marginal ice zone. *J. of Geophyl Res*, 92, 6825-6835.

ACKNOWLEDGMENTS

I would like to thank the two anonymous reviewers for their helpful suggestions and comments. I would also like to thank Jim Maslanik for supplying the 24 hour averaged POLES temperature data. The original POLES data were obtained from the Polar Science Center, University of Washington, Seattle, WA. The SSM/I gridded brightness temperatures obtained on CD-ROM were from the National Snow and Ice Data Center, Boulder, CO. This work was supported at the University of Nebraska by NASA grant NAGW-1266 and by NASA contract NAS-5-32392 to the University of Colorado.

Table 1
Location sites and melt onset dates

Pt	i,j	Lat	Long	Location	Melt Onset Date		
					1989	1990	1991
1	154,160	72 N	135 E	Laptev Sea (FYI)	134	123	129
2	113,163	71 N	165 E	East Siberian Sea (FYI)	99	92*	91*
3	85,174	69 N	176 W	Chukchi Sea (FYI)	141	101	142
4	80,188	70 N	167 W	Chukchi Sea (FYI)	96	115	111
5	160,193	80 N	120 E	Laptev Sea (MYI)	169	149	147
6	230,212	72 N	62 E	Barents Sea (FYI)	104	103	98
7	132,213	83 N	180 E	Arctic Ocean(MYI)	174	138	158
8	132,214	83 N	177 W	Arctic Ocean(MYI)	174	138	185
9	124,234	83 N	136 W	Arctic Ocean(MYI)	173	157	186
10	132,319	70 N	60 W	Baffin Bay (FYI)	108	115	122
11	65,330	60.5N	88 W	Hudson Bay (FYI)	104	93	97*
12	66,340	59 N	85 W	Hudson Bay (FYI)	117	92*	111
13	65,351	57 N	82.5W	Hudson Bay (FYI)	134	93*	111
					* First date of analysis		

FIGURE CAPTIONS

Figure 1. Time series analysis for a first-year ice location in the Laptev Sea (72 N,135 E) for 1989. The triangle shape represents the onset of melt as detected by the HR melt algorithm.

Figure 2. Same as Fig. 1 except for 1990.

Figure 3. Same as Fig. 1 except for 1991.

Figure 4. Time series analysis for a multiyear ice location in the central Arctic Ocean (83 N,180 W) for 1989. The triangle shape represents the onset of melt as detected by the HR melt algorithm.

Figure 5. Same as Fig. 4 except for 1990.

Figure 6. Same as Fig. 4 except for 1991.

Figure 7. Initial melt onset dates as detected by the HR melt algorithm for (a) 1989, (b) 1990, and (c) 1991.

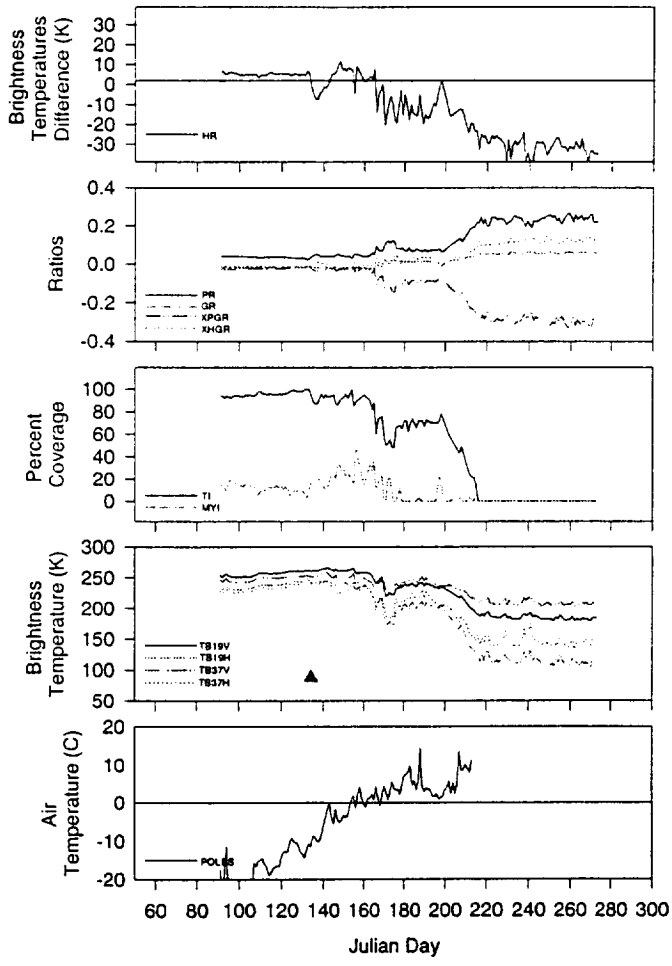
Brightness Temperatures Difference (K)
30
20
10
0
-10
-20
-30
HR
Ratios
0.4
0.2
0.0
-0.2
-0.4
PR
GR
XPGR
XHGR
Percent Coverage
100
80
60
40
20
0
FI
MYI
Brightness Temperature (K)
300
250
200
150
100
50
TB19V
TB19H
TB37V
TB37H
Air Temperature (C)
20
10
0
-10
-20
POLES
60 80 100 120 140 160 180 200 220 240 260 280 300
Julian Day

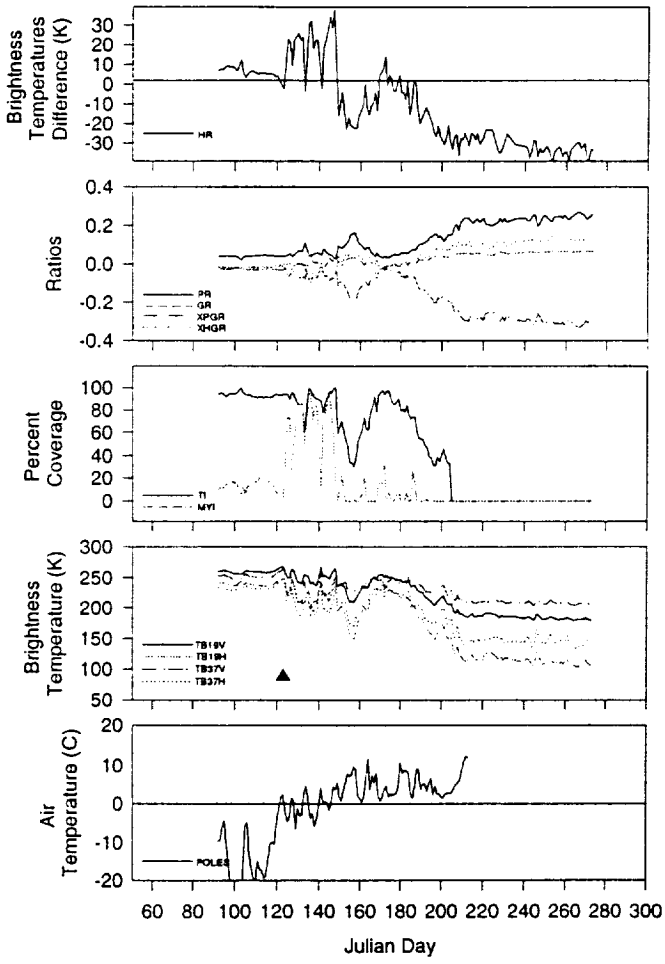
Brightness Temperatures Difference (K)
30
20
10
0
-10
-20
-30
HR
Ratios
0.4
0.2
0.0
-0.2
-0.4
PR
GR
XPGR
XHGR
Percent Coverage
100
80
60
40
20
0
FI
MYI
Brightness Temperature (K)
300
250
200
150
100
50
TB19V
TB19H
TB37V
TB37H
Air Temperature (C)
20
10
0
-10
-20
POLES
60 80 100 120 140 160 180 200 220 240 260 280 300
Julian Day

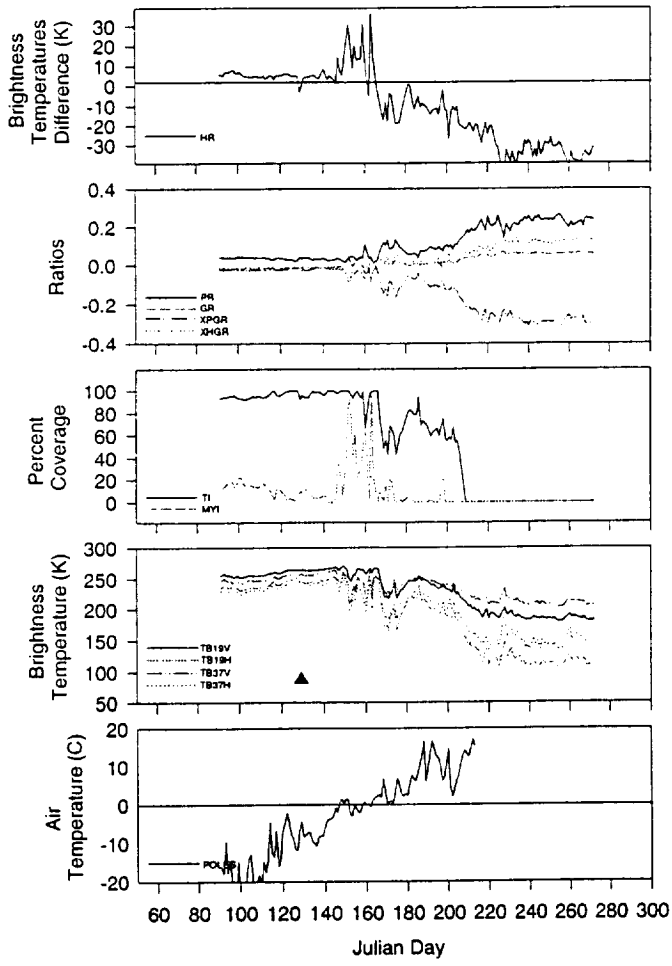
Brightness Temperatures Difference (K)
30
20
10
0
-10
-20
-30
HR
Ratios
0.4
0.2
0.0
-0.2
-0.4
PR
GR
XPGR
XHGR
Percent Coverage
100
80
60
40
20
0
FI
MYI
Brightness Temperature (K)
300
250
200
150
100
50
TB19V
TB19H
TB37V
TB37H
Air Temperature (C)
20
10
0
-10
-20
60 80 100 120 140 160 180 200 220 240 260 280 300
Julian Day

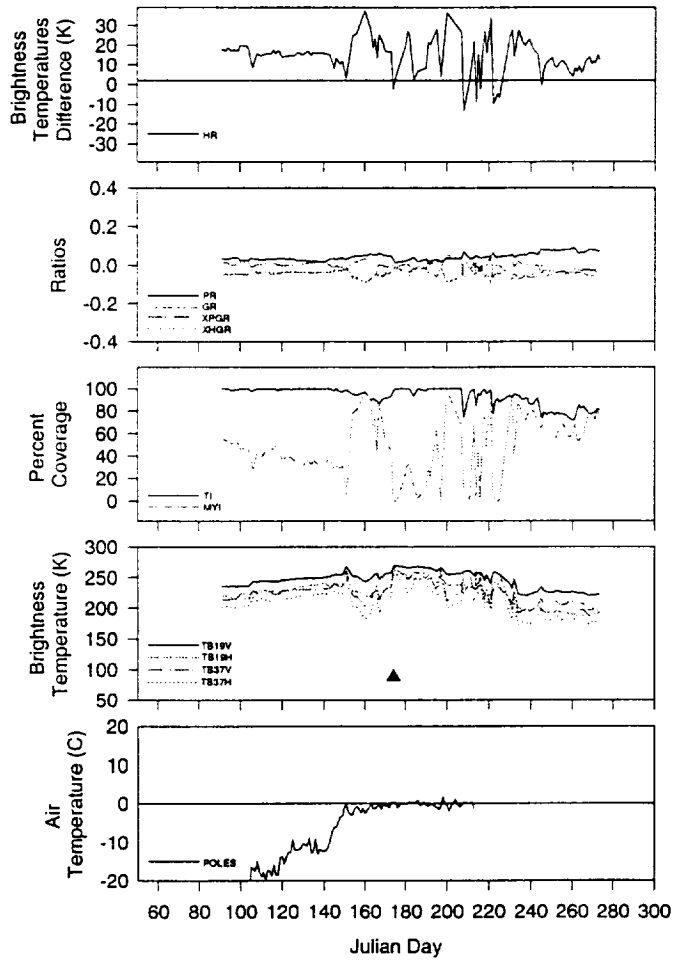
Brightness Temperatures Difference (K)
30
20
10
0
-10
-20
-30
HR
Ratios
0.4
0.2
0.0
-0.2
-0.4
PR
GR
XPGR
XHGR
Percent Coverage
100
80
60
40
20
0
FI
MYI
Brightness Temperature (K)
300
250
200
150
100
50
TB19V
TB19H
TB37V
TB37H
Air Temperature (C)
20
10
0
-10
-20
POLES
60 80 100 120 140 160 180 200 220 240 260 280 300
Julian Day

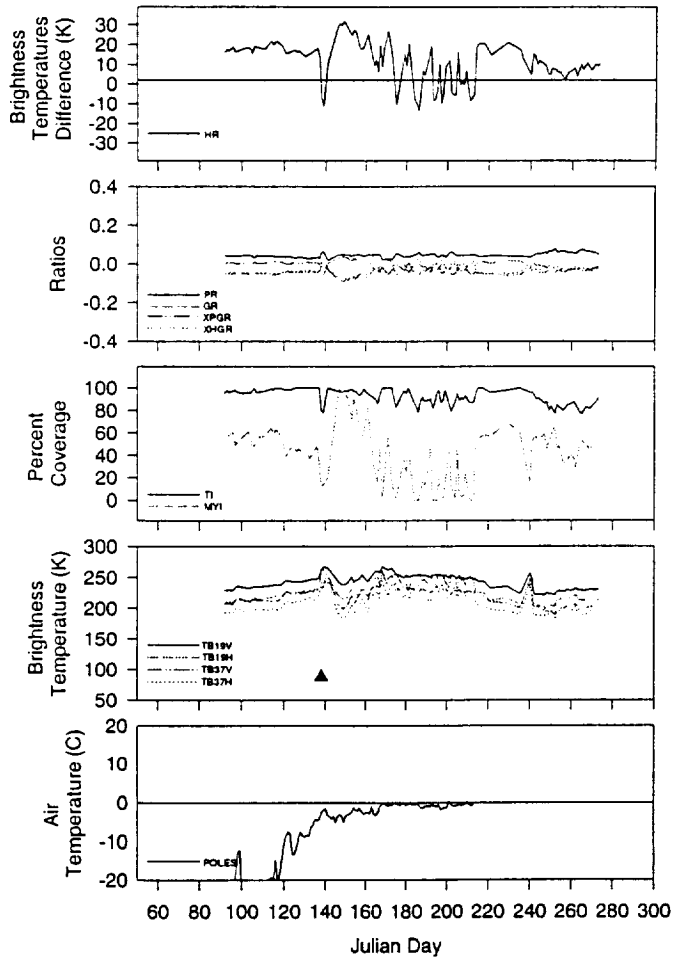
Brightness Temperatures Difference (K)
30
20
10
0
-10
-20
-30
HR
Ratios
0.4
0.2
0.0
-0.2
-0.4
PR
GR
XPGR
XHGR
Percent Coverage
100
80
60
40
20
0
FI
MYI
Brightness Temperature (K)
300
250
200
150
100
50
TB19V
TB19H
TB37V
TB37H
Air Temperature (C)
20
10
0
-10
-20
POLES
60 80 100 120 140 160 180 200 220 240 260 280 300
Julian Day

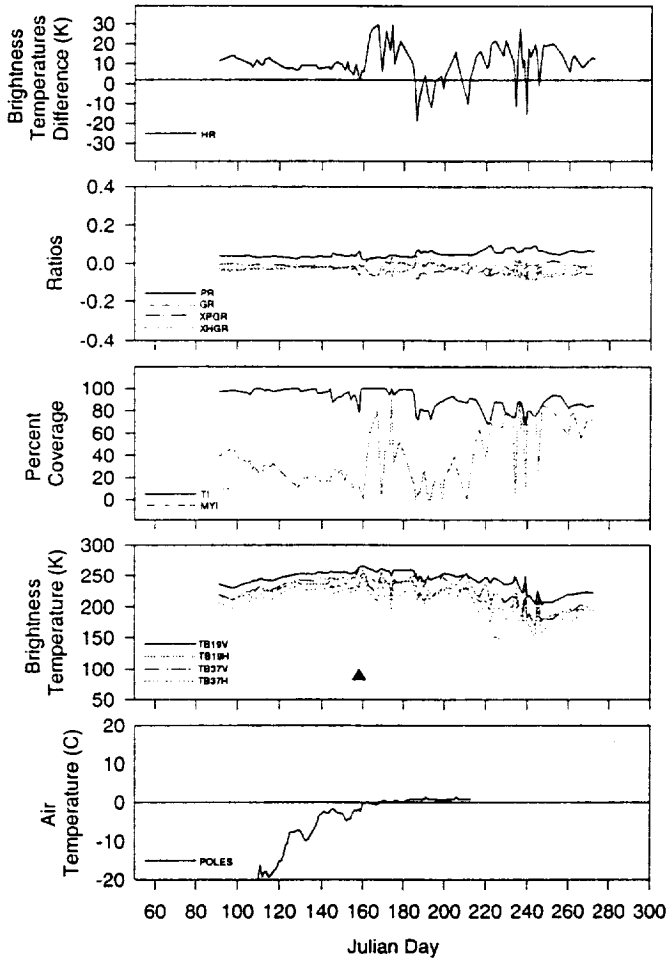
Brightness Temperatures Difference (K)
30
20
10
0
-10
-20
-30
HR
Ratios
0.4
0.2
0.0
-0.2
-0.4
PR
GR
XPGR
XHGR
Percent Coverage
100
80
60
40
20
0
TI
MYI
Brightness Temperature (K)
300
250
200
150
100
50
TB19V
TB19H
TB37V
TB37H
Air Temperature (C)
20
10
0
-10
-20
POLES
60 80 100 120 140 160 180 200 220 240 260 280 300
Julian Day

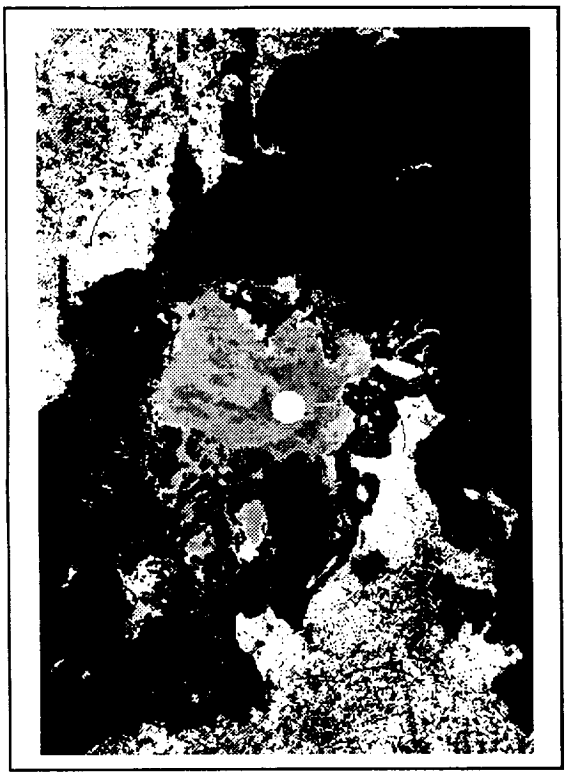

a. 1989

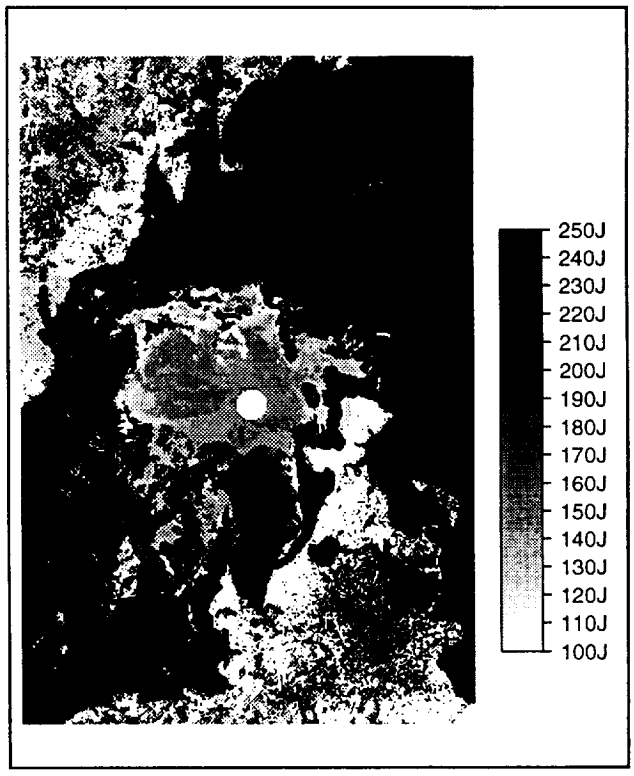

c. 1991

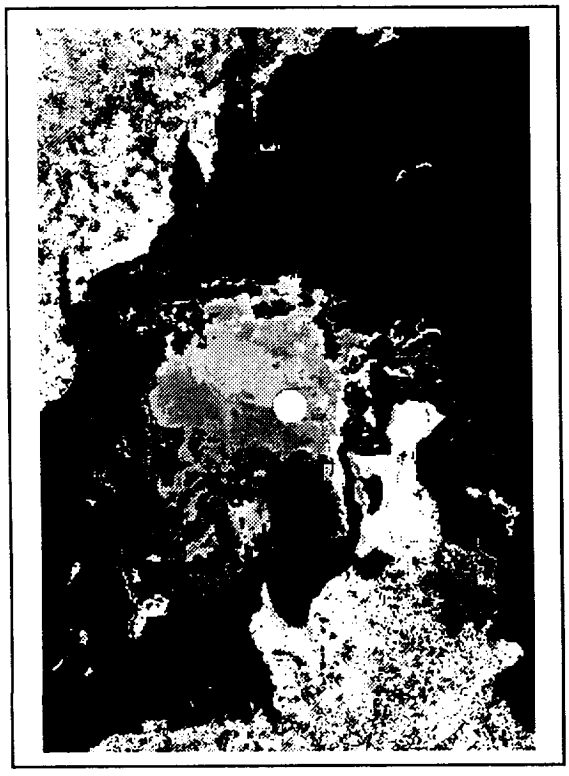

b. 1990

Meteorol. Atmos. Phys. 59, 245–255 (1996)

Meteorology and Atmospheric Physics

© Springer-Verlag 1996
Printed in Austria

[1] Department of Geography, University of Georgia, Athens, Georgia, U.S.A.
[2] Program in Meteorology/Climatology, Department of Geography, University of Nebraska-Lincoln, Lincoln, Nebraska, U.S.A.

A Comparison of Microwave Radiometric Data and Modeled Snowpack Conditions for Dye 2, Greenland

T. L. Mote[1] and C. M. Rowe[2]

With 4 Figures

Received September 23, 1994
Revised April 30, 1995

Summary

Meteorological observations were recorded at Dye 2, Greenland, during the summer of 1993 as part of a research program to identify interannual variations in melt occurrence on the Greenland ice sheet from satellite microwave data. The meteorological observations were used to drive an energy-balance model of the snowpack during 21 June to 13 July 1993. Time series of the meteorological observations and various model outputs were compared to a concurrent time series of Special Sensor Microwave/Imager (SSM/I) data for scan cells centered within 25 km of Dye 2. The satellite microwave observations clearly show an increase in snowpack emissivity at the same time that the model indicates liquid water forming in the snow. Diurnal melt-freeze cycles that occurred during mid June to early July resulted in an increase in the 37 GHz brightness temperature as great as 60 K from the dry, refrozen snow in the morning to the wet snow of some afternoons. The effects of fresh snowfall, which tend to increase the brightness temperature, and of snow growth from melt-freeze metamorphism, which tend to decrease the brightness temperature, are also apparent in the microwave observations. The results of this work demonstrate the influence of daily weather variations on the microwave emissivity in the ice sheet's percolation zone and the usefulness of swath data to diagnose the diurnal cycle of melt.

1. Introduction

Satellite-based microwave observations over the Greenland and Antarctic ice sheets have been used to determine melt occurrence, snow accumulation rates (Rotman et al., 1982; Zwally, 1977), katabatic wind intensity (Remy and Minster, 1991), and surface and depth hoar formation (Schuman et al., 1993). Such geophysical information has become increasingly important as the scientific community attempts to answer questions concerning the role of the ice sheets in various climate change scenarios. The primary concern has been the response of the mass balance of the ice sheets to potential variations in surface air temperature of the polar regions. Both surface and remotely sensed estimates of the snow accumulation and melt rates are needed to determine the impact of variations in climate on the mass balance of the ice sheets.

Recently, the melt zone of the Greenland ice sheet has been identified using radar backscatter values (Jezek et al., 1994) and radar altimeter waveforms (Ferraro, 1994). Microwave radiometric data also has been examined for indications of melt on both the Antarctic and the Greenland ice sheets on a daily, monthly and seasonal basis (Mote and Anderson, 1995; Zwally and Fiegles, 1994; Mote et al., 1993; Steffen et al., 1993). The radiometric data can be used to identify the occurrence of melt due to the increase in emissivity that results from the formation of liquid water in the snow. Liquid water in the snow also reduces the difference in brightness temperature between two channels of different frequency or polarization

from the differences associated with dry snow. However, microwave emissivity is dependent on a number of factors other than the liquid water content of the snow. Notably, the emissivity is dependent on the depth profiles of temperature, density and grain size (Zwally, 1977; Van der Veen and Jezek 1993), as well as the surface roughness (Remy and Minster, 1991) and presence of ice layers in the snowpack. As the frequency increases, a thinner layer of the snowpack is responsible for the microwave emission detected by the sensor. Therefore, daily variations in surface climate that affect the temperature, grain size, density or liquid water content of the top few centimeters of the snowpack play a large role in its microwave emissivity at high frequencies. Previous examinations of melt occurrence on the Greenland ice sheet have relied on daily averages of microwave brightness temperatures, despite the large diurnal variations that may occur in the liquid water content. This research compares swath SSM/I data to surface meteorological observations, measured snowpack temperatures, and modeled snowpack conditions for Dye 2, Greenland, from mid June to mid July 1993 to determine how variations in surface weather affect the use of satellite microwave data for melt identification.

2. The 1993 Field Season at Dye 2

The research described here was a result of one component of NASA's 1993 field season at Dye 2. Two objectives of the field program are relevant to the interpretation of melt occurrence as identified with microwave data. The first relevant objective was to collect meteorological observations during the melt season to drive an energy-balance model of the snowpack. A second objective was to collect shallow firn cores for evidence of past melt events in the snow stratigraphy and compare that record to the record of melt occurrence as interpreted from Scanning Multichannel Microwave Radiometer (SMMR) and SSM/I data. Both the model results and the core stratigraphy are being used to better understand the indications of melt identified with microwave radiometric data. The research described here is concerned with the comparison of modeled snowpack conditions to the microwave data.

Dye 2, Greenland (66°29′ N, 46°17′ W, 2117 m a.s.l.) lies in the percolation zone of the ice sheet,

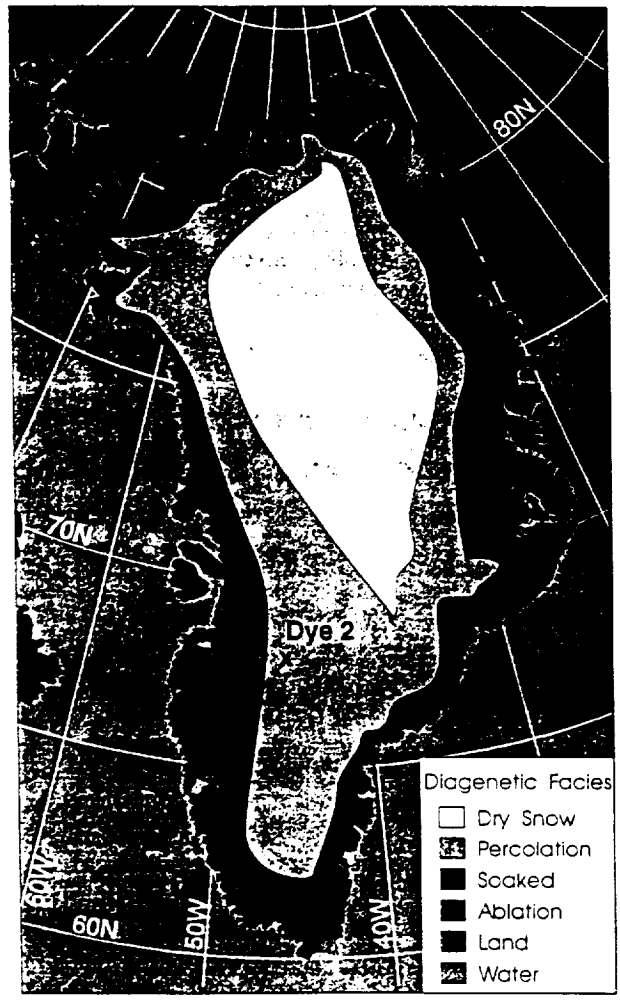

Fig. 1. Location map of Dye 2 on the Greenland ice sheet, with snow facies after Benson (1962).

a region that experiences melt but where liquid water does not completely soak the previous year's snow accumulation (Fig. 1). In the percolation zone, summer melt water percolates into the snowpack and refreezes into horizontal ice lenses and vertical ice pipes. Dye 2 is of particular interest for comparing surface conditions to microwave data because it is located in a region of the percolation zone where the microwave data indicated increasing melt frequency during the 1980s (Mote and Anderson, 1995).

Meteorological observations were taken at Dye 2 during 10 June to 13 July 1993. The measurements included hourly values of surface air temperature, snowpack temperature (at various intervals to a depth of 2 m), humidity, wind direction and speed, incoming and reflected shortwave radiation, and downwelling longwave radiation. Additional measurements of precipitation type

and amount, as well as cloud cover are available for 16 June to 13 July. These data were used to drive a one-dimensional energy and mass balance model of the snowpack that allows for melt and metamorphism of the snowpack. The model, SNTHERM.89, was developed by Rachel Jordan at the U.S. Army Cold Regions Research and Engineering Laboratory, and modified for use on the ice sheet (Jordan, 1991; Rowe et al., 1995). The model was run for the period of 21 June to 13 July and produced hourly time series that included, but were not limited to, depth profiles of temperature, liquid water content, and snow density.

3. Satellite Microwave Data

Microwave radiometric data were obtained for June and July 1993, from the SSM/I sensor aboard the Defense Meteorological Satellite Program's F-11 satellite. The satellite records radiation received at both horizontal and vertical polarizations for 19.35, 37.0, 85.5 GHz and the vertical polarization at 22.235 GHz. Because this research was an outgrowth of an examination of gridded SMMR and SSM/I data for 1979 to 1991, only channels common to both sensors were examined. The channels in common to the two sensors include both polarizations at 19.35 GHz (18 GHz for SMMR) and 37 GHz, and the vertical polarization at 22 GHz. Because the 22 GHz channel is the more sensitive to atmospheric water vapor and less sensitive to surface conditions than the other channels, it was not used in this research.

At 19.35 GHz, the footprint of the SSM/I is 69 km across track and 43 km along track, while at 37 GHz the footprint is 37 km along track and 28 km cross track (Wentz, 1991). Oversampling by the sensor allows a nominal 25 km resolution at 37 GHz. The F-11 satellite had daily overpasses of Dye 2 at approximately 0800–1000 UTC (0500 to 0700 local time) and then again around 1800–2000 UTC (1500 to 1700 local time). The passes tended to occur near the times of the lowest and highest liquid water concentrations in the snowpack so that an examination of the effect of the diurnal cycle on the snowpack's emissivity is possible.

To produce a time series of brightness temperatures for Dye 2, an inverse distance weighting approach was used for all scan cells from any one orbit that were centered within a 25 km radius of Dye 2. The number of scan cells included in the averaging for each orbit ranged from one to five with a mean of 3.6 scan cells included. The overlap in the swaths of two successive orbits often resulted in two observations during the morning or afternoon.

4. Weighted-Average Brightness Temperatures

The 37 GHz, horizontal polarization (37 H) channel was chosen for the initial comparison to modeled snowpack conditions because, for that channel, a threshold brightness temperature associated with melt has been calculated by Mote and Anderson (1995). Microwave radiometric data can be used to indicate snowpack melt due to the increase in microwave brightness temperature (at frequencies greater than 10 GHz) that occurs during melt. The emissivity of snow increases rapidly with melt due to an increase in the liquid water content of the snow. The increased emissivity is due to the high dielectric constant of liquid water, compared to that of air and ice, which strongly affects the dielectric constant of the snow-ice-air mixture. The dielectric constant is a complex number that represents a measure of the propagation characteristics of a wave through a medium (real part) and the energy losses in the medium (imaginary part). Because of the large difference in the dielectric constant of ice and water, particularly the imaginary part, a small amount of liquid water in snowpack causes a large increase in emissivity (Foster et al., 1984). In addition, the separated grains of ice that comprise a dry snowpack also cause volume scattering of the microwave radiation, an effect which is reduced by the addition of liquid water (Rango et al., 1979). The result is a strong contrast in the brightness temperature between dry snow and snow with even small amounts of liquid water. This phenomenon allows the use of a threshold brightness temperature for identifying melt occurrence. However, liquid water on the snow surface causes a decrease in emissivity due to surface reflection (Ulaby et al., 1986). No surface meltwater features were identified near Dye 2 during the summer of 1993, so the effect of surface meltwater is not a concern.

The time series of 37 H brightness temperatures was compared to SNTHERM.89 output of liquid water content averaged over the top 2 cm and the top 10 cm of the snowpack. These layers were

selected because the model results indicate that liquid water often first appears 1–3 cm below the surface of the snowpack when the air temperature is below 0 °C. This is due to radiation penetration into the snowpack and the evaporation of liquid water closer to the surface. As the model begins to indicate increased concentrations of liquid water, water becomes evident nearer to the surface and begins to percolate deeper into the snowpack. This initial formation of liquid water below the surface is also evident in liquid water content measurements at the ETH camp near the equilibrium line in West Greenland (Ohmura et al., 1991).

4.1 Snowpack Melt

The 37 H data were compared to the melt threshold value of 201.1 K for Dye 2, given by Mote and Anderson (1995). Their melt threshold values vary across the ice sheet and are partially a function of the snow accumulation rate. Regions of lower snow accumulation have lower mean annual brightness temperatures (Zwally, 1977) and lower melt threshold values. Mote and Anderson (1995) found melt threshold brightness temperatures near 230 K in the region of heavy snow accumulation on the southeast margin of the ice sheet but less than 205 K in the low accumulation region in the southwest portion of the ice sheet. Dye 2 lies in a region of relatively low accumulation and has a lower mean annual brightness temperature and melt threshold value than most locations in the melt zone of the Greenland ice sheet. The 201.1 K melt threshold value for Dye 2 seems appropriate compared to some microwave radiometric observations over a seasonal snowpack. For example, Stiles and Ulaby (1980) found 35 GHz, horizontal polarization brightness temperatures of 150–165 K for dry snow and 230–250 K for snow with 1–3 percent liquid water content. It is important to note that the 201.1 K melt threshold represents the brightness temperature for a 625 km^2 region surrounding Dye 2, in which there are almost certainly areas of both dry and wet snow during many summer days.

The afternoon observations of the 37 H brightness temperatures for each day during 9–17 June, 22–24 June and 9–12 July exceed the 201.1 K melt threshold for Dye 2. The afternoon 37 H brightness temperatures exceeded the threshold value on 1 July, by more than 35 K, and on 26 June, but only by less than 5K. The average volumetric liquid water content (m_v) in the upper 2 cm of the snowpack, as given by the SNTHERM.89 model, shows the occurrence of melt during the afternoons of 22–24 June and 10–11 July (Fig. 2). On all three days during 22–24 June, the liquid water content of the upper 2 cm of the snowpack during the time of the afternoon SSM/I overpass was greater than 6 percent; it was also greater than 6 percent on both 10 and 11 July. Although no model output are available for 9–17 June, the maximum afternoon air temperature for five of the nine days exceeded the freezing point, and the maximum afternoon temperature was within 2 K of the freezing point on the other four days. The maximum net radiation flux for those afternoons typically was greater than 150 Wm^{-2}. It is likely that melt occurred in the upper few centimeters with adequate net radiation even though surface air temperatures were slightly below the freezing point. Even if melt did not occur at Dye 2 on some of those days, it is quite likely that melt did occur at lower elevations that were within some of the scan cells included in the average. The surface air temperatures were also at or above freezing on the afternoons of 22–24 June and 10–13 July.

Melt was also indicated in the upper 2 cm of the modeled snowpack before the afternoon SSM/I overpass on 28 June as the surface air temperature rose above freezing, but the model output indicates that the surface had refrozen by the time of the sensor overpass. The 37H brightness temperature during the afternoon overpass of 28 June (188.3 K) is less than the threshold value (201.1 K), giving no indication of melt (Fig. 2). The model provides no indication of melt in the top 2 cm of the snowpack during the afternoon of 1 July, and the surface air temperature was 5 K lower than the freezing point at the time of the SSM/I overpass. However, the 37H brightness temperatures during the afternoon overpasses were 236.2 K at 18 UTC (1500 local time) and 213 K at 20 UTC (1700 local time), which are both above the melt threshold value (Fig. 2). Although no melt was indicated in the top 2 cm, there was an indication of melt in the top 10 cm. Despite the low surface air temperatures, enough net radiation (150–200 Wm^{-2}) was available to cause the model to simulate melting. The low density of the fresh snow that fell during the morning of 1 July likely allowed pene-

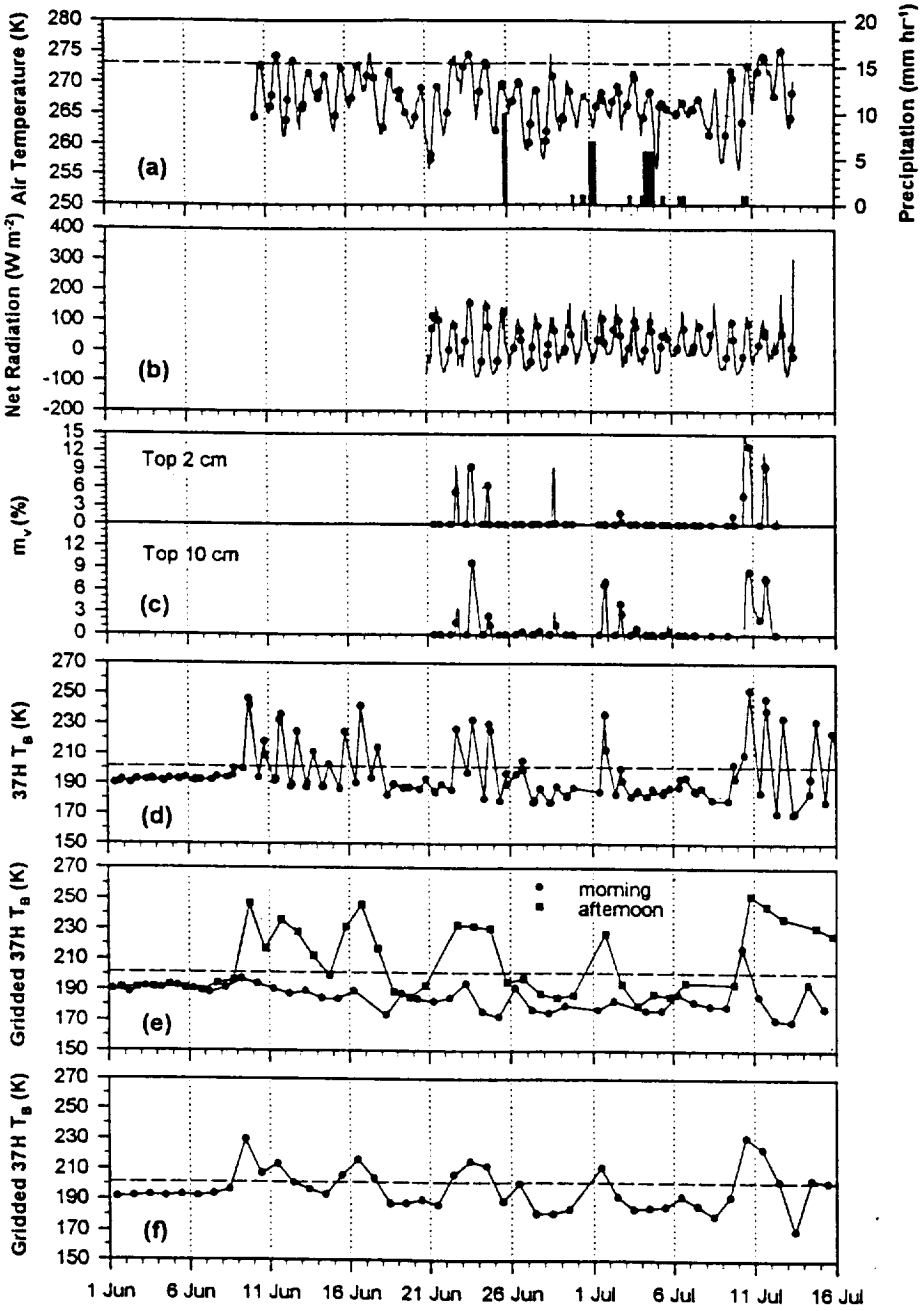

Fig. 2. Meteorological data, modeled snowpack conditions and concurrent SSM/I brightness temperature time series for June and July 1993 at Dye 2, Greenland. Surface air temperatures (solid line), surface air temperatures taken at the time of SSM/I overpasses (circles), and precipitation (bars) (a); modeled net radiation (solid line), and modeled net radiation at the time of an SSM/I overpass (circles) (b); modeled liquid water content averaged in the top 2 and top 10 cm of the snowpack (solid line), and modeled liquid water content at the time of an SSM/I overpass (circles) (c); weighted average 37H brightness temperatures (d); morning (circles) and afternoon (squares) gridded 37H brightness temperatures (e); daily averaged, gridded 37H brightness temperatures (f)

tration of radiation further into the snowpack, producing melt below but not within the top 2 cm of the snowpack. It is also likely that the fine-grained fresh snowfall reduced the scattering of microwave radiation and contributed to the increased brightness temperatures on the afternoon of 1 July.

In one case, the model output indicated liquid water in the snowpack, but the 37H brightness temperatures were not elevated. The 11 July m_v for the top 10 cm of the snow showed approximately 3 percent liquid water content, although the model output showed the top 2 cm as dry. Although the model indicates some liquid water in the top 10 cm, the 37 H brightness temperature for the 11 July morning overpass was only 184.3 K. This is in contrast to the observations and model output during the afternoon of 1 July, in which the model output shows liquid water in the snowpack below a dry layer, but the microwave data show a relatively high brightness temperature (236.2 K at 18 UTC). This difference at

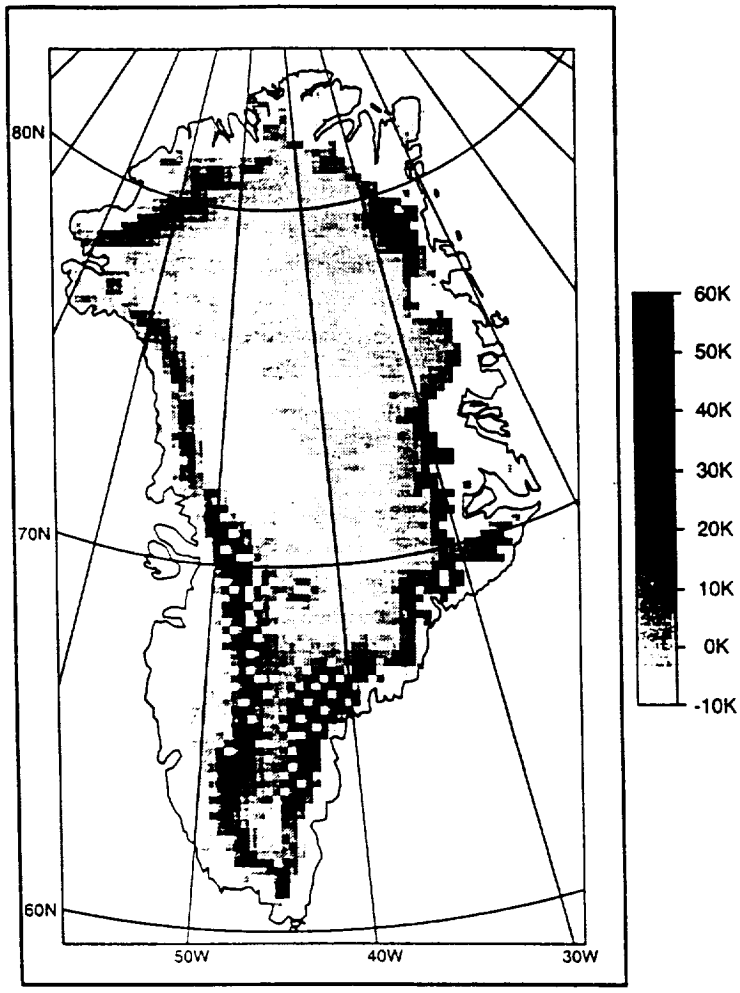

Fig. 3. Afternoon 37H brightness temperatures minus morning 37H brightness temperatures for 23 June 1993 across the Greenland ice sheet

first suggests that the model may not be adequately handling the percolation and refreezing of melt water in the snowpack, and the top 10 cm of the snowpack was actually dry on 11 July. However, the difference between the afternoon of 1 July and the morning of 11 July was that on 11 July the top 2 cm was a refrozen snow layer while on 1 July the surface of the snowpack was freshly fallen snow. The large-grained, refrozen upper layers on the morning of 11 July would have scattered the radiation emitted from the underlying wet layers, reducing the brightness temperature, while the fine-grained fresh snow on 1 July did not.

Because all days in which melt occurred showed evidence of refreezing during the morning, the afternoon-morning brightness temperature difference was examined for all available SSM/I data over the Greenland ice sheet. The daily maps of the gridded brightness temperatures for the afternoon minus the morning observations were examined for the period of 1 June to 19 July 1993. As an example, a map of the afternoon minus the morning brightness temperatures for 23 June, a day with afternoon melt at Dye 2, shows differences as great as 60K in some locations in the south and southwest margins of the ice sheet (Fig. 3). A region of brightness temperature differences greater than 30 K follows the margin of the south dome of the ice sheet from approximately 65° N on the eastern margin to approximately 68° N on the western margin of the south dome. This area of large brightness temperature differences extends from the margin of the ice sheet to approximately 1800 m a.s.l. The large diurnal variation in brightness temperature associated with afternoon melt and morning refreeze that was identified at Dye 2 is also evident across most of the ice sheet that is known to experience melt.

4.2 Precipitation and Metamorphism

Only the afternoon of 26 June had a brightness temperature above the threshold value but was

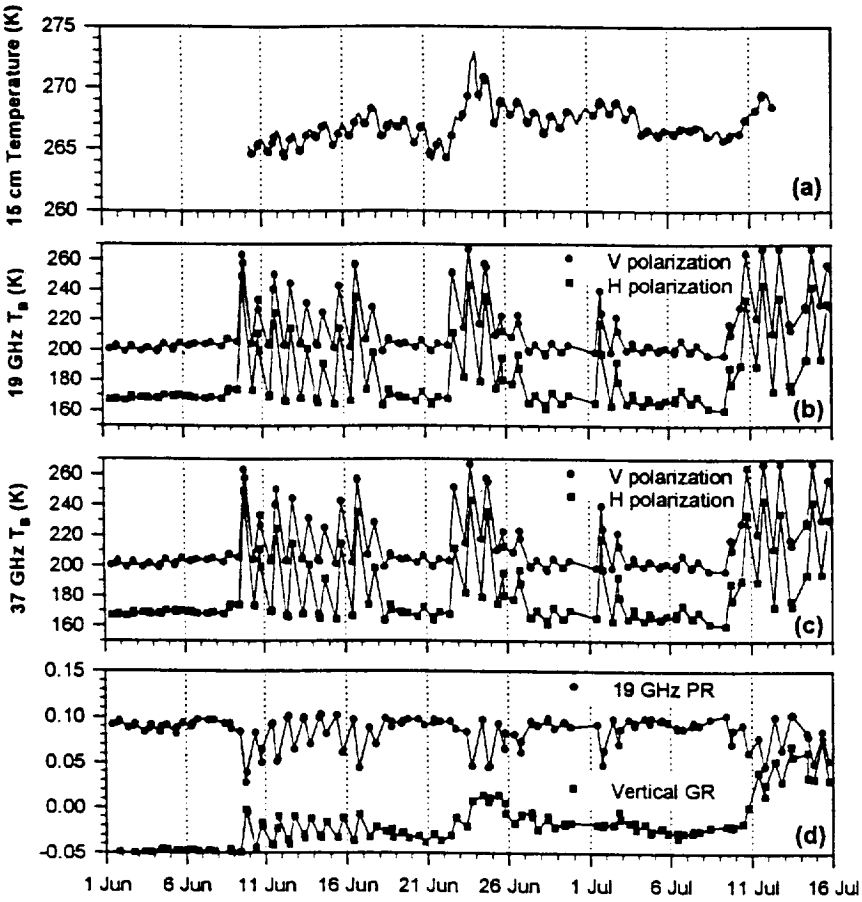

Fig. 4. Measured snowpack temperatures and normalized differences of the SSM/I brightness temperatures during June and July 1993 for Dye 2, Greenland. Measured snowpack temperatures at a depth of 15 cm (solid line), and measured snowpack temperatures at times of SSM/I overpasses (circles) (a); 19 GHz vertical (circles) and horizontal (squares) brightness temperatures (b); 37 GHz vertical (circles) and horizontal (squares) brightness temperatures (c); 19 GHz polarization ratio (circles) and vertical gradient ratios (squares) (d)

not associated with some clear indication of melt in the model output. The morning of 26 June also had a brightness temperature approximately 10 K greater than morning brightness temperatures for days immediately before and after that day. An initial hypothesis was that the increase in brightness temperature was due to warming of the snowpack. The snowpack temperature measured at 15 cm was 272 K at 3 UTC on 24 June (Fig. 4) and the temperature measured at 20 cm was 270 K at 18 UTC on 24 June. In both cases, the temperature were higher than at any other time from 11 June to 13 July at the respective depths in the snowpack. The warming of the snow apparently was due to heat transported into the snowpack by the meltwater formed on 22–24 July and the latent heat released during the refreezing of the meltwater. However, the 15 cm snowpack temperatures were between 266 and 268 K during both 26 and 27 June, while the 37H brightness temperature decreased from 205.4 K on the afternoon of 26 June to 177.5 K on the morning of 27 June. Because of the linear relationship between physical temperature and brightness temperature, the variations in physical temperature cannot explain the higher than expected 37H brightness temperatures on 26 June.

Another possible explanation of the higher than expected brightness temperatures was the location of the scan cells included in the weighted average. On the afternoon of 26 June, the scan cell with the highest 37H brightness temperature (216.0 K), was centered 24.1 km to the west-northwest of Dye 2. By plotting the location of the scan cell on a topographic map of Greenland, one can see that the footprint of the scan cell included a region as much as 200 m lower than Dye 2. It is possible that the snowpack at lower elevations within that scan cell was experiencing some melt, raising the brightness temperature recorded for that scan cell.

Although the location of the individual scan cells may explain the higher than expected afternoon 37H brightness temperature on 26 June, the

morning brightness temperature that day was also approximately 10 K higher than other mornings in late June. This is likely due to the 5 cm of fresh snow that fell on the evening of 25 June (Fig. 2). The fine-grained snow that fell may have reduced the microwave scattering, resulting in the increased brightness temperature. This may also explain why the brightness temperatures on 5 July are approximately 5 K higher than on other days without melt in early July. Dye 2 had approximately 12 cm of fresh snow during 3–6 July, mostly on 4 July. The snowfall that occurred on 30 June and 1 July does not show the same effect in the morning 37 H brightness temperatures, but melt occurred immediately after the snowfall ended. The melt likely resulted in immediate metamorphism of the fresh snow, which increased the snow grain size and eliminated any increase in emissivity due to the fresh snow.

Melt-freeze metamorphism results in increased grain size, which increases the effect of volume scattering and reduces the brightness temperatures. At Dye 2, a result of this process is the downward trend in morning brightness temperatures from approximately 190 K during early June to 170 K in mid July. These changes appear in steps that correspond to the various melt periods. The morning brightness temperatures decreased from slightly greater than 190 K during the first week of June to approximately 185 K after the 9–17 June melt period. After the 22–24 June melt period, the morning brightness temperatures decreased to approximately 180 K, and then decreased to about 170 K during the melt period that began 9 July.

4.3 Normalized Differences of Brightness Temperatures

While our research has used a single-channel threshold method to identify melt events. Steffen et al. (1993) used multi-channel, normalized difference measure of the 19 and 37 GHz brightness temperatures for melt identification. Individually, the time series for each of the four SSM/I channels had similar characteristics during June and July 1993 at Dye 2. To determine how the evolution of the snowpack affected the other SSM/I channels, normalized differences of brightness temperatures for channels of different frequencies or polarizations were calculated.

The polarization ratio (PR) at a frequency f is defined as:

$$PR_f = (T_{B,v} - T_{B,h})/(T_{B,v} + T_{B,h}) \quad (1)$$

where $T_{B,v}$ is the vertical polarization brightness temperature at that frequency and $T_{B,h}$ is the horizontal polarization brightness temperature.

The gradient ratio (GR) at a polarization p is defined as:

$$GR_p = (T_{B,37} - T_{B,19})/(T_{B,37} + T_{B,19}) \quad (2)$$

where $T_{B,19}$ is the 19 GHz brightness temperature for that polarization and $T_{B,37}$ is the 37 GHz brightness temperature. In particular, the GR was examined for the effect of meltwater penetration on the emissivity at different frequencies. Due to the longer wavelength of radiation, the 19 GHz channels are sensitive to radiation emitted from a greater depth into the snowpack than are the 37 GHz channels. Thus, the GR tends toward zero or become positive during melt episodes.

The 19V, 19H and 37V channels show the same indications of melt as the 37H channel. Additionally, both of the normalized differences of the channels, the PR and GR, show evidence of the effects of snowpack melting. During the daily melt-refreeze cycles of 9–17 June, the PR and GR both tended toward zero during afternoon melting (Fig. 4). Throughout the study period, the PR values tended toward zero during the same afternoons that had increased brightness temperatures for the 37H channel.

During the melt period of 22–24 June, both the morning and afternoon GR values tended toward zero. Although GR values near zero are sometimes associated with the occurrence of melt (Steffen et al., 1993), there was no evidence from the meteorological data, model output or the use of a single-channel threshold to support the conclusion that melt occurred during the morning SSM/I overpass. The GR values on the mornings of 22–24 June may have been due to the warming of the underlying snowpack that is evident in the temperature profile of the snowpack during this period. The colder, refrozen snow near the surface resulted in a lower brightness temperature at 37 GHz than at 19 GHz, which is apparent in the GR for 24 and 25 June.

A step-change in the GR values from predominately negative to predominately positive values occurred on 10–11 July. This coincides with a

period when the model showed significant melt and liquid water percolation to 15–20 cm. The meltwater percolation occurred during the afternoon of 10 July and the subsequent warming of the snowpack with meltwater refreezing occurred late on 10 July and into the morning of 11 July (Fig. 4). The increased physical temperature of the snowpack at 15–20 cm as well as the increase in emissivity due to the introduction of liquid water at that depth may be the reason for increased brightness temperatures at 19 GHz and a positive GR. In general, both the PR and GR time series can be used to identify the melt periods that are also evident in the time series of the 37H brightness temperatures.

5. Gridded Brightness Temperatures

The field work conducted at Dye 2 was an outgrowth of research that has used gridded SMMR and SSM/I brightness temperatures available from the National Snow and Ice Data Center (NSIDC) for identifying melt occurrence on the Greenland ice sheet. In the NSIDC data set, all scan cells that were centered within a given grid cell were averaged for each day (beginning at 0 UTC). This approach results in the loss of diurnal variations in brightness temperatures. One objective of the present work was to compare both the swath data and gridded data for Dye 2 to the surface meteorological data and snowpack conditions to determine what information is lost in the daily averaging procedure.

The swath brightness temperatures were binned into the polar stereographic grid defined by NSIDC using three different averaging periods. First, observations were averaged into either morning or afternoon grids; then, all observations were averaged on a daily basis. In all three cases, no weighting was applied to produce the averages. If the center of a scan cell was within the square 25×25 km grid cell that contains Dye 2, it was included in the average. Thus, the spatial resolution of the three binned time series is comparable to that of the weighted average time series.

Both the twice-daily and daily time series seem to preserve the dominant features of the time series from the weighted average of the orbital data. The daily gridded and the afternoon gridded data indicated that surface melt was occurring on 9–11, 15–17 and 22–24 June, 1 July and 10–12 July (Fig. 2). However, the time series from the daily averaged data did not exceed the threshold value associated with melt on 12–14 June, while the time series from the gridded data of afternoon overpasses did not indicate melt on 14 June. The brightness temperatures in the weighted average time series did indicate melt each afternoon during 9–17 June, although the 37H brightness temperature exceeded the melt threshold by less than 2K on the afternoon of 14 June. Because no model output is available before 16 June, it is uncertain whether any melt actually occurred on the afternoon of 14 June. The surface temperatures and net radiation flux for that afternoon indicate that conditions were conducive to modest, radiation-induced melting. Additionally, only a small increase in the threshold value associated with melt could result in the conclusion that no melt occurred that afternoon with any of the three time series presented here.

One problem with the daily gridded data is the occurrence of two overpasses in either the morning or in the afternoon that are subsequently included in the averaging. The result is a possible bias toward the morning or afternoon values in the daily average. For example, two overpasses of the sensor occurred on the afternoon of 11 July, while only one morning overpass occurred. Additionally, the morning overpass only had three scan cells included in the average, while the two afternoon overpasses had five scan cells on the 18 UTC overpass and four cells on the 19 UTC overpass included in the average. As a result, the daily average is heavily weighted toward the afternoon conditions. The weighted average of scan cells for the 37H channel during the 9 UTC overpass showed a brightness temperature of 184.3K, while the afternoon overpasses at 18 and 19 UTC showed 37H brightness temperatures of 246.7 K and 238.9 K, respectively. The daily average for the gridded data showed a brightness temperature of 224 K for the grid cell that includes Dye 2. However, averaging the scan cells from the two afternoon overpasses and then averaging that result with the average of the scan cells from the morning overpass yields a daily average of only 214 K.

The process of binning data into a grid, compared to the inverse-distance weighted average was also examined. This was done by comparing the morning and afternoon gridded data to the

orbital data for dates on which there was only one morning or afternoon overpass of the sensor. The brightness temperatures produced by the binning or weighted average processes were nearly identical and would not affect the identification of melt. One exception was the afternoon of 14 June, when the afternoon gridded brightness was approximately 1 K less than the melt threshold and the inverse-distance weighted average produced a brightness temperature about 1 K above the melt threshold.

6. Conclusions

Meteorological observations recorded at Dye 2, Greenland, during June and July 1993 were used to drive an energy-balance model of the snowpack. The liquid water content values output from the model and the various meteorological observations were compared to time series of Special Sensor Microwave/Imager (SSM/I) data averaged for scan cells centered within 25 km of Dye 2.

Diurnal melt-freeze cycles that occurred during mid June to early July are evident both by an increase and subsequent decrease in the microwave brightness temperatures and from the formation of liquid water as shown in the model output. Additionally, the effects of the melt-freeze metamorphosis of the snow and new snow accumulation are evident in the brightness temperature time series. These time series demonstrate that a brightness temperature threshold for a single channel of microwave data can be used for melt identification, particularly if other geophysical characteristics of the snowpack are also considered. One improvement on the single-channel threshold approach might be the addition of an afternoon-morning difference for a given channel. A threshold of the afternoon- morning brightness temperature difference could be used in conjunction with a single-channel threshold to account for melt occurring throughout the low-sun hours, which would not be detected by using an afternoon-morning difference alone.

Due to the relatively coarse resolution of passive microwave data, heterogeneous snow conditions within a grid cell or scan cell introduce difficulty in interpreting the microwave data. This is particularly true when comparing surface conditions at one point to scan cells that may include information from sites nearly 50 km away from the location of interest. The use of modeled surface conditions for comparison to the microwave data partially alleviates this problem because the modeled snowpack conditions are probably more representative of mixed conditions than a firn core or snow pit.

The different approaches to spatial and temporal averaging of the microwave data also introduce uncertainties into interpreting the resultant time series. To illustrate these problems, the time series produced from an inverse-distance weighted average of scan cells within 25 km of Dye 2 was compared to data binned into a 25 × 25 km grid cell that includes Dye 2, averaged on either a daily or twice-daily basis. The gridding process used can make a substantial difference in the estimated brightness temperature for a given location, particularly if the scan cells included in a daily average tend to be clustered more in the morning or afternoon.

Acknowledgments

This work was supported by the Polar Oceans and Ice Sheets Program of the National Aeronautics and Space Administration, grant NAGW-1266, and by the NASA Global Change Fellowship Program, training grant NGT-30127, both to the University of Nebraska-Lincoln. The authors thank M. R. Anderson, E. J. Ferraro, K. C. Jezek, K. C. Kuivinen, and I. H. H. Zabel for assistance in collecting observations at Dye 2.

References

Benson, C. S., 1962: Stratigraphic studies in the snow and firn of the Greenland ice sheet. CRREL Res. Rep. 70. CRREL, Hanover, NH, 93 pp.

Ferraro, E. J., 1994: Analysis of Airborne Radar Altimetry Measurements of the Greenland Ice Sheet. Ph.D. Dissertation, University of Massachusetts, Amherst, MA, 164 pp.

Foster, J. L., Hall, D. K., Chang, A. T. C., Rango, A., 1984: An overview of passive microwave snow research and results. *Rev. Geophys. Space Res.*, **22**, 195–208.

Jezek, K. C., Gogineni, P., Shanableh, M., 1994: Radar measurements of melt zones on the Greenland ice sheet. *Geophys. Res. Letters*, **21**, 33–36.

Jordan, R., 1991: A one-dimensional model for a snow cover: technical documentation for SNTHERM.89 Special Report 91-16. U.S. Army Crops of Engineers, Cold Regions Research and Engineering Laboratory, Hanover, NH.

Mote, T. L., Anderson, M. R., Kuivinen, K. C., Rowe, C. M., 1993: Passive microwave-derived spatial and temporal variations of summer melt on the Greenland ice sheet. *Ann. Glaciol.*, **17**, 233–238.

Mote, T. L., Anderson, M. R., 1995: Variations in snowpack melt on the Greenland ice sheet based on passive microwave measurements. *J. Glaciol.*, **17**, 51–60.

Ohmura, A., Steffen, K., Blatter, H., Greuell, W., Rotach, M., Konzelmann, T., Laternser, M., Ouchi, A., Steiger, D., 1991: Energy and Mass Balance During the Melt Season at the Equilibrium Line Altitude, Paakitsoq, Greenland Ice Sheet: Progress Report No. 1. Department of Geography, Swiss Federal Institute of Technology, Zurich, 118 pp.

Rango, A., Chang, A. T. C., Foster, J. L., 1979: The utilization of spaceborne microwave radiometers for monitoring snowpack properties. *Nord. Hydrol.*, **10**, 25–40.

Remy, F., Minster, J. F., 1991: A comparison between active and passive microwave measurements of the Antarctic ice sheet and their association with the surface katabatic winds. *J. Glaciol.*, **37**, 3–10.

Rotman, S. R., Fisher, A. D., Staelin, D. H., 1982: Inversion for physical characteristics of snow using passive radiometric observations. *J. Glaciol.*, **28**, 179–185.

Rowe, C. M., Kuivinen, K. C., Jordan, R., 1995: Simulation of summer snowmelt on the Greenland ice sheet using a one-dimensional model. *J. Geophys. Res.*, **100**, 16,265–16,273.

Schuman, C. A., Alley, R. B., Anandakrishnan, S., 1993: Characterization of a hoar-development episode using SSM/I brightness temperatures in the vicinity of the GISP-2 site, Greenland. *Ann. Glaciol.*, **17**, 183–188.

Steffen, K., Abdalati, W., Stroeve, J., 1993: Climate sensitivity studies of the Greenland ice sheet using satellite AVHRR, SMMR, SSM/I and in situ data. *Meteorol. Atmos. Phys.*, **51**, 239–258.

Stiles, W. H., Ulaby, F. T., 1980: The active and passive microwave response to snow parameters: 1. Wetness. *J. Geophys. Res.*, **85**, 1037–1044.

Ulaby, F. T., Moore, R. K., Fung, A. K., 1986: *Microwave Remote Sensing, Active and Passive*, vol. 3. Reading, MA: Addison-Wesley, 2162 pp.

van der Veen, C. J., Jezek, K., 1993: Seasonal variations in brightness temperature for central Antarctica. *Ann. Glaciol.*, **17**, 300–306.

Wentz, F. J., 1991: SSM/I Antenna Temperature Tapes User's Manual, Revision 1. Remote Sensing Systems, Santa Rosa, CA, 70 pp.

Zwally, H. J., 1977: Microwave emissivity and accumulation rate of polar firn. *J. Glaciol.*, **18**, 195–215.

Zwally, H. J., Fiegles, S., 1994: Extent and duration of Antarctic surface melt. *J. Glaciol.*, **40**, 463–476.

Authors' addresses: Thomas L. Mote, Department of Geography, University of Georgia, 204 GGS Building, Athens, GA 30602-2502, U.S.A.; C. M. Rowe, Program in Meteorology/Climatology, Department of Geography, University of Nebraska-Lincoln, Nebraska, U.S.A.

CRREL SPECIAL REPORT
96-27

A Comparison of Passive Microwave Techniques for Detecting Snowpack Melt on the Greenland Ice Sheet

MARK R. ANDERSON
University of Nebraska–Lincoln

THOMAS MOTE
University of Georgia

WALEED ABDALATI
CIRES, University of Colorado

INTRODUCTION

Snowpack melt occurrences detected using passive microwave data have been used to examine climate variability on the Greenland ice sheet. This study compares two techniques to detect snowpack melt using passive microwave data. The first approach (Mote and Anderson 1995) uses thresholds of 37-Ghz, horizontally polarized brightness temperatures to determine when melt is occurring. The thresholds vary by grid cell and are a function of the spring brightness temperatures. Observed brightness temperatures are compared to modeled brightness temperatures associated with the onset of melt. The second method (Abdalati and Steffen 1995) uses a cross-polarized gradient ratio (XPGR), which is the normalized difference of the 19-Ghz, horizontally polarized, and the 37-Ghz, vertically polarized brightness temperatures. Abdalati and Steffen (1995) determined a threshold for the XPGR from field observations. Thresholds chosen for both methods corresponded to a 1% liquid water content in the snowpack.

The comparison was conducted for the entire Greenland ice sheet using orbital SSM/I brightness temperatures from 1990. To maintain consistency, the orbital data were gridded into morning and afternoon passes and then into a daily composite. The same mask was used to exclude land and water areas near the ice sheet margin. Orbital SSM/I brightness temperatures from 1993 were compared with surface observations and energy-balance model results from Dye 2.

RESULTS

The results of this study indicate strong correlations between the daily spatial extent of surface melt (melt area) identified by the two methodologies using the gridded brightness temperatures. The melt occurrences identified by the two approaches were generally similar in both extent and duration (Fig. 1 and 2). However, some differences between the techniques were observed (Fig. 3). The XPGR approach (Abdalati and Steffen 1995) produces a slightly higher overall melt area than the single-channel technique (Mote and Anderson 1995) when the melt areas are accumulated over the entire season, 1.34 and 1.17×10^8 km^2, respectively. Time series of daily melt area for both approaches (Fig. 4) and the differences between the approaches (Fig. 5) were also generated. The single-channel approach indicates more daily fluctuations than the XPGR approach. This difference is most likely attributable to the stronger dependence of the 37-GHz channel used in the single-channel approach on liquid water in the top few centimeters of the snowpack. During the end of the season, the XPGR approach indicates more melt.

A difference in the timing of the snowpack melt between the two approaches is also apparent. The two time series of daily melt area were cross-correlated with lags of 1 to 10 days. The highest cross-correlation between the time series was with the single-channel approach, leading the XPGR approach by 7 days (Fig. 6). The cross-correlation coefficients are:

1. No adjustments to either time series, $r = 0.64$;
2. The single-channel approach lagged seven days, $r = 0.75$;
3. The single-channel approach lagged 7 days and smoothed with a 10-day centered moving average, $r = 0.84$.

Although a lag is clearly present between the time series, it appears that the lag develops during the melt season. During May and June there is very little lag between the time series, but a lag becomes very apparent in July and August. The

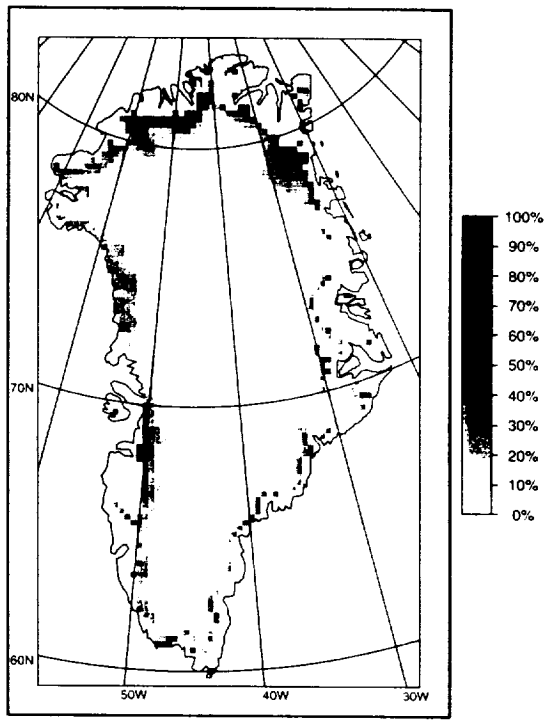

Figure 1. Frequency of melt (in days) identified by the single-channel approach.

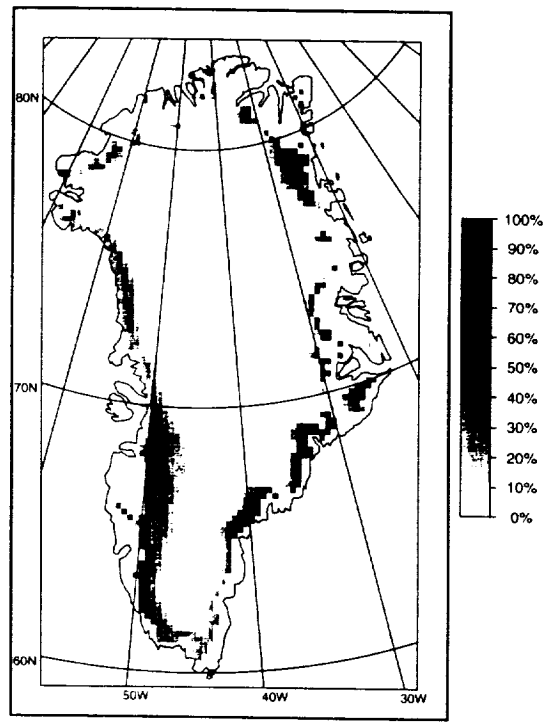

Figure 2. Frequency of melt (in days) identified by the XPGR approach.

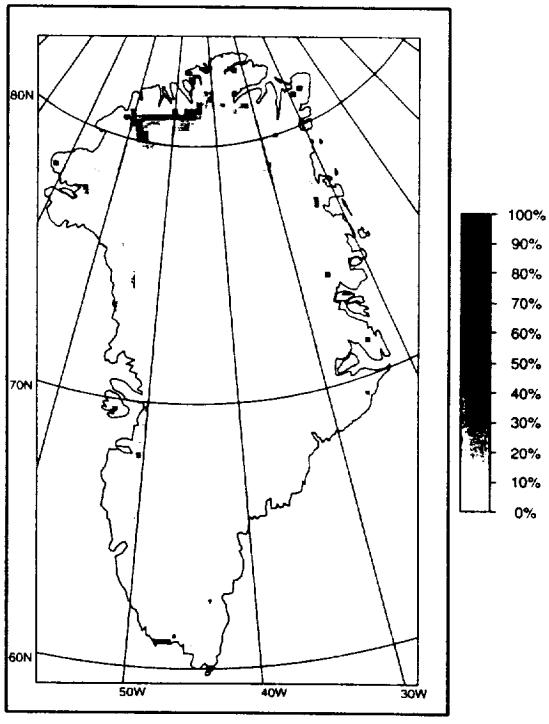

a. When the single-channel shows a higher melt frequency (a positive difference).

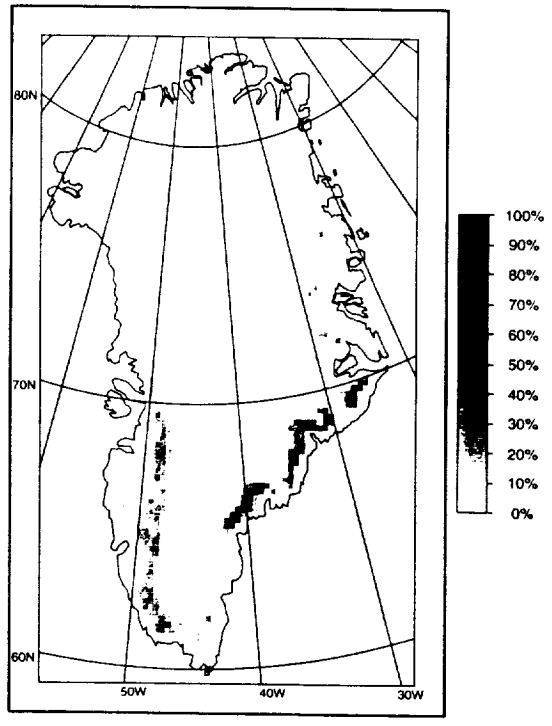

b. When the XPGR displays a higher melt frequency (a negative difference).

Figure 3. The difference in frequency of melt (in days) identified by the single-channel minus the XPGR approach.

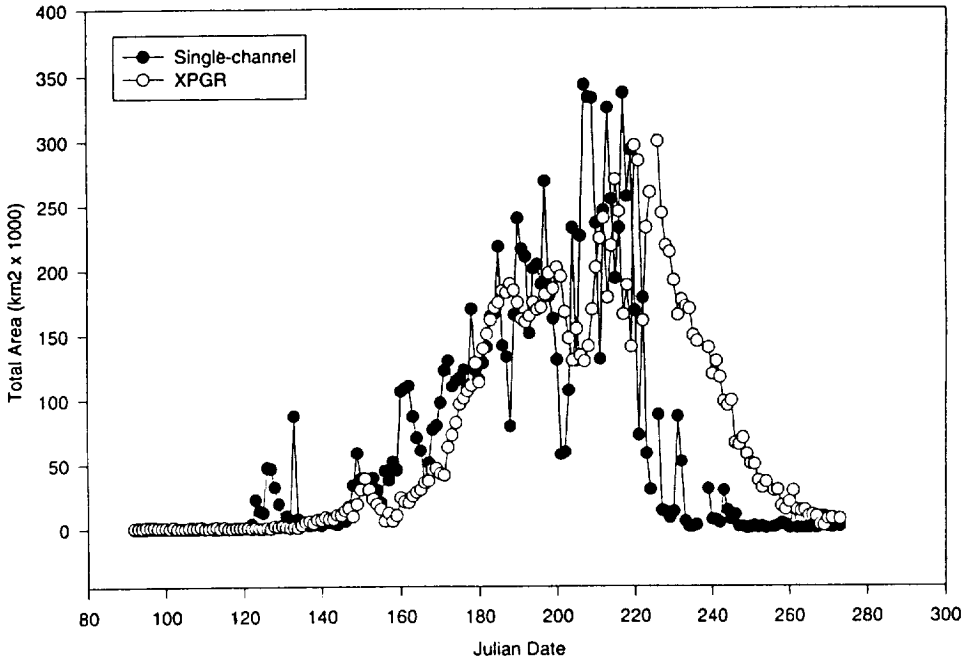

Figure 4. Time series of daily melt for the single-channel and XPGR approaches.

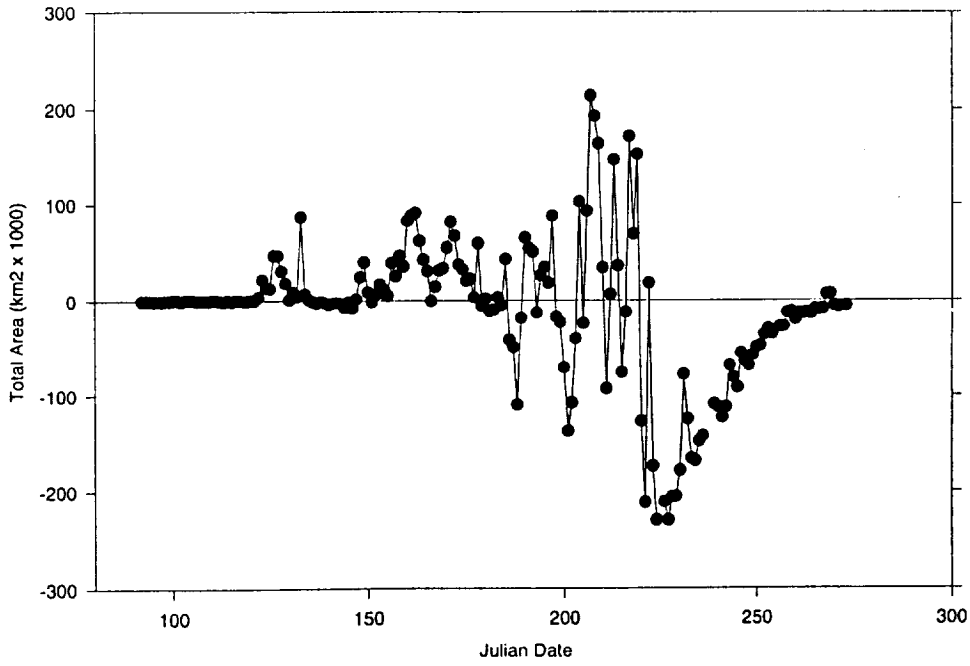

Figure 5. Differences in the time series of daily melt for the single-channel minus XPGR approaches.

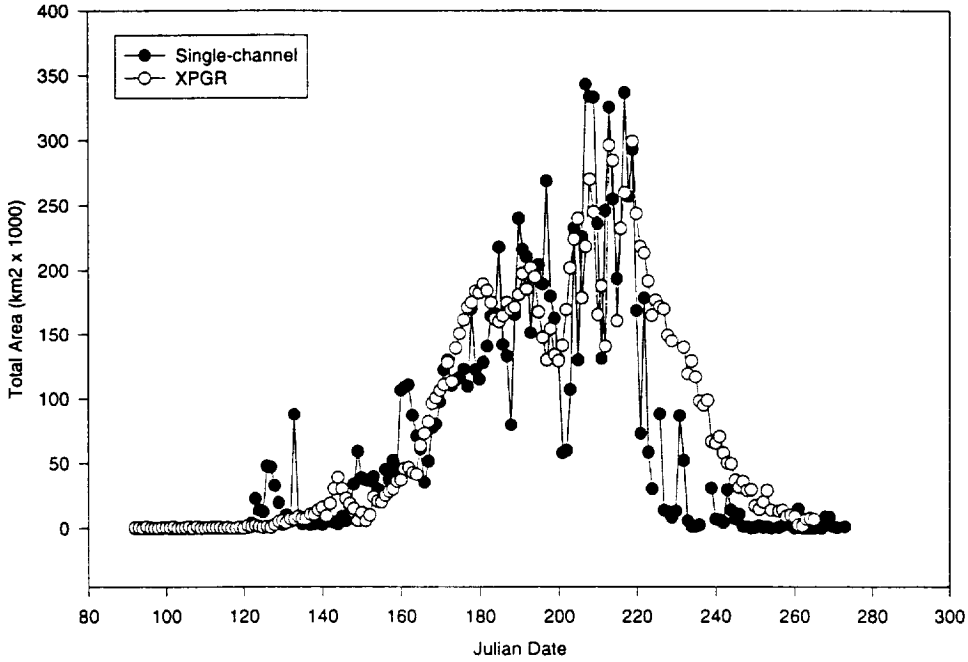

Figure 6. Time series of daily melt for the single-channel and XPGR lagged 7 days.

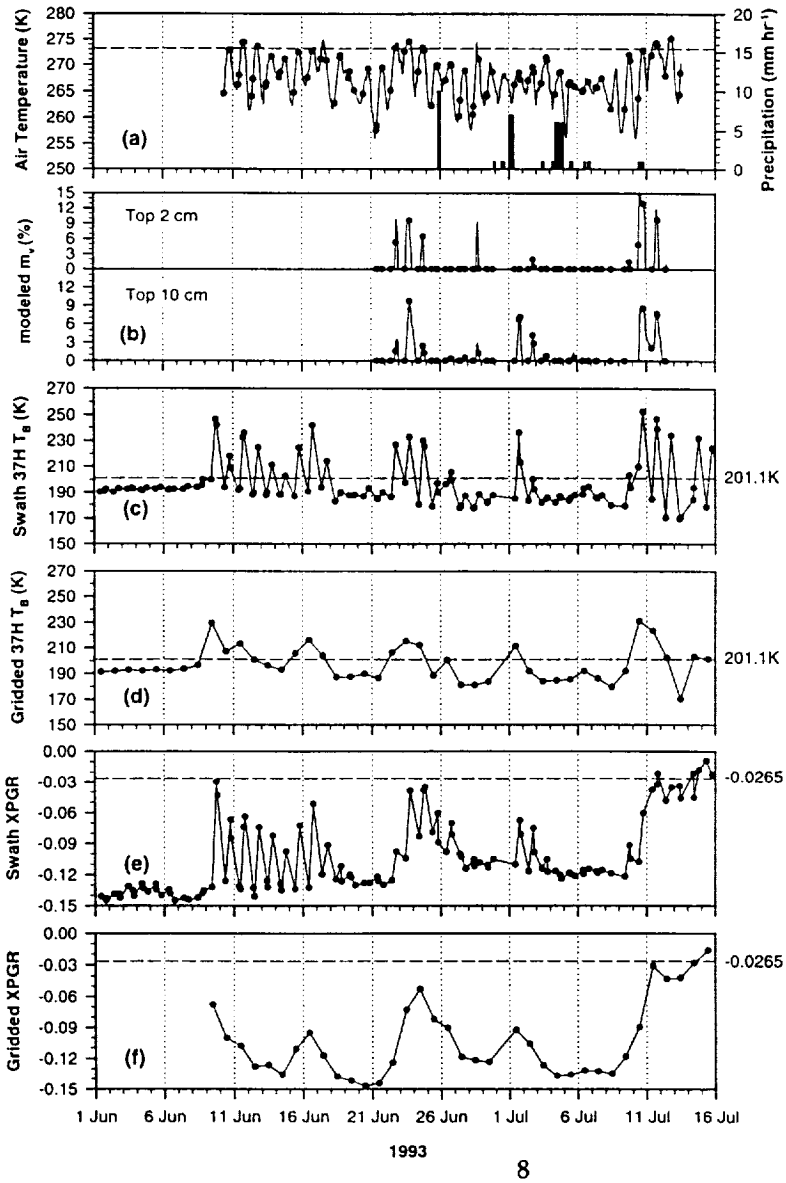

Figure 7. Time series for Dye 2, Greenland, representing surface observations, energy-balance model results, and swath brightness temperature data.

lag may even be greater than 7 days late in the melt season. This change in the lag during the melt season possibly is caused by the lack of penetration of liquid water into the snowpack early in the season. Later in the melt season, the XPGR approach may be indicating meltwater a few centimeters into the snowack as a residual from a previous day's melting. The single-channel approach's thresholds need to be adjusted lower late in the melt season to account for lower non-melt brightness temperatures that result from larger snow grain sizes after metamorphism. If this is the case, the single-channel approach is underestimating melt late in the season. The XPGR approach may also be overestimating melt late in the summer by identifying highly metamorphosed snow as melt.

Similar results were found when a more detailed study of the swath brightness temperatures for Dye 2 were analyzed for 1993 (Fig. 7). The swath data were also gridded for comparison. The single-channel approach indicates melt during periods with temperatures above 0°C and when the modeled liquid water content is above 1%. The XPGR approach only reaches its melt threshold after prolonged melt has occurred, near the end of the period. The single-channel approach identifies more melt events and identifies them earlier in the melt season. Both approaches show reduced response to melt owing to the temporal averaging of the swath data.

CONCLUSIONS

Monitoring surface snowmelt and melt frequency from passive microwave data needs to be continued to establish a longer period of record for use in climate change studies and to aid in understanding the energy balance responses of the Greenland ice sheet. The research presented demonstrates that the two approaches detect similar extents and durations of melt occurrences. The results also indicate that both approaches do have differences in detection of snowmelt, most likely attributable to how melt occurs in the snowpack and its representation by passive microwave radiation. The potential exists for combining the techniques to get some indication of the vertical extent of melt. Even though passive microwave sensors and their calibrations have changed in the past and will continue to change in the future, the approaches used to determine melt are important, allowing long time series of daily melt extent to be established. From these time series, annual variations in the extent of melt can be determined, advancing our knowledge of how the Greenland ice sheet might respond to future climate changes.

ACKNOWLEDGMENTS

This work was supported at the University of Nebraska by NASA grant NAGW-1266 and training grant NAGW-3685, and at the University of Colorado by NASA grant NAGW-2158 and from the Swiss National Foundation for Scientific Research grants 21-27449.89 and 20-36396.92. The SSM/I gridded brightness temperatures obtained on CD-ROM were from the National Snow and Ice Data Center, Boulder, Colorado.

LITERATURE CITED

Abdalati, W. and K. Steffen (1995) Passive microwave-derived snow melt regions on the Greenland ice sheet. *Geophy. Res. Let.*, **22**(7): 787–790.

Mote, T.L. and M.R. Anderson (1995) Variations in snowpack melt on the Greenland ice sheet based on passive microwave measurements. *Journal of Glaciology*, **41**(137): 51–60.

10.6

SNOWPACK METAMORPHISM AT DYE 2, GREENLAND, INFERRED FROM SSM/I AND SURFACE METEOROLOGICAL OBSERVATIONS

Thomas L. Mote*

University of Georgia
Athens, Georgia

Clinton M. Rowe

University of Nebraska-Lincoln
Lincoln, Nebraska

1. INTRODUCTION

Meteorological observations and output from a one-dimensional energy and mass balance model of the snowpack were compared to microwave radiometric data during the summer of 1993 for Dye 2, Greenland. Dye 2 (66°29'N, 46°17'W, 2260m a.s.l.) lies in the percolation zone of the Greenland ice sheet, a zone where melt occurs but where any meltwater percolates into the snowpack and refreezes. The comparison was made as part of a larger project using microwave radiometric data to map the melt zone of the Greenland ice sheet. The field season at Dye 2 was designed to examine (1) the accuracy of microwave data in identifying surface melt, (2) the meteorological conditions associated with melt in this region, and (3) the effect of snowpack metamorphism on the snowpack's microwave emissivity.

2. DATA

Meteorological observations were taken during 10 June to 13 July 1993 at Dye 2. The measurements included hourly values of surface air temperature, snowpack temperatures (to a depth of 2m), humidity, wind direction and speed, incoming and reflected shortwave radiation, and downwelling longwave radiation. These data were used to drive a one-dimensional energy and mass balance model that allows for melt and metamorphism of the snowpack. The model, SNTHERM.89, was developed at the U.S. Army Cold Regions Research and Engineering Laboratory (Jordan, 1991), and modified for use on the ice sheet (Rowe *et al.*, 1995). The model produced hourly time series that included, but were not limited to, depth profiles of temperature, liquid water content, and snow density for the period of 21 June to 13 July 1993.

Microwave radiometric data from the Special Sensor Microwave/Imager (SSM/I) sensor aboard the DMSP F-11 satellite were obtained for June and July 1993 (Wentz, 1991). An inverse distance weighting approach was used for all scan cells that were centered within a 25 km radius of Dye 2 to produce a time series of brightness temperatures for Dye 2. Morning overpasses occurred at 0900-1100 UTC (0600-0800 LST), and afternoon overpasses occurred at 1400-1700 UTC (1100-1400 LST).

3. RESULTS

The 37 GHz, horizontal polarization, (37H) brightness temperatures were compared to SNTHERM.89 output of volumetric water content and energy fluxes (Figure 1). The volumetric water content was averaged over 2 and 10 cm layers, which were selected because the model output indicates that liquid water often first appears 1-3 cm below the surface of the snowpack when the air temperature is below 0°C. This is due to radiation penetration into the snowpack and the evaporation of liquid water closer to the surface. As the model begins to indicate increased concentrations of liquid water, water becomes evident nearer to the surface and begins to percolate deeper into the snowpack.

3.1 *Snowpack Melt*

The afternoon observations of the 37H brightness temperatures for each day during 22-24 June and 9-12 July exceeded a threshold value of 201.1K calculated by Mote and Anderson (1995) that is associated with the onset of snow melt for Dye 2 (Figure 1f). The afternoon 37H brightness temperatures also exceeded the threshold value on 1 July and on 26 June. The average volumetric liquid water content (m_v) in the upper 2 cm of the snowpack, as given by SNTHERM.89, shows the occurrence of melt during the afternoons of 22-24 June and 10-11 July (Figure 1e). On all three days during 22-24

* *Corresponding author address:* Thomas L. Mote, University of Georgia, Department of Geography, Athens, GA 30602-2502.

June, the volumetric water content of the upper 2 cm of the snowpack during the time of the afternoon SSM/I overpass was greater than 6 percent; it was also greater than 6 percent during the afternoons of 10 and 11 July. The surface air temperatures were at or above freezing during the afternoons of 22-24 June and 10-13 July (Figure 1a).

Melt was indicated in the upper 2 cm of the modeled snowpack before the afternoon SSM/I overpass on 28 June as the surface air temperature rose above freezing, but the model output indicates that the surface had refrozen by the time of the SSM/I overpass (Figure 1e). The 37H brightness temperature during the afternoon overpass of 28 June (188.3K) is less than the threshold value (201.1K), giving no indication of melt (Figure 1f). The model provides no indication of melt in the top 2 cm of the snowpack during the afternoon of 1 July, and the surface air temperature was 5K lower than the freezing point at the time of the SSM/I overpass. However, the 37H brightness temperatures during the afternoon overpasses were 236.2K at approximately 1800 UTC (1500 LST) and 213K at approximately 2000 UTC (1700 LST), which are both above the melt threshold value (Figure 1f). Although no melt was indicated in the top 2 cm, there was an indication of melt in the top 10 cm. The low density of the fresh snow that fell during the morning of 1 July (Figure 1a) may have allowed penetration of radiation further into the snowpack, resulting in liquid water below but not within the top 2 cm of the snowpack.

3.2 *Snow Grain Growth*

In one case, the model output indicated liquid water in the snowpack, but the 37H brightness temperatures were not elevated above the 201.1K threshold. The 11 July m_v for the top 10 cm of the snow showed approximately 3 percent volumetric water content during the morning, although the model output showed the top 2 cm as dry (Figure 1e). Although the model indicated some liquid water in the top 10 cm, the 37H brightness temperature for the 11 July morning overpass (184.3K) was below the 201.1K threshold (Figure 1f). This is in contrast to the observations and model output during the afternoon of 1 July, in which the model output showed liquid water in the snowpack below a dry layer, but with a relatively high brightness temperature (236.2K at 1800 UTC). This difference at first suggests that the model may not be adequately handling the percolation and refreezing of melt water in the snowpack, and the top 10 cm of the snowpack was actually dry on 11 July. However, one difference between the afternoon of 1 July and the morning of 11 July was that on 11 July the top 2 cm was a refrozen snow layer while on 1 July the surface of the snowpack was freshly fallen snow. The large-grained, refrozen upper layers on the morning of 11 July may have scattered the radiation emitted from the underlying wet layer, reducing the brightness temperature, while the fine-grained fresh snow on 1 July would not.

Melt-freeze metamorphism results in increased grain size, which increases the effect of volume scattering and reduces the brightness temperatures. At Dye 2, a result of this process is the downward trend in morning brightness temperatures from approximately 190K during early June to 170K in mid July. These changes appear in steps that correspond to the various melt periods. The morning brightness temperatures decreased from slightly greater than 190K during the first week of June to approximately 185K after the 9-17 June melt period (not shown). After the 22-24 June melt period, the morning brightness temperatures decreased to approximately 180K, and then decreased to about 170K during the melt period that began 9 July.

3.3 *Surface Energy Balance*

Both of the primary melt periods, 22-24 June and 10-11 July, were associated with relatively strong sensible heat components to the energy balance, greater than 40 W m^{-2} (Figure 1d). On each of those days, with the exception of 11 July, the shortwave radiation flux also exceeded 200 W m^{-2} (Figure 1b). Although the shortwave radiation flux peaked at less than 50 W m^{-2} on 11 July, significant cloud cover resulted in a positive longwave radiation flux. As a result, the peak net radiation flux on 11 July was almost equal to that of 10 July (Figure 1c).

The reason for melt occurrence on 1 July was due to a strong longwave radiation component. The longwave radiation flux was slightly positive for much of 28 June to 2 July. The same conditions also resulted in a marginal melt event on 2 July. The SNTHERM.89 model output indicated a small amount of liquid water in the upper 2 cm and some liquid water in the upper 10 cm on 2 July, although less than on 1 July (Figure 1e). The 37H brightness temperature was within 0.5K of the melt threshold on the afternoon of 2 July (Figure 1f). The melt event on 1-2 July also had a substantial latent heat component. The latent heat flux during 29 June to 3 July was near zero during the period of high relative humidity in the early morning hours, compared to more typical values of -50 W m^{-2} (Figure 1d). Possibly the lack of a strong shortwave radiation component is the reason the model produces melt deeper in the snowpack during 1-2 July than on 22-24 June and 10-11 July (Figure 1e).

The energy available to produce melt is more clearly indicated by examining the change in the heat storage of the snowpack (dQ). Five times during 21 June to 11 July

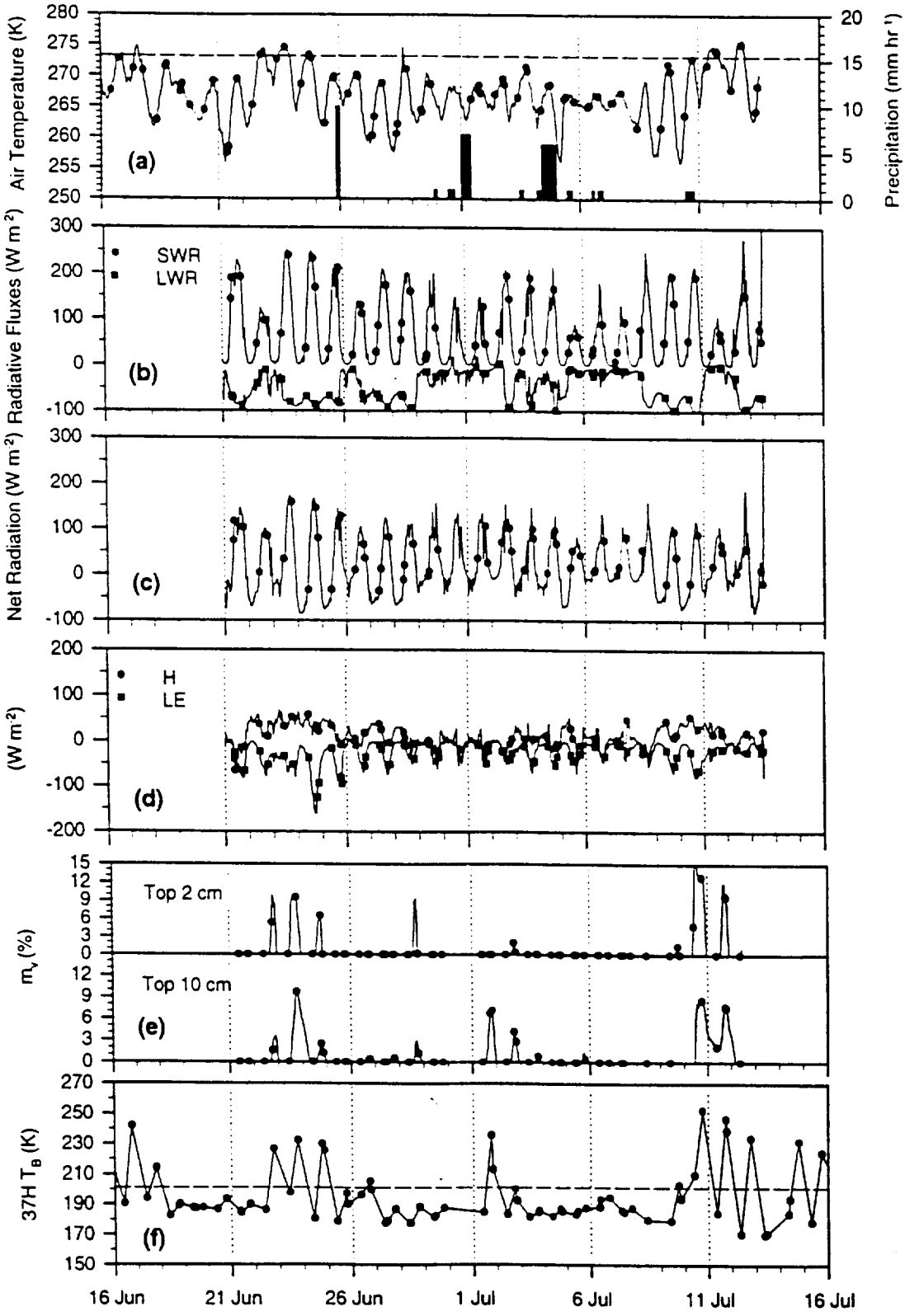

Figure 1. Hourly surface air temperatures (line) and precipitation (bars) (a); hourly shortwave (SWR) and longwave (LWR) radiative fluxes (b); modeled hourly net radiation flux (c); modeled hourly sensible (H) and latent (LE) heat fluxes (d); modeled hourly volumetric water content (e); and 37 GHz, horizontal polarization, brightness temperatures from SSM/I (f). Symbols indicate values concurrent with SSM/I overpasses.

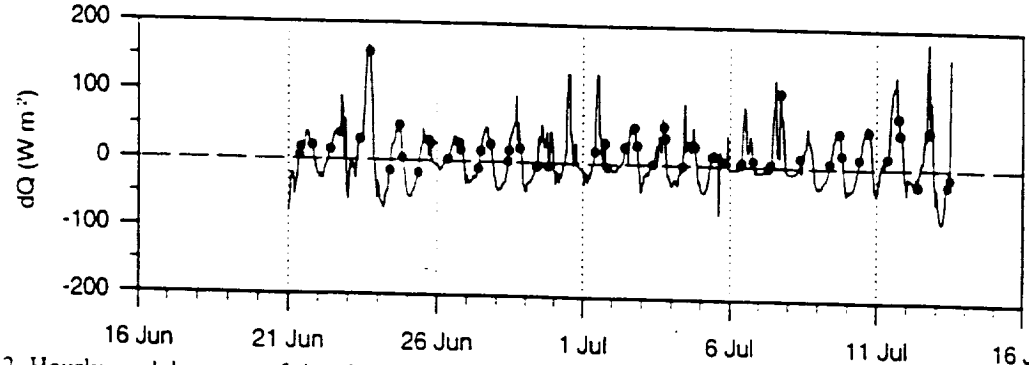

Figure 2. Hourly model output of the change in heat storage of the snowpack. Symbols indicate values concurrent with SSM/I overpasses.

dQ exceeded 100 W m^{-2} (Figure 2). Two of those instances, 23 June and 11 July, are clearly associated with surface melting. Two other instances occurred on 30 June and 1 July, associated with the 1-2 July surface melting. One instance in which dQ exceeded 100 W m^{-2}, 7 July, was not clearly associated with any surface melting. This occurred during a relatively prolonged cold period and after a fresh snowfall (Figure 1a). The energy added to the snowpack on 7 July was not sufficient to induce melting.

4. CONCLUSION

Diurnal melt-freeze cycles that occurred during mid June to early July are evident both by an increase in the microwave brightness temperatures and from the formation of liquid water as shown in the SNTHERM.89 model output. These time series demonstrate that a brightness temperature threshold for a single channel of microwave data can be used for melt identification, particularly if other geophysical characteristics of the snowpack are also considered. Additionally, the effects of melt-freeze metamorphosis of the snow and new snow accumulation are evident in the brightness temperature time series. The majority of the liquid water was a result of large shortwave radiation and sensible heat components, although there is evidence of melt induced primarily by downwelling longwave radiation.

Due to the relatively coarse resolution of passive microwave data, heterogeneous snow conditions within a scan cell introduces difficulty in interpreting the microwave data. This is particularly true when comparing surface conditions at one point to scan cells that may include information from nearly 50 km away from the location of interest. The use of modeled snowpack conditions, as has been done in this work, is suggested as an alternative to the use of firn cores or snow pits. The modeled conditions are likely more representative of the average conditions within the sensor's footprint than any individual core or pit.

5. REFERENCES

Jordan, R., 1991: A one-dimensional model for a snow cover: technical documentation for SNTHERM.89. *Special Report 91-16*, U.S. Army Corps of Engineers, Cold Regions Research and Engineering Laboratory, Hanover, NH.

Mote, T.L., and M.R. Anderson, 1995: Variations in snowpack melt on the Greenland ice sheet based on passive-microwave measurements. *J. Glaciol.*, **41**, 51-60.

Rowe, C.M., K.C. Kuivinen, and R. Jordan, 1995: Simulation of summer snowmelt on the Greenland ice sheet using a one-dimensional model. *J. Geophys. Res.*, in press.

Wentz, F.J., 1991: SSM/I Antenna Temperature Tapes User's Manual, Revision 1. Remote Sensing Systems, Santa Rosa, CA, 70 pp.

JOURNAL OF GEOPHYSICAL RESEARCH, VOL. 100, NO. D8, PAGES 16,265–16,273, AUGUST 20, 1995

Simulation of summer snowmelt on the Greenland ice sheet using a one-dimensional model

Clinton M. Rowe and Karl C. Kuivinen

Meteorology/Climatology Program, Department of Geography, and Snow and Ice Research Group, University of Nebraska-Lincoln

Rachel Jordan

Geophysical Sciences Branch, U.S. Army Cold Regions Research and Engineering Laboratory, Hanover, New Hampshire

Abstract. A one-dimensional heat and mass balance model of a snowpack over frozen soil was modified for use in glacial environments. The model solves a set of governing equations for the energy and mass balances of the snow, subject to observed meteorological conditions at the upper boundary and the assumption of a steady state at the lower boundary. The initial state of the snowpack is defined by the temperature, density and grain size profiles at the beginning of the simulation period. The data used to test the model on the Greenland ice sheet are a subset of the meteorological and surface data collected during the 1990 summer field season by the Swiss Federal Institute of Technology (ETH) Greenland Expedition. The site was located near the equilibrium line elevation on the west slope of the ice sheet. The relatively large amount of snowmelt experienced at this site during the summer of 1990 provides a robust test of the snowmelt model. Both the simulated height and mass of the snowpack agree well with the observations. The evolution of profiles of temperature, density and liquid water content also conform to our expectations of the physical changes taking place in the snowpack during melt. Results from the present model are also compared to those from a similar model and differences between the models are discussed.

Introduction

The Greenland ice sheet exerts an influence on the atmosphere, at least at a regional scale, due to the combined effects of its elevation, surface temperature and albedo. In turn, the mass balance of the ice sheet depends on the relationship between the ice sheet and its climatic environment, especially in terms of the mass and energy exchanges that take place at the surface of the ice sheet. Simply stated, the average net mass balance of the entire ice sheet is determined by evaluating the difference between accumulation and ablation at many individual points throughout the entire area. However, the response of the ice sheet to natural or human-induced variations in climate is incompletely understood due to the complex interactions between the ice sheet and the atmosphere at various spatial and temporal scales. For example, a warming of the atmosphere over Greenland would be expected to increase ablation from the ice sheet resulting in a negative mass balance [*Van der Veen*, 1987; *Braithwaite*, 1990; *Braithwaite and Olesen*, 1990a; *Warrick and Oerlemans*, 1990; *Huybrechts et al.*, 1991]. Increased ablation would be due not only to increased sensible heat and longwave radiation fluxes to the ice sheet resulting in greater melt, but also to an increase in the area of the ablation zone and to a longer melt season. However, the increase in atmospheric water vapor that would accompany the temperature rise could result in increased precipitation over all or part of the ice sheet, partially or completely offsetting the increased ablation [*Van der Veen*, 1987; *Warrick and Oerlemans*, 1990; *Huybrechts et al.*, 1991].

Copyright 1995 by the American Geophysical Union.

Paper number 95JD01384
0148-0227/95/95JD-01384$05.00

Many studies of the mass balance of the Greenland ice sheet have parameterized ablation as a function of temperature, either alone or in combination with other variables such as wind speed [*Braithwaite*, 1990; *Huybrechts et al.*, 1991; *Reeh*, 1991]. For estimation of the current mass balance of the ice sheet, these parameterizations appear to be adequate, but they are inappropriate for the investigation of ice sheet mass balance in a changing climate. This is because of feedbacks between the ice sheet and the climate system that are not considered explicitly by the parameterizations and because the parameterizations might not remain valid under a changed climate due to extrapolation errors. Furthermore, because air temperature is a state variable, it will respond not only to changes in the climate, but also to any changes to the ice sheet itself.

Energy balance and degree-day models that incorporate the physics of snowmelt and reliable measurements of ice thickening and thinning rates can provide insight into the ice processes that might be affected by climate change [*Braithwaite*, 1990; *Braithwaite and Olesen*, 1990a,b]. It is the purpose of this investigation to employ an energy balance model to investigate the processes affecting mass balance at a specific site near the equilibrium line elevation [*Ohmura et al.*, 1991]. For this study, a one-dimensional model of snowpack physics that was originally developed at the Army Corps of Engineers Cold Regions Research and Engineering Laboratory (CRREL) [*Jordan*, 1991] has been employed. This model originally was formulated to consider snow over frozen ground, so that only a few modifications were necessary to implement the model for the case of interest (i.e., snow over firn/ice). The model solves a set of governing equations for the energy and mass balances of the snow, subject to observed meteorological conditions at the upper boundary and the assumption of a steady state at the lower boundary, from an initial state defined by the temperature, density and grain size profiles at the beginning of the simulation period.

Model Summary

General Methodology

The one-dimensional mass and energy balance model used in this study (SNTHERM) was developed for predicting temperature profiles within layered frozen media. It was partially based on the earlier work of *Anderson* [1976] and is similar in many respects to other recent mass and energy balance models for snow [*Akan*, 1984; *Bader and Weilenmann*, 1992; *Brun*, 1989; *Greuell and Oerlemans*, 1986; *Illangasekare et al.*, 1990; *Jordan*, 1983; *Loth*, 1993; *Morris*, 1987]. In addition to temperature prediction, SNTHERM simulates the various physical and hydrological processes within a snow cover, including water flow, compaction, grain growth, snow ablation, and snow accumulation. Only thermal processes are modeled for soil layers, and therefore a sink is included at the snow-soil interface which artificially drains infiltrating water when it reaches the soil. The snow or soil layers are modeled as mixtures of five constituents: dry soil material, dry air, ice, liquid water, and water vapor, denoted by the subscripts d, a, i, l, and v, respectively. The partial or bulk density (γ_k) of each constituent k is related to its intrinsic density (ρ_k) as

$$\gamma_k = \theta_k \rho_k , \tag{1}$$

where θ_k is the fractional volume. For this study of snow ablation over an ice sheet, it was possible, with minor modifications to the model, to treat the ice as a soil layer with no dry soil component, as indicated in Figure 1. This procedure made advantageous use of the intralayer drain in the model and avoided problems of ponding water, which are not handled in SNTHERM. To be succinct, references to the dry soil fraction are omitted from the equations in the following summary.

SNTHERM uses a control volume numerical procedure to describe the spatial domain [*Patankar*, 1980] and a Crank-Nicholson weighting scheme for the time domain. The conceptual grid used in the numerical solution is shown in Figure 1. In order to accommodate compaction of the snow cover, the control volume thickness is allowed to change over time. This is not the usual practice, but is efficient numerically since the control volume boundaries remain coincidental with the stratigraphy of the evolving snow cover. The mass of ice and water is assumed to be conserved under contraction of the control volume, whereas the displaced portion of air and water vapor are expelled. Governing sets of equations are linearized with respect to the unknown variables and solved by the Thomas or tridiagonal matrix algorithm (TDMA) [*Patankar*, 1980]. For each time step, the mass balance equations are solved first and the water flux and snow density from this computation are used in the subsequent solution of the energy equation. Readers desiring further details on the numerical methods of SNTHERM or on the governing equations are referred to *Jordan* [1991].

Conservation Equations

One-dimensional mass balance equations for the total snow medium and the three water constituents, respectively, are of the form

$$\frac{\partial}{\partial t}\int \rho_s dz = -\sum_{k=i,v}\sum_{S} \boldsymbol{J}_k \cdot \boldsymbol{n} \tag{2}$$

and

$$\frac{\partial}{\partial t}\int \gamma_k dz = -\sum_{S} \boldsymbol{J}_k \cdot \mathbf{n} + \sum_{k'=i,l,v} \int M_{kk'}\, dz (1-\delta_{k'k}) \tag{3}$$

where t is time, ρ_s is the overall snow density, z is the vertical position relative to the snow-soil interface, dz is the incremental control volume thickness, $\boldsymbol{J}_k$ is the flux of water constituent k (positive upwards), $\mathbf{n}$ is a unit vector normal to the surface of the control volume, and $\sum_S$ indicates a summation over the top and bottom surfaces of the control volume. The source terms M_{li}, M_{vl} and M_{vi} are the mass rates of melt, evaporation, and sublimation, respectively, $\delta_{kk'}$ is the Kronecker delta, and $M_{kk'} = -M_{k'k}$.

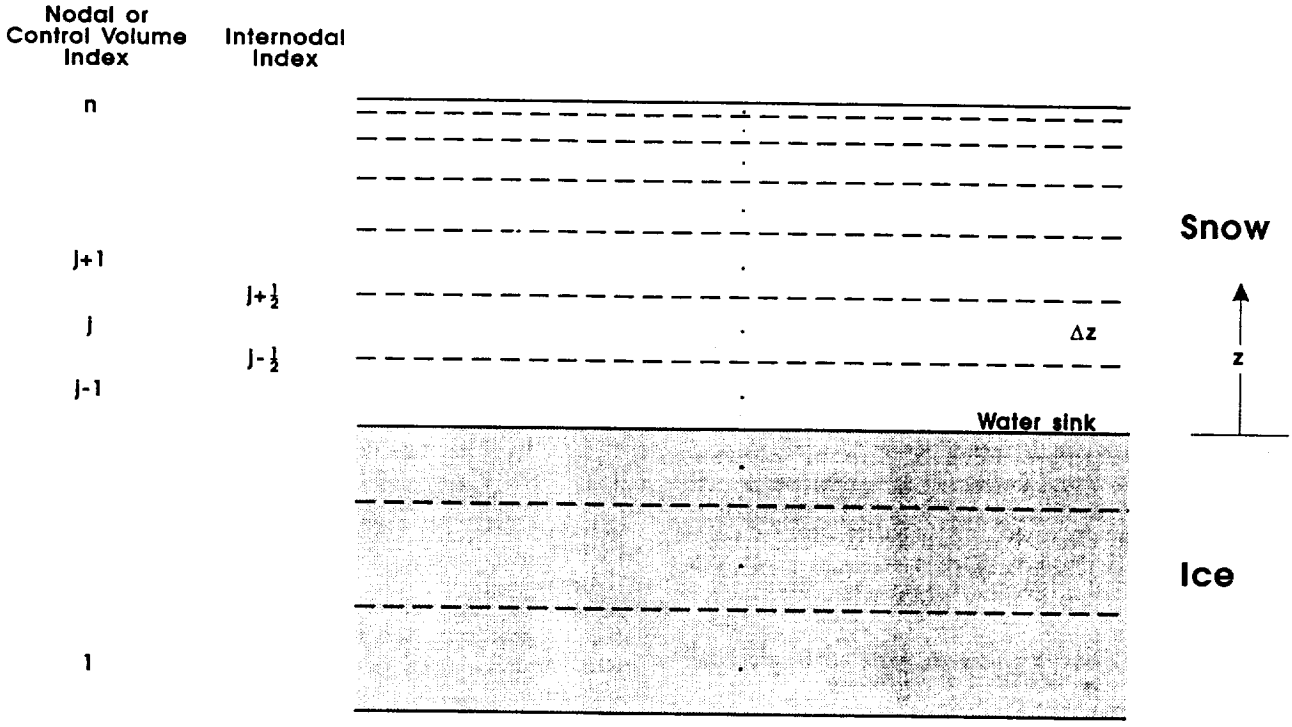

Figure 1. One dimensional grid for a two-layer system of snow over ice. The ice layer is treated as a soil without a dry soil component.

Air within the pore space is assumed to be stagnant and incompressible so that the vapor flux is driven by diffusion only. With the further assumption that the air is saturated, the vapor flux is computed from Fick's law as

$$J_v = -D_e \frac{\partial \rho_{v,sat}}{\partial z} = -D_e \frac{\partial \rho_{v,sat}}{\partial T} \frac{\partial T}{\partial z}, \quad (4)$$

where $\rho_{v,sat}$ is the intrinsic water vapor density at saturation, and D_e is an effective diffusion coefficient for vapor flow through snow which takes into account condensation and sublimation of vapor on the ice grains. Having specified that the control volume remains coincidental with the compacting snow cover, the mass flux of ice is taken as 0. Movement of liquid water through snow is assumed to be governed by Richards' equation [*Richards*, 1931]. Since capillary forces within snow are usually 2 to 3 orders of magnitude less than those of gravity [*Colbeck*, 1971], they are neglected, and the liquid water flux is expressed as

$$J_l = \frac{K_l}{\mu_l} \rho_l^2 g, \quad (5)$$

where K_l is the hydraulic permeability, g is the gravitational constant, ρ_l is the density of water, and μ_l is the dynamic viscosity of water. The formula of *Brooks and Corey* [1964] is used for estimating K_l

$$K_l = K_{max} s_e^{\epsilon}, \quad (6)$$

where s_e is the effective saturation $(s - s_r)/(1 - s_r)$, s is the liquid water saturation, s_r is the residual liquid water saturation, K_{max} is the saturated permeability computed from the formula of *Shimizu* [1970] and the parameter ϵ is taken as three [*Colbeck and Anderson*, 1982]. Discounting evaporative changes, the water flow equation is formulated from the equation for liquid water continuity as

$$\rho_l (1 - s_r) \frac{\partial}{\partial t} \int s_e \phi \, dz = \frac{\rho_l^2 g}{\mu_l} \sum_S (K_{max} s_e^3 \mathbf{k}) \cdot \mathbf{n} + \int M_{li} \Delta z \quad (7)$$

where $\mathbf{k}$ is a unit vector in the upwards vertical direction. The snow porosity ϕ changes with time and is related to M_{li} through the continuity equation for ice.

The water infiltration pattern generated by (7) consists of a step function in the vertical direction and even wetting in the horizontal direction. Whereas this simplified simulation of the flow pattern is adequate for many modeling purposes, it is important to note that it is not a realistic description. The actual flow pattern is almost always in the form of fingers, which disperse the leading edge of the infiltration wave and accelerate its arrival at the bottom of the snow cover [*Colbeck*, 1979; *Marsh and Woo*, 1984]. In addition, discontinuities in hydraulic permeability and capillary tension between heterogeneous snow layers result in horizontal flow along these textural boundaries. There is also an uncertainty associated with the selection of the residual saturation, since it must be satisfied prior to the advancement of the water front and therefore directly affects the infiltration rate. Moreover, the amount of water retained by the snowpack and the snow density are directly related to this parameter. A summary by *Kattelmann* [1986] on measurements of the residual water content ($\theta_r = s_r \phi$) shows a broad range of values from 0.0 to 0.4, with most lying between 0.01 and 0.05. A intermediate value of s_r=0.04 has been selected as the default value for the model.

The one-dimensional equation for the conservation of energy is written as

$$\frac{\partial}{\partial t} \int \rho_s h_s \, dz = -\sum_{k=l,v} \sum_S J_k h_k \cdot \mathbf{n} + \sum_S k_s \nabla T \cdot \mathbf{n} - \sum_S R_S \cdot \mathbf{n} \quad (8)$$

where h is the specific enthalpy taken with respect to the fusion point of water, k_s is the thermal conductivity of snow, and R_s is the net radiation. The general expression for enthalpy is

$$h = \int_{273.15}^{T} c(T) dT + L, \quad (9)$$

where c and L are the specific and latent heats, respectively. The first term in (8) represents the change in stored heat and the subsequent terms represent heat fluxes due to water flow, vapor diffusion, conduction, and solar radiation (R_S), respectively. Disregarding hysteresis effects, the unfrozen water content (γ_l) is related to temperature through an adaptation of the formula developed by *Guryanov* [1985] for soil

$$f_l = \frac{\gamma_l}{\gamma_w} = \frac{1}{1 + (a_1 T_D)^2}, \quad (10)$$

where T_D is the temperature depression (273.15 – T), and $\gamma_w = \gamma_l + \gamma_i$. A value of $a_1 = 100$ was selected to provide a reasonably sharp curve (99% of the water is frozen at -0.10°C) while avoiding the numerical difficulties associated with too steep a slope. Sensible and latent heat changes are combined in an apparent heat capacity (c_{app}) as

$$c_{app} = c_s + L_{li} \frac{\partial f_l}{\partial T} + L_{vi} \frac{\theta_v}{\gamma_w} \frac{\partial \rho_{v,sat}}{\partial T}, \quad (11)$$

where c_s is the specific heat of the total snow medium, and L_{li} and L_{vi} are the latent heats of fusion and sublimation, respectively.

The solar absorption term in (8) depends primarily on the intensity, angle, and spectral composition of the incident radiation, and on snow albedo, optical depth, and grain diameter. As a first approximation, incident solar energy is assumed diffuse and isotropic, and is divided at 1.12 μm into components corresponding roughly to the visible and to the near and midinfrared regions of the spectrum. Infrared radiation is assumed to be totally absorbed within the top node, and visible radiation to decay according to Beer's law, where the asymptotic bulk extinction coefficient β_∞ is computed from the formula of *Bohren and Barkstrom* [1974]

$$\beta_\infty = \frac{0.003795 \gamma_w}{\sqrt{d}}, \quad (12)$$

using a value of 0.003795 suggested by *Anderson* [1976]. A value of 0.78 is set as a default for the albedo of snow, and 55% of the net solar radiation is considered to be in the near and midinfrared wavebands.

Snow Cover Metamorphism

The deformation rate of the snow cover takes into account settling due to metamorphism, compaction under the sustained pressure of the snow overburden and loss of snow structure during active melt, giving

$$\frac{\partial}{\partial z} \frac{\partial z}{\partial t} = \left[\frac{\partial}{\partial z} \frac{\partial z}{\partial t} \right]_{metamorphism} + \left[\frac{\partial}{\partial z} \frac{\partial z}{\partial t} \right]_{overburden} + \left[\frac{\partial}{\partial z} \frac{\partial z}{\partial t} \right]_{melt}, \quad (13)$$

where the algorithms for the first two mechanisms follow *Anderson* [1976]. Mass losses for nodes undergoing melt are compensated by a reduction in the control volume thickness so that a constant ice density is maintained. In addition to compaction, water and vapor flows are factors in the overall densification of the snow cover. If a control volume mass or thickness falls below prescribed minimums, either through melt, sublimation, or compaction, it is automatically combined with a neighboring volume.

The grain growth function for dry snow is an adaptation of a formula used to predict growth by sintering in metals and ceramics [*Stephenson*, 1967; *Gow*, 1969]. This function is directly related to vapor flux which provides the necessary vapor source for growth and inversely related to particle size. There is a marked increase in grain growth within wet snow [*Colbeck*, 1982]. The growth function in this case is related to liquid water content and is again inversely related to grain size, with a maximum size set at 3 mm.

Boundary Conditions

Upper boundary conditions at the snow surface are prescribed by meteorologically determined fluxes of mass and energy. The surface energy flux (I) is expressed as

$$I = -R_s\downarrow(1-\alpha_s) - R_L\downarrow + R_L\uparrow + I_{sens} + I_{lat} + I_{conv} , \quad (14)$$

where $R_s\downarrow$ is the energy flux of downwelling solar radiation, α_s is the snow albedo, $R_L\downarrow$ and $R_L\uparrow$ are the energy fluxes of downwelling and upwelling longwave radiation, I_{sens} and I_{lat} are the turbulent fluxes of sensible and latent heat, and I_{conv} is the heat convected by rain or falling snow. Solar radiation is estimated from the three-layer insolation model of *Shapiro* [1982, 1987], and the downwelling longwave flux is computed from the formula of *Idso* [1981], with the addition of the Wachtmann correction [*Hodges et al.*, 1983]. The upwelling longwave flux is expressed as

$$R_L\uparrow = \varepsilon_s \sigma T_0^4 + (1-\varepsilon_s) R_L\downarrow , \quad (15)$$

where the first term on the right is the longwave emission from the snow as a function of the surface temperature (T_0) and the emissivity of the snow (ε_s) and the second term is reflected downwelling longwave radiation. A value of 0.97 is used for the snow emissivity [*Jordan et al.*, 1989]. The turbulent fluxes are given by [*Andreas and Murphy*, 1986]

$$I_{sens} = -\rho_a c_a C_H w (T_a - T_0) \quad (16)$$

and

$$I_{lat} = -L_v C_E w (\rho_{v,a} - \rho_{0v,sa}) , \quad (17)$$

where ρ_a is the air density, c_a is the specific heat of air at constant pressure, C_H is the bulk transfer coefficient for sensible heat, C_E is the bulk transfer coefficient for latent heat, w is the wind speed and $\rho_{v,a}$ is the vapor density in air, which is computed using the relative humidity. The bulk transfer coefficients are taken as equal and, assuming neutral stability, are computed from the roughness length (z_0) as

$$C_{EN} = C_{HN} = \frac{k^2}{\left[\ln\left(\frac{Z}{z_0}\right)\right]^2} , \quad (18)$$

where Z is the observation height above the snow interface. For nonneutral atmospheric conditions, the standard stability adjustment is made to C_{EN} and C_{HN} [*Large and Pond*, 1982; *Jordan*, 1992].

Rainfall and the turbulent exchange of water vapor provide the upper boundary fluxes in the mass balance and water flow equations, where the vapor flux is computed as the turbulent flux of latent heat divided by L_v. Additional nodes are added on top of the snow cover when snowfall occurs, using a default density of 100 kg m^{-3} for the new snow.

As the bottom boundary condition for the energy equation, a constant temperature of -8.9°C is assumed at a depth of 10 m, since the 10 m temperature is nearly constant on an annual basis [*Paterson*, 1980]. No lower boundary is required for the water flow equation when the gravitational approximation is used.

Data

The data used to test the model on the Greenland ice sheet are a subset of the meteorological and surface data collected during the 1990 summer field season by the Swiss Federal Institute of Technology (ETH) Greenland Expedition [*Ohmura et al.*, 1991]. The site was located near the equilibrium line elevation on the west slope of the ice sheet (69°34′25.3″N, 49°17′44.1″W, 1175 m above sea level (asl)). This site was originally chosen because the location of the equilibrium line should be a sensitive indicator of the relationship between glacier mass balance and climate variations [*Ohmura et al.*, 1992]. For the purpose of the current research, the relatively large amount of snowmelt experienced at this site during the summer of 1990 provides a robust test of the snowmelt model. In addition, data from this site were used by *Greuell and Konzelmann* [1994] to optimize and test an energy and mass balance model. These two models are similar in some respects but have significant differences in their formulation, initialization, and use. Results from the present model will be compared to those of *Greuell and Konzelmann* [1994], and the differences between the models will be discussed below.

Meteorological Data

Meteorological data (air temperature, relative humidity, wind speed, cloud cover, and precipitation) at 6-hour intervals from the ETH site were published for the entire field season. A subset of the data from JD 163 (June 12) to JD 212 (July 31) was extracted from the ETH data for use with the snowmelt model. This period begins at the first observation with all of the data needed to run the snowmelt model, and ends soon after the snowpack has completely melted. Before using the published data, missing and invalid air temperature data were estimated from the preceding and following observations, and two obvious typographical errors in relative humidity were corrected. Because the model uses linear interpolation to estimate meteorological variables at model time steps between observations, it was thought necessary to preprocess the data to create an hourly meteorological data set for input to the model. Hourly air temperature, relative humidity, and wind speed were estimated from the published data using cubic spline interpolation. Because of the difficulty associated with interpolating cloud type, both cloud cover and cloud type were held constant over a 6-hour period centered on the observation (i.e., for the hour of observation, the 3 hours preceding and 2 hours following). Precipitation was distributed over the 6-hour period preceding the observation so as to preserve the correct 6-hour precipitation total. With the exception of days 167 and 168, all the precipitation fell as rain. The resulting hourly data were converted to the proper units for input into the snowpack model (Figure 2). Because detailed radiation data were not published in a format that could be used in the model, they were estimated using the algorithms provided in the SNTHERM code.

Snowpack Data

The snowmelt model requires initial vertical profiles of temperature, density, and grain diameter for the snowpack and the underly-

ing substrate. Temperature and density profiles were estimated from published figures for the ETH site [*Ohmura et al.*, 1991]. The ETH scientists measured snowpack temperatures at six depths (initially 0, 19, 38, 57, 76, and 95 cm above the snow/ice interface) using thermistors inserted approximately 50 cm horizontally into the wall of a pit, which was subsequently filled. Measurements were made at 0000, 0600, 1200 and 1800 UT daily. Englacial temperatures were measured daily using thermistors mounted on cables that were lowered into holes drilled into the ice. A total of six such cables were used by the ETH scientists in 1990 [*Greuell*, 1991b]. To initialize SNTHERM, the snowpack temperatures were estimated for 0000 UT on JD 163 (June 12), while englacial temperatures to 10 m were estimated for the previous day. Since englacial temperatures can be expected to vary only slowly at the beginning of the summer, this should not introduce any significant errors into the initial temperature profile.

Mass balance measurements were made by the ETH scientists 4 times per day using five stakes set into the snow approximately 10 m apart. These snowpack heights were averaged to give a value representative of the change in height of the snowpack. Once per day, generally around 1800 UT, vertical profiles of density and liquid water content were obtained from the wall of a pit dug into the snowpack. Several different methods were used by the ETH scientists to measure density. The values used to initialize SNTHERM were interpolated from a graph presenting the density profile as measured at 5 cm intervals with a 500 cm^3 cylinder inserted horizontally into the pit wall. Raw density measurements were corrected before plotting to correspond to density measurements made using a large cylinder vertically inserted into the snowpack. Density estimates could not be made for the first day of simulation, but were obtained for JD 167 (June 16). Again, in the absence of significant melt, this should not introduce significant initialization errors. Liquid water content estimates were calculated from measurements of the dielectric constant of the snow made concurrently with the density profiles.

The initial grain size profile was estimated from descriptions contained in the ETH report. The grain sizes used to initialize the model are comparable to those estimated as a function of density [*Anderson*, 1976].

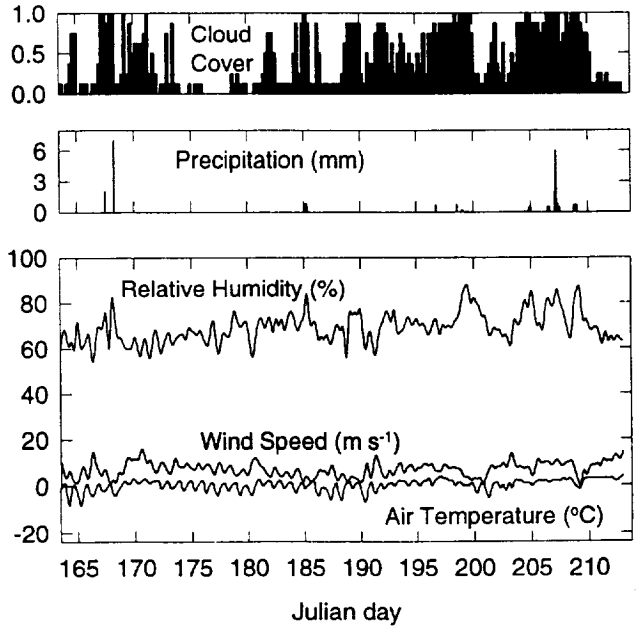

Figure 2. Meteorological conditions at the ETH site for input to the model.

Table 1. Snowpack Parameters Used in SNTHERM

Parameter	Default	Site-Specific
Roughness length (z_0)	0.007	0.001
Ratio of neutral stability bulk turbulent transfer coefficients of momentum and latent heat (C_{DN}/C_{EN})	1.5	1.0
Ratio of neutral stability bulk turbulent transfer coefficients of momentum and sensible heat (C_{DN}/C_{HN})	1.0	1.0
Windless exchange coefficient for latent heat (E_{E0})	0.0	0.0
Windless exchange coefficient for sensible heat (E_{H0})	1.8	1.0
Fractional humidity in snow (f_m)	1.0	1.0
Albedo (α)	0.78	0.70
Irreducible or residual liquid water saturation (s_r)	0.04	0.02

Results

Three model runs were made for a 50-day period from JD 163 (June 12) to JD 212 (July 31) 1990. The first run used the default snow properties (Table 1) given by *Jordan* (1990) for midlatitude seasonal snowpacks. This run left approximately 20 cm of snow on top of the ice at the end of the run, even though the actual snowpack had melted 2 days earlier (Figure 3). Most of the disagreement between the model and the observations arises from two periods (JD 176-178 and JD 186-189) when modeled mass loss occurs more slowly than observed.

The second run used snow properties chosen to be representative of the ETH site (Table 1). Roughness length was reduced to a value consistent with the relatively flat snow-covered terrain [*Arya*, 1988], the ratio of the turbulent transfer coefficients for latent heat and momentum was set to unity, the windless convection coefficient for sensible heat was set to zero, and the irreducible liquid water saturation was reduced by half. In terms of the mass balance, however, the most significant change was the reduction of the snow albedo from the default value to a value computed as a weighted average of the June and July monthly albedos reported by *Konzelmann* [1991] for the ETH site. Since the two periods of greatest discrepancy in the initial run were characterized by little or no cloud cover (Figure 2), the reduction in solar heating due to a too high albedo would be a likely cause. For this run, the height of the snowpack is reduced more rapidly than was the observed snowpack until just prior to the end of the run (Figure 3), and the modeled snowpack disappears less than 2 days after the observed. The mass of the snowpack is modeled closely until the last 5-6 days of the model run, when mass is removed too slowly. It must be noted that the observed mass was computed by *Greuell and Konzelmann* [1991] as the product of the snowpack height and an average snowpack density. Before JD 203 (July 22), they used as the density of snow a 5-day running mean of the density obtained by inserting the large cylinder vertically into the snowpack. From JD 203 to JD 210 (July 29), they used a constant snowpack density of 439 kg m^{-3} and after JD 210, a constant value of 300 kg m^{-3}. Ice lenses and slush were assumed to have densities of 900 kg m^{-3} and 950 kg m^{-3}, respectively. Therefore because of measurement errors

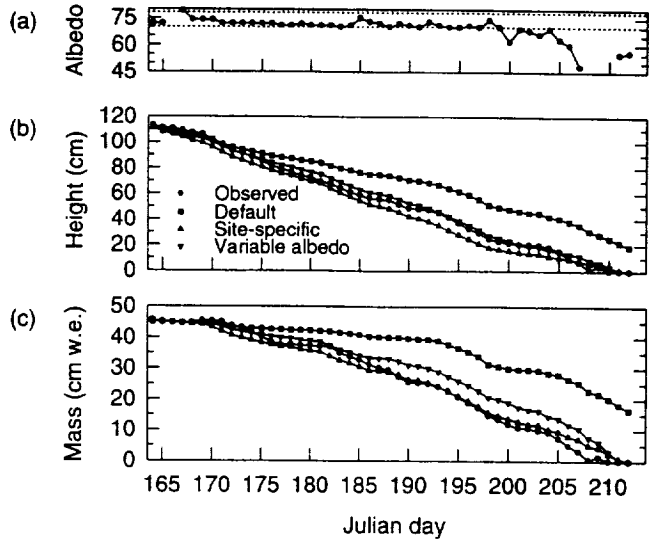

Figure 3. (a) Daily observed albedo (percent), with constant albedos used in runs 1 and 2 marked; (b) daily observed and modeled snowpack height (centimeters); and (c) daily observed and modeled snowpack mass balance (centimeters water equivalent).

and horizontal inhomogeneities, the observed mass balance may only be representative of the immediate area in which the measurements were taken (i.e., approximately 10 x 20 m), while the model results, based on the more spatially homogeneous climatic parameters, may actually represent more spatially averaged values.

Because the SNTHERM model assumes a constant albedo, the average albedo specified for the second run is initially too low, then becomes too high for the final 10-12 days of the run. This corresponds to the errors in the modeled mass balance, with mass being lost too quickly at the beginning of the run (i.e., absorption of solar radiation too high) and too slowly at the end of the run. To overcome this problem, a third run was performed in which the albedo was specified on a daily basis using observed values from *Greuell* [1991a]. This run gives better overall agreement with the observed snowpack height during the period than did the previous runs. However, the snowpack mass balance is not modeled as well as by the second run.

Further discussion of the evolution of the snowpack temperature, density and liquid water content profiles will be based on the results of the final model run using the site-specific snowpack properties and a variable albedo.

Snowpack Temperature

Both the actual and modeled snowpacks (Figure 4) become temperate (i.e., isothermal at 0°C) by JD 171 (June 20). The modeled snowpack (Figure 4b) remains essentially isothermal for the remainder of the simulation, but shows a diurnal variation in the upper 10-20 cm of the pack in response to the diurnal air temperature and radiation cycle.

Snowpack Density

Densities in the observed and simulated snowpacks (Figure 5) increase over time, as is expected, due to snow metamorphism. However, the density of the layer closest to the underlying ice becomes too high in the simulation, beginning about JD 175 (June 24) in the lowest 5 cm of the snowpack and growing to about 20 cm by JD 200 (July 19). This density increase is caused by liquid water from melt higher in the snowpack infiltrating and refreezing near the underlying ice and is responsible for much of the discrepancy between the simulated and observed mass. Once this dense layer forms, it reduces the infiltration rate of meltwater and continues to grow. Physically, this may be representative of the growth of superimposed ice as often occurs in the ablation zone of the ice sheet. Measurements of superimposed ice at the ETH camp indicated that it varied in thickness between 3 and 6 cm between JD 183 (July 2) and JD 202 (July 21) [*Greuell and Konzelmann*, 1991]. The actual snowpack at the ETH site, however, developed a slush layer beginning on JD 181 (June 30) that is not reproduced by the model since any liquid water reaching the ice surface is immediately drained away. If liquid water were allowed to accumulate in the lowest layers of the model snowpack, it would be more difficult for refreezing to occur and a slush layer could perhaps be formed. Slow drainage of liquid water from this slush layer would also improve the simulation of snowpack mass.

Snowpack Liquid Water Content

The bulk of the snowpack has volumetric liquid water content of 2-6% from JD 169 (June 18) through JD 197 (July 16) in both the observations and the simulation (Figure 6). In general, the simulated liquid water content is somewhat lower than the observed values, but since these measurements were made in the late afternoon, they may correspond more closely to daily maximum

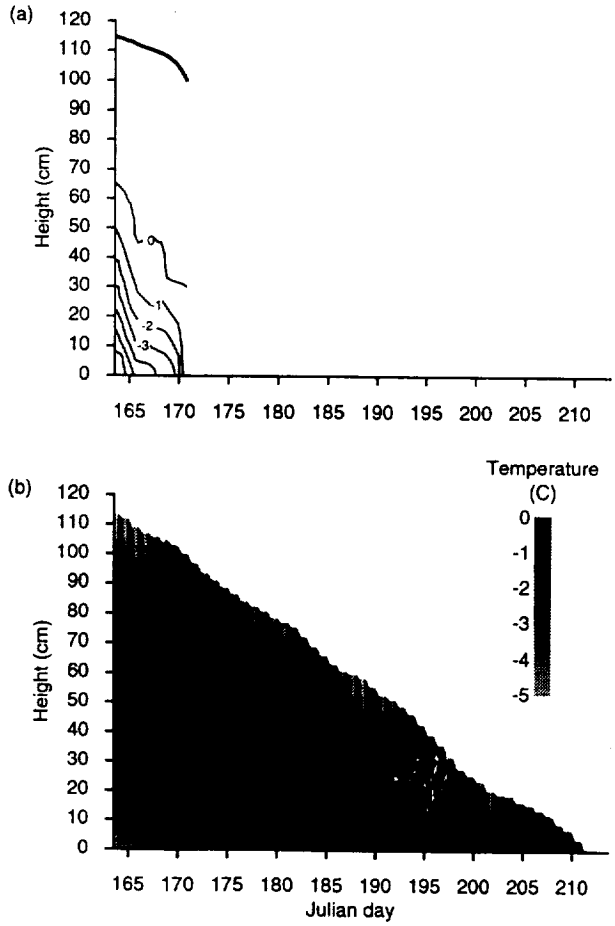

Figure 4. Time-height profile of (a) observed [adapted from *Greuell*, 1991b] and (b) modeled snowpack temperature (°C). The observed snowpack became isothermal at 0°C on JD 170 (June 19). The heavy line in (a) indicates the top of the snowpack.

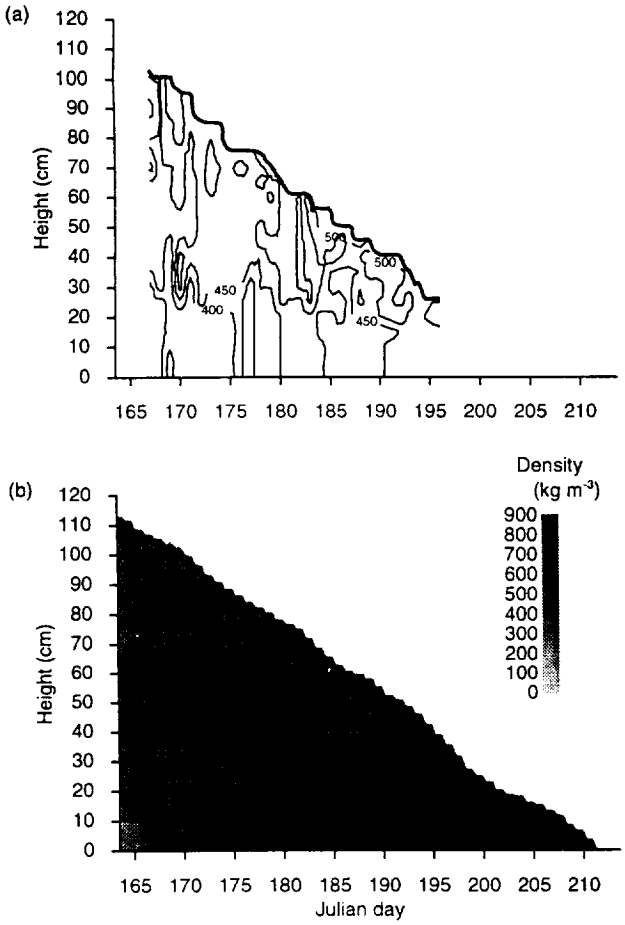

Figure 5. Time-height profile of (a) observed [adapted from *Greuell and Konzelmann*, 1991] and (b) modeled snowpack density (kilogram per cubic meter). Observed density profiles were not available after JD 196 (July 15). The heavy line in (a) indicates the top of the snowpack.

liquid water contents than to daily average values. In the simulated snowpack, liquid water content is higher above the denser snow layers since the rate of drainage through the snowpack largely is determined by the density of the snow. The lowest part of the simulated snowpack is too dry after about JD 175 (June 24). This is the same layer that became too dense at about the same time. The upper part of the snowpack, to depths of about 15-30 cm, experiences a diurnal cycle of liquid water content that corresponds to the melt/refreeze cycle in the upper portion of the snowpack.

Energy Fluxes

Time series of the daily energy fluxes between the snowpack and both the atmosphere and the underlying ice (Figure 7) show that sensible heat flux and net radiation are positive throughout the simulation. Thus these two terms provide the energy source for snowmelt, while latent heat flux and conduction into the ice are energy sinks and reduce the energy available for melt. Melt is more highly correlated with net radiation (r^2= 0.809) than with sensible heat flux (r^2= 0.076). This is contrary to the findings of Braithwaite and Olesen [*Braithwaite*, 1981; *Braithwaite and Olesen*, 1984, 1990b]. They attribute their results to the greater temporal variability, and therefore greater covariability with melt, of sensible heat flux as compared to net radiation. For this simulation, however, net radiation and sensible heat flux have nearly equal variance, but net radiation represents the larger energy source for melt and thus results in a greater temporal correlation.

Model Intercomparison

Greuell and Konzelmann [1994] present results of a numerical model of the surface energy and mass balance at the ETH site for 1990. As with SNTHERM, their model uses air temperature and humidity, wind speed, cloud amount, and precipitation as input. However, unlike SNTHERM, the parameterizations used in their model to compute the various flux terms were, for the most part, developed for the ETH site specifically or for Greenland. In addition, their simulations made use of measured, rather than computed, radiation fluxes. Two significant differences between the models are their (1) incorporation of a snow albedo parameterization based on density and cloud cover and (2) inclusion of a slush layer as compared to SNTHERM's prescribed albedo and free drainage.

Initial profiles of temperature, density and liquid water content were prescribed on JD 152 (June 1) as a uniform temperature of -8.8°C within the ice to a depth of 25 m and a linear increase from that value at the snow/ice interface to 0°C at the surface, a constant snowpack density of 380 kg m^{-3}, and dry snow (i.e., no liquid water present). They ran their model until JD 249 (September 6), resulting in the ablation of approximately 18 cm of ice.

Following an initial model run, Greuell and Konzelmann tuned the model to provide good agreement with the mass balance and

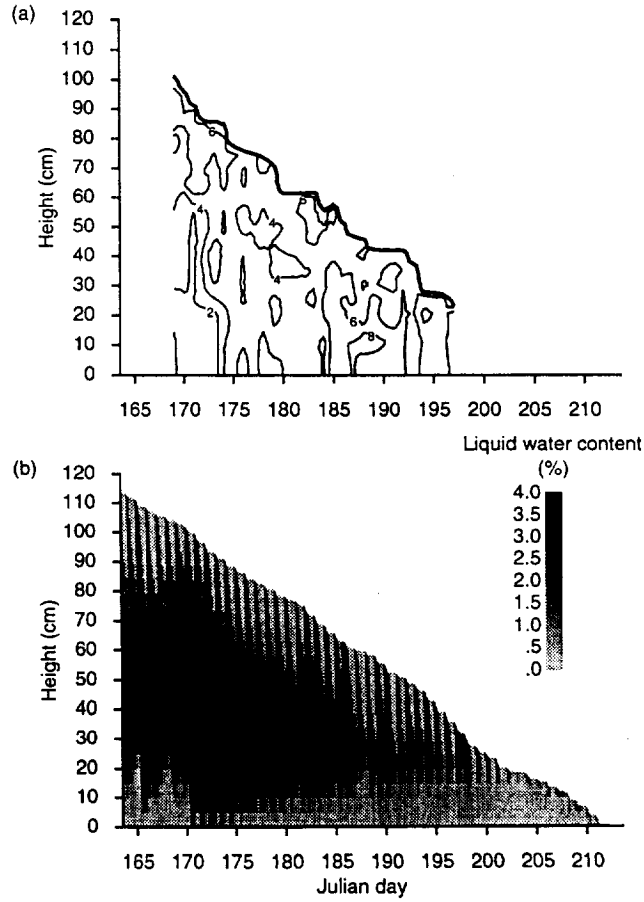

Figure 6. Time-height profile of (a) observed [adapted from *Greuell and Konzelmann*, 1991] and (b) modeled snowpack liquid water content (percent). Observed liquid water content profiles were not available after JD 197 (July 16). The heavy line in (a) indicates the top of the snowpack.

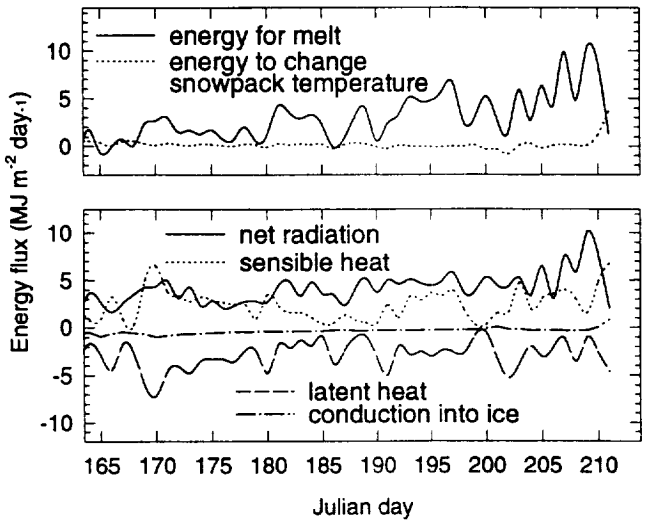

Figure 7. Time series of modeled energy fluxes at the surface of the snowpack.

englacial temperature profile by increasing the measured downward radiation fluxes by 0.5%, decreasing the reflected shortwave by a similar percentage and increasing the extinction coefficient for ice from 2.5 m^{-1} to 2.8 m^{-1}. These adjustment are, by their estimate, well within the respective uncertainties. As with SNTHERM, their simulated mass loss is delayed relative to the observed loss. They attribute this to their treatment of mass storage in the slush layer, which in their model is not allowed to drain until it has reached its capacity of 20 cm. Thus even though these models represent two extremes in their treatment of the drainage of meltwater from the snowpack, they both result in the retention of mass at the bottom of the snowpack.

Summary and Conclusions

SNTHERM, a one-dimensional energy and mass balance model developed at CRREL by *Jordan* [1992], was modified for use with snowpacks over ice. This model uses meteorological data and appropriate values for the surface properties to estimate the fluxes of shortwave and longwave radiation at the surface, sensible and latent heat transfers between the surface and the atmosphere, and the transfer of sensible heat into the snowpack. In addition, the profiles of temperature, density, grain size, thermal conductivity, specific heat, and liquid water content of the snowpack are estimated as the snowpack undergoes metamorphism over time.

Preliminary simulations were made using meteorological and snowpack data collected during the summer of 1990 at the Swiss camp near the equilibrium line on the west slope of the Greenland ice sheet [*Ohmura et. al.*, 1991]. Both the simulated height and mass of the snowpack agree well with the observations. Time-height profiles of temperature, density, and liquid water content conform to our expectations of the physical changes taking place in the snowpack during melt. Simulated snowpack temperatures show the nearly isothermal conditions characteristic of a melting snowpack, with the portion of the pack near the pack-ice interface remaining colder until the end of the simulated period. Small, diurnal variations in temperature are seen at the top of the snowpack in response to the diurnal fluctuations in net radiation, and sensible and latent heat fluxes. The rapid increase in density near the bottom of the snowpack is caused by meltwater from the upper levels of the snowpack freezing in the colder regions near the ice. The variation in liquid water content of the snowpack simulated by the model is essentially an inverse of the predicted bulk density since higher density layers in the snowpack have reduced pore space and, as a result, cannot hold as much liquid water as less dense layers.

Results from this type of simulation could be used to compute, for example, the onset and rate of snowmelt on the ice sheet. Since the emissivities of snow and liquid water are significantly different, especially in the microwave, these results may help to explain much of the temporal and spatial variation observed in passive microwave brightness temperatures over the ice sheet [*Mote et al.*, 1993; *Mote and Anderson*, 1994; *Mote and Rowe*, 1995].

Since exchanges of energy between the surface and the atmosphere determine the energy available to melt the snowpack, variations in surface properties, coupled with variations in cloud cover, atmospheric transmissivity and emissivity, and wind will contribute to spatial and temporal variations in the surface energy balance across the ice sheet and, therefore to variations in melt. We have begun to investigate which of the flux terms is responsible for most of the day-to-day variation in snowpack properties. Preliminary analysis of our simulation results shows that, as expected, net radiation provides the majority of the energy for ablation of the snowpack, with sensible heat supplying nearly all of the remainder. However, day-to-day variations in the amount of ablation seem to be highly correlated with the turbulent fluxes, implying that simple models of snowmelt based on correlations with air temperature may be able to capture much of the variance in snowmelt observed on the ice sheet. This result, when confirmed, will be important as we investigate the role of atmospheric circulation patterns on snowmelt over the ice sheet.

Acknowledgments. The authors would like to thank Mary R. Albert and Robert E. Davis, both of CRREL, and two anonymous reviewers for their helpful comments on earlier versions of this paper. This work was supported in part by NASA grant NAGW-1266 to the University of Nebraska-Lincoln.

References

Akan, A.O., Simulation of runoff from snow-covered hill slopes, *Water Resour. Res., 20*, 707-713, 1984.

Anderson, E. A., A point energy and mass balance model of a snow cover, *NOAA Tech. Rep. NWS 19*, Off. of Hydrol., Nat. Weather Serv., Silver Spring, Md., 1976.

Andreas, E. L., and B. Murphy, Bulk transfer coefficients for heat and momentum over leads and polynyas, *J. Phys. Oceanogr., 16*, 1875-1883, 1986.

Arya, S.P., *Introduction to Micrometeorology*, Academic, San Diego, Calif., 1988.

Bader, H.P., and P. Weilenmann, Modeling temperature distribution, energy and mass flow in a (phase-changing) snowpack, I, Model and case studies, *Cold Reg. Sci. Technol., 20*, 157-181, 1992.

Bohren, C., and B. Barkstrom, Theory of the optical properties of snow, *J. Geophys. Res., 79*, 4527-4535, 1974.

Braithwaite, R. J., On glacier energy balance, ablation, and air temperature, *J. Glaciol., 27*, 381-391, 1981.

Braithwaite, R. J., Greenland glaciers and the 'greenhouse effect,' *Rapp. Grønlands Geol. Unders., 148*, 51-53, 1990.

Braithwaite, R. J., and O. B. Olesen, Ice ablation in West Greenland in relation to air temperature and global radiation, *Z. Gletscherkd. Glazialgeol., 20*, 155-168, 1984.

Braithwaite, R. J., and O. B. Olesen, Increased ablation at the margin of the Greenland ice sheet under a greenhouse-effect climate, *J. Glaciol., 36*, 20-22, 1990a.

Braithwaite, R. J., and O. B. Olesen, Response of the energy balance on the margin if the Greenland ice sheet to temperature changes, *J. Glaciol., 36*, 217-221, 1990b.

Brooks, R. H., and A. T. Corey, Hydraulic properties of porous media, *Hydrology Papers, 3*, Colorado State Univ., Fort Collins, Colo., 1964.

Brun, E., E. Martin, V. Simon, C. Gendre, and C. Coleou, An energy and mass model of snow cover suitable for operational avalanche forecasting, *J. Glaciol., 35*, 333-342, 1989.

Colbeck, S. C., One-dimensional water flow through snow, *Research Report 296*, U. S. Army Corps of Eng., Cold Reg. Res. and Eng. Lab., Hanover, N. H., 1971.

Colbeck, S. C., Water flow through heterogeneous snow, *Cold Reg. Sci. Technol., 1*, 37-45, 1979.

Colbeck, S. C., and E.A. Anderson, The permeability of a melting snow cover, *Water Resour. Res., 18*, 904-908, 1982.

Gow, A. J., On the rates of grains and crystals in South Polar firn, *J. Glaciol., 8*, 241-252, 1969.

Greuell, W., Climatology, in *Energy and Mass Balance During the Melt Season at the Equilibrium Line Altitude, Paakitsoq, Greenland Ice Sheet: Progress Report 1*, edited by A. Ohmura, K. Steffen, H. Blatter, W. Greuell, M. Rotach, T. Konzelmann, M. Laternser, A. Ouchi, and D. Steiger, pp. 21-35, Dep. Geogr., Swiss Federal Inst. of Technol., Zurich, 1991a.

Greuell, W., Englacial temperature, in *Energy and Mass Balance During the Melt Season at the Equilibrium Line Altitude, Paakitsoq, Greenland Ice Sheet: Progress Report 1*, edited by A. Ohmura, K. Steffen, H. Blatter, W. Greuell, M. Rotach, T. Konzelmann, M. Laternser, A. Ouchi, and D. Steiger, pp. 76-82, Dep. Geogr, Swiss Federal Inst. of Technol., Zurich, 1991b.

Greuell, W., and T. Konzelmann, Mass budget, in *Energy and Mass Balance During the Melt Season at the Equilibrium Line Altitude, Paakitsoq, Greenland Ice Sheet: Progress Report 1*, edited by A. Ohmura, K. Steffen, H. Blatter, W. Greuell, M. Rotach, T. Konzelmann, M. Laternser, A. Ouchi, and D. Steiger, pp. 83-93, Dep. Geogr., Swiss Federal Inst. of Technol., Zurich, 1991.

Greuell, W., and T. Konzelmann, Numerical modelling of the energy balance and the englacial temperature of the Greenland Ice Sheet, Calculations for the ETH-Camp location (West Greenland, 1155 m a.s.l.), *Global Planet. Change, 9*, 91-114, 1994.

Greuell, W., and J. Oerlemans, Sensitivity studies with a mass balance model including temperature profile calculations inside the glacier, *Z. Gletscherkd. Glazialgeol., 22*, 101-124, 1986.

Guryanov, I. E., Thermal-physical characteristics of frozen, thawing and unfrozen grounds, in *Ground Freezing, Proceedings of the Fourth International Symposium on Ground Freezing*, edited by S. Kinosita and M. Fukuda, pp. 225-230, Hokkaido Univ. Press, Sapporo, Japan, 1985.

Hodges, D. B., G. J. Higgins, P. F. Hilton, R. E. Hood, R. Shapiro, C. N. Touart, and R. F. Wachtmann, Final tactical decision aid (FTDA) for infrared (8-12 μm) systems -- Technical background, *Sci. Rep. 5*, Syst. and Appl. Sci. Corp., Riverdale, Md., (under contract to Air Force Geophys. Lab., *Rep. AFGL-TR-83-0022*), 1983.

Huybrechts, P., A. Letreguilly, and N. Reeh, The Greenland ice sheet and greenhouse warming, *Palaeogeogr., Palaeoclim., Palaeoecol., 89*, 399-412, 1991.

Idso, S. B., A set of equations for full spectrum and 8-14 μm and 10.5-12.5 μm thermal radiation from cloudless skies, *Water Resour. Res., 17*, 295-304, 1981.

Illangasekare, T.H. and R.J. Walter Jr., M.F. Meier, and W.T. Pfeffer, Modeling of meltwater infiltration in subfreezing snow, *Water Resour. Res., 26*, 1001-1012, 1990.

Jordan, R., Meltwater movement in a deep snowpack, 2, Simulation model, *Water Resour. Res., 19*, 979-985, 1983.

Jordan, R., A one-dimensional temperature model for a snow cover: Technical documentation for SNTHERM.89, *Spec. Rep. 91-16*, U. S. Army Corps of Eng., Cold Reg. Res. and Eng. Lab., Hanover, N. H., 1991.

Jordan, R. Estimating turbulent transfer functions for use in energy balance models, *Internal Rep. 1107*, U. S. Army Corps of Eng., Cold Reg. Res. and Eng. Lab., Hanover, N. H., 1992.

Jordan, R., H. O'Brien, and M.R. Albert, Snow as a thermal background: Preliminary results from the 1987 field test, *Spec. Rep. 89-7*, U. S. Army Corps of Eng., Cold Reg. Research and Eng. Lab., Hanover, N. H., 1989.

Kattelman, R., Measurements of snow layer water retention, in *Proceedings of the Cold Regions Hydrology Symposium*, edited by D. L. Kane, pp. 377-386, American Water Resources Association, Bethesda, Md., 1986.

Konzelmann, T., Radiation measurements, in *Energy and Mass Balance During the Melt Season at the Equilibrium Line Altitude, Paakitsoq, Greenland Ice Sheet: Progress Report 1*, edited by A. Ohmura, K. Steffen, H. Blatter, W. Greuell, M. Rotach, T. Konzelmann, M. Laternser, A. Ouchi, and D. Steiger, pp. 51-59, Dep. Geogr., Swiss Federal Inst. of Technol., Zurich, 1991.

Large, W. G., and S. Pond, Sensible and latent heat flux measurements over the ocean, *J. Phys. Oceanogr., 12*, 464-482, 1982.

Loth, B., Snow cover model for global climate simulations, *J. Geophys. Res., 98*, 10,451-10,464, 1993.

Marsh, P., and M. K. Woo, Wetting front advance and freezing of meltwater within a snow cover, 1, Observations in the Canadian Arctic, *Water Resour. Res., 20*, 1853-1864, 1984.

Morris, E.M., Modeling of water flow through snowpacks, in *Seasonal Snow Covers: Physics, Chemistry, Hydrology*, edited by H.G. Jones and W.J. Orville-Thomas, pp. 179-208, D. Reidel, Dordrecht, 1987.

Mote, T.L., and M.R. Anderson, Variations in snowpack melt on the Greenland ice sheet based on passive-microwave measurements, *J. Glaciol. 41*, 51-60, 1995.

Mote, T.L., and C. M. Rowe, A comparison of microwave radiometric data and modeled snowpack conditions for Dye 2, Greenland, *Meteorology and Atmospheric Physics*, in press, 1995.

Mote, T.L., M.R. Anderson, K.C. Kuivinen, and C.M. Rowe, Passive microwave-derived spatial and temporal variations of summer melt on the Greenland ice sheet, *Ann. Glaciol., 17*, 233-238, 1993.

Ohmura, A., K. Steffen, H. Blatter, W. Greuell, M. Rotach, T. Konzelmann, M. Laternser, A. Ouchi, and D. Steiger, *Energy and Mass Balance During the Melt Season at the Equilibrium Line Altitude, Paakitsoq, Greenland Ice Sheet: Progress Report 1*, Dep. of Geogr., Swiss Federal Inst. of Technol., Zurich, 1991.

Ohmura, A., P. Kasser, and M. Funk, Climate at the equilibrium line of glaciers, *J. Glaciol., 38*, 397-411, 1992.

Patankar, S. V., *Numerical Heat Transfer and Fluid Flow*, Hemisphere, New York, 1980.

Paterson, W.S.B., Ice sheets and ice shelves, in *Dynamics of Snow and Ice Masses*, edited by S.C. Colbeck, pp. 1-78, Academic, New York, 1980.

Reeh, N., Parameterization of melt rate and surface temperature on the Greenland ice sheet, *Polarforschung, 59*, 113-128, 1991.

Richards, L.A., Capillary conduction of liquids through porous mediums, *Physics, 1*, 318-333, 1931.

Shapiro, R., Solar radiative flux calculations from standard meteorological observations, *Scientific Rep. 1*, Syst. and Appl. Sci. Corp., Riverdale, Md., (under contract to Air Force Geophys. Lab., *Rep. AFGL-TR-82-0039*), 1982.

Shapiro, R., A simple model for the calculation of direct and diffuse solar radiation through the atmosphere, *Scientific Rep. 35*, ST Syst. Corp., Lexington, Mass., (under contract to Air Force Geophys. Lab., *Rep. AFGL-TR-87-0200*), 1987.

Shimizu, H., Air permeability of deposited snow, *Contribution 1053* (English Translation), Inst. of Low Temperat. Sci., Sapporo, Japan, 1970.

Stephenson, P. J., Some considerations of snow metamorphism in the Arctic ice sheet in the light of ice crystal studies, *Physics of Ice and Snow, Proceedings of an International Conference on Low Temperature Science*, Inst. of Low Temperat. Sci., Hokkaido Univ., Sapporo, Japan, pp. 725-740, 1967.

Van der Veen, C. J., Ice sheets and the CO_2 problem, *Surv. in Geophys., 9*, 1-42, 1987.

Warrick, R., and J. Oerlemans, Sea level rise, in *Climate Change: The IPCC Scientific Assessment*, edited by J.T. Houghton, G. J. Jenkins, and J. J. Ephraums, pp. 257-281, Cambridge University Press, Cambridge, 1990.

R. Jordan, Geophysical Sciences Branch, U.S. Army Cold Regions Research and Engineering Laboratory, Hanover, NH 03755-1290. rjordan@hanover-crrel.army.mil.

K.C. Kuivinen. Snow and Ice Research Group, University of Nebraska-Lincoln, Lincoln, NE 68588-0135. kuivinen@unlinfo.unl.edu

C.M. Rowe, Meteorology/Climatology Program, Department of Geography, University of Nebraska-Lincoln, Lincoln, NE 68588-0135. crowe@unlinfo.unl.edu.

(Received September 7, 1994; revised April 5, 1995; accepted April 19, 1995.)

Annals of Glaciology 21 1995
© International Glaciological Society

Indications of melt in near-surface ice-core stratigraphy: comparisons with passive-microwave melt signals over the Greenland ice sheet

CLINTON M. ROWE, MARK R. ANDERSON,
Department of Geography and Snow and Ice Research Group, University of Nebraska–Lincoln, Lincoln, NE 68588, U.S.A.

THOMAS L. MOTE,
Department of Geography, University of Georgia, Athens, GA 30602, U.S.A.

KARL C. KUIVINEN
Department of Geography and Snow and Ice Research Group, University of Nebraska–Lincoln, Lincoln, NE 68588, U.S.A.

ABSTRACT. During the summer of 1993, a field program was conducted to collect several shallow firn cores from two locations in the southern region of the Greenland ice sheet. Stratigraphic evidence of melt from these cores was used for comparison with satellite-derived indications of melt.

The shallow firn cores were examined for stratigraphic evidence of past melt events and were sampled for oxygen-isotope analysis to delineate the annual accumulation layers in the snowpack. The relative intensity of each year's summer melt episode was compared to the corresponding melt frequency derived from microwave emissions. This comparison demonstrates that a linkage between the stratigraphic record and microwave data can be established. Both data sets indicate that there was less melt during the late 1970s and early 1980s than during the late 1980s, in general agreement with climate observations.

INTRODUCTION

High-latitude regions are expected to be more sensitive to climatic change than are regions at middle and low latitudes, due to an enhanced greenhouse effect. Thus, much effort has been directed toward detecting climate changes in polar regions. Because of the paucity of climate stations in polar regions, proxy data are often utilized. Ice cores preserve a record of past climates in a variety of their physical characteristics, including stratigraphy, stable-isotope concentrations, microparticles and conductivity.

Passive-microwave remote sensing offers a means of detecting changes in the snow cover over large geographic areas. At microwave frequencies, the emissivity of dry snow increases dramatically with the addition of small amounts of liquid water, so that passive-microwave remote sensing can detect the onset, duration and cessation of snow melt. Because these data have been collected for only a relatively short period, their use in detecting climatic change is limited. However, satellite passive-microwave data do provide a means to monitor current and future melt conditions on the Greenland ice sheet.

DATA AND METHODS

Shallow firn cores

Shallow firn cores were obtained at two sites, Dye 2 (66°29′ N, 46°17′ W, 2117 m a.s.l.) and South Cluster (65°18′ N, 45°50′ W, 2442 m a.s.l.), in southern Greenland (Fig. 1), using a lightweight, hand-powered auger. These cores were inspected and the position, thickness and character of all stratigraphic features (e.g. ice layers, ice wedges) were recorded. Each core was then divided every 5 cm along the length of the core into samples for density measurement and subsequent oxygen-isotope analysis.

Oxygen-isotope values are most often presented as standardized ratios ($\delta^{18}O$) of deviations of the proportion of ^{18}O from that of standard mean ocean water (SMOW) defined as

$$\delta^{18}O = \frac{(^{18}O/^{16}O)_{sample} - (^{18}O/^{16}O)_{SMOW}}{(^{18}O/^{16}O)_{SMOW}} \times 1000. \quad (‰)$$

A more negative value of $\delta^{18}O$ indicates that the precipitation in the sample was formed at lower

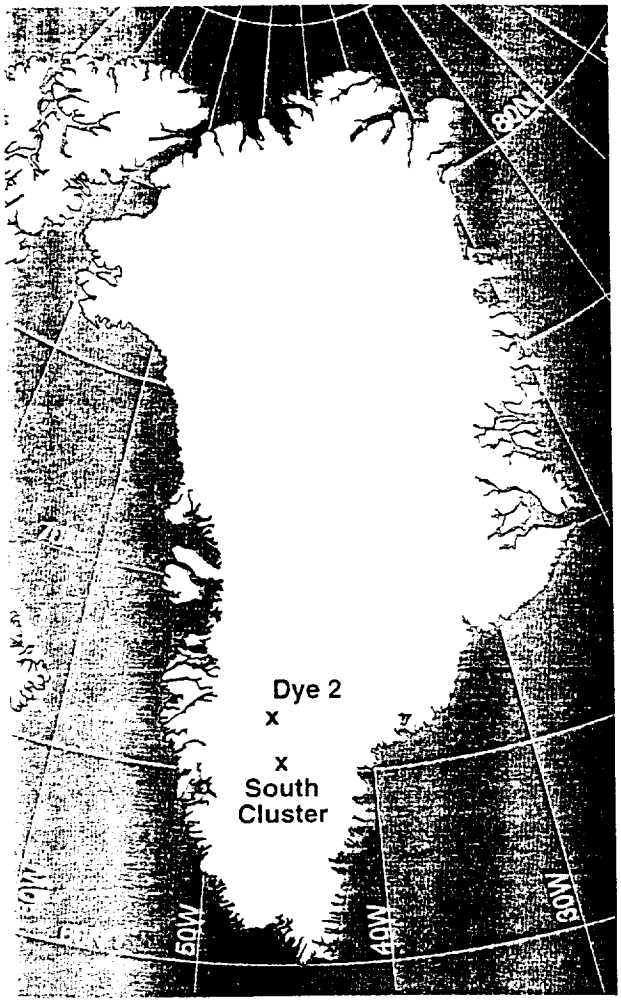

Fig. 1. Location map of the two sites where shallow firn cores were obtained.

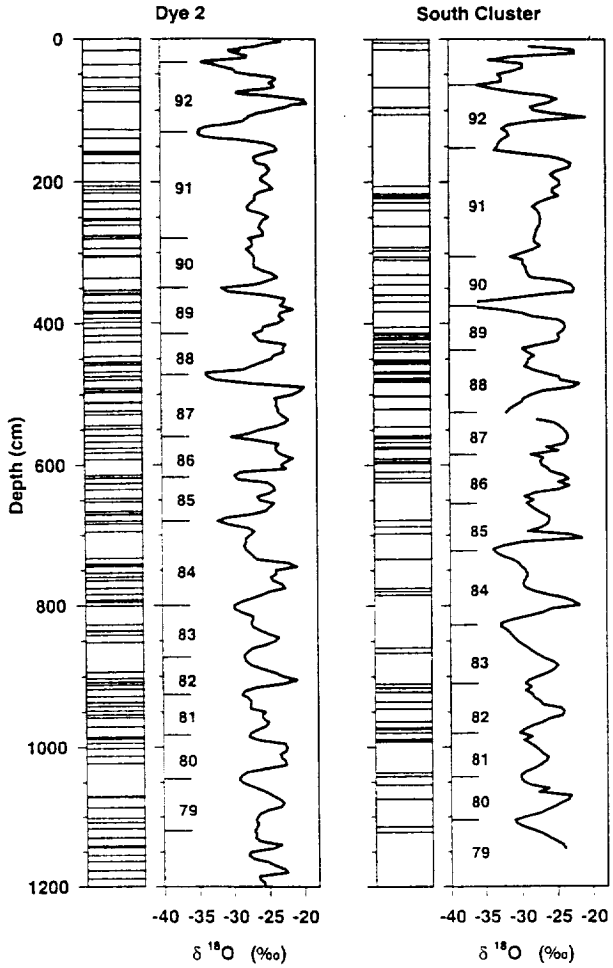

Fig. 2. Ice-feature stratigraphy and oxygen-isotope ratios for the firn cores from the Dye 2 and South Cluster sites. The horizontal bars mark the position and approximate thickness of all ice features observed in the core. Annual layering as derived from the oxygen-isotope ratios is indicated on the ^{18}O plot by the last two digits of the year.

temperature (Dansgaard and others, 1973). Thus, $\delta^{18}O$ can be used as a surrogate for air temperature.

As the coldest temperatures are to be expected during the winter, when no melt takes place, minima in the $\delta^{18}O$ vs depth curve were used to delineate melt seasons in this study. Each core was then analyzed to give the thickness of each year's accumulation (Fig. 2).

Passive-microwave data

Determination of snowpack melt was made using data from two satellite microwave radiometers, the Scanning Multichannel Microwave Radiometer (SMMR) and the Special Sensor Microwave/Imager (SSM/I). These data were obtained from the U.S. National Snow and Ice Data Center (NSIDC) archive of daily brightness temperatures binned into a 25 km × 25 km grid on a polar stereographic projection. The SMMR data are available on alternate days from October 1978 to August 1987 and the SSM/I data are available daily beginning in July 1987. Determination of which grid cells were undergoing surface melt was made using data from the 37 GHz horizontal polarization channel of both sensors (Mote, 1994). Differences in view angle, radiometric resolution, calibration, and time and frequency of observations lead to a systematic difference between the SMMR and SSM/I sensors, primarily due to the difference in calibration of the two sensors (Jezek and others, 1991). A linear regression of the brightness temperatures over the dry-snow region of the ice sheet for the period during which both sensors were operating (10 July–20 August 1987) allows the systematic difference between sensors to be removed (Mote, 1994). All SMMR brightness temperatures used in this study were converted to equivalent SSM/I brightness temperatures based on this regression.

At frequencies greater than 10 GHz, the brightness temperature (T_B) of snow increases monotonically with increasing volumetric liquid-water content (m_v), for m_v less than 6% (Stiles and Ulaby, 1980). The T_B is also dependent on the thermometric temperature of the snow, but the increase in T_B due to even a small addition of liquid water is much greater than could occur from an increase in thermometric temperature. Thus, a unique T_B threshold value can be selected for a given m_v indicative of the onset of melting (Mote, 1994).

A simple microwave-emission model was used to estimate the 37 GHz, horizontally polarized T_B associated with 1% liquid water content in the

snowpack. The 1% value was chosen because the T_B of the snowpack typically shows the greatest increase as m_v increases from 0.5% to 1% (Stiles and Ulaby, 1980). A semi-empirical approach was used in which the scattering properties of the snowpack were estimated from the brightness temperatures observed before the onset of melt (Mote and Anderson, in press). The dielectric constant of the ice–air–water mixture under melt conditions was calculated through the use of a dielectric mixing model described by Tiuri and Schultz (1980). The change in the bulk dielectric as liquid water forms in the snowpack results in an increased emissivity and, therefore, a higher brightness temperature. A simplified version of the radiative-transfer equation shown by Ulaby and Stiles (1980) was then used to estimate a brightness temperature associated with melt for each grid cell on the ice sheet.

A threshold approach (Mote, 1994) was used to identify the occurrence of melt in each grid cell over the ice sheet for each day of available data. On a given day, if the observed 37 GHz, horizontally polarized T_B from a grid cell exceeded the modeled threshold value, that location is considered to have experienced melt. Time series of melt occurrence were extracted for the grid cells containing the Dye 2 and South Cluster sites for further analysis.

DISCUSSION

Visual inspection of the number and location of melt features identified in the cores as a function of depth (Fig. 2) reveals that, prior to 1991, melt features are more common in the upper (more recent) parts of the cores than in the lower (less recent) parts. This is especially true for the South Cluster core. For example, 1983 and 1984 show very few melt indications compared to 1988 and 1989, when numerous melt features were observed in the core. Not only are there more ice features, but the thickness of the layers is also greater. The apparent increase in the frequency of melt features begins in 1985 at Dye 2 and 1986 at South Cluster. This corresponds well to the increase in mean melt extent on the southwest part of the ice sheet since 1986 identified by Mote and Anderson (in press).

A more direct, quantitative comparison of the microwave melt frequency and the melt features in the cores is difficult to make. Perhaps ideally, the number of melt features observed in an annual layer of the core would correspond to the total number of melt events identified with the microwave data, where a melt event is defined as one or more consecutive days for which the brightness temperature exceeded the melt threshold (Table 1). However, melt events cannot be determined unambiguously from the SMMR record as observations were made only on alternate days. As a result, two consecutive observations of melt in the SMMR data could correspond to a single 3–5 d melt event or to two 1–2 d events separated by an unobserved day with no melt. Furthermore, because of the complex flow regime of meltwater as it percolates into the snowpack, there is not necessarily a one-to-one relationship between melt events and the number of melt features. For example, a single melt event, especially one producing a relatively large amount of meltwater, could result in multiple ice layers as liquid water spreads out along horizontal strata in the snow. Conversely, successive melt events may not produce separate ice features in the snowpack, as

Table 1. Microwave-derived melt events and frequencies and number of ice features in each annual layer for the Dye 2 and South Cluster sites

	Dye 2			*South Cluster*		
Year	*Melt events**	*Melt frequency %*	*Ice features*	*Melt events**	*Melt frequency %*	*Ice features*
1991	11	19.7	3	4	8.6	5
1990	7	10.2	3	5	5.9	5
1989	3	11.5	4	3	7.0	6
1988	5	21.7	5	4	5.2	11
1987	–	15.1	8	–	6.9	6
1986	–	12.9	4	–	8.1	6
1985	–	9.8	2	–	6.6	2
1984	–	7.1	9	–	5.4	3
1983	–	6.5	2	–	4.8	2
1982	–	5.4	2	–	1.8	4
1981	–	9.7	3	–	8.1	4
1980	–	0.0	2	–	1.6	2
1979	–	6.5	1	–	4.8	2

* The number of melt events cannot be computed for that part of the time series containing SMMR data (see text for explanation).

meltwater from a subsequent event may simply refreeze to the previous ice layer. Therefore, it is necessary to standardize the microwave-derived melt occurrences and snowpack-melt features on a seasonal basis for comparison.

As a first attempt at this, the total thickness of all ice features in each annual layer in the core was computed and compared to the annual microwave-derived frequency of melt for the grid cell containing each site (Fig. 3). For this comparison, the melt frequency is expressed as the percentage of days between 1 May and 31 August of a given year for which melt conditions were identified in that cell. A percentage of days is used rather than the raw frequency to account for the difference in the number of days with available data for each year. Half of the maximum thickness was used for ice features that did not occupy the entire core diameter (e.g. lenses). This technique makes the assumption that liquid water produced during a melt season does not penetrate very far into the snowpack before refreezing and, thus, contributes to the ice volume only for the

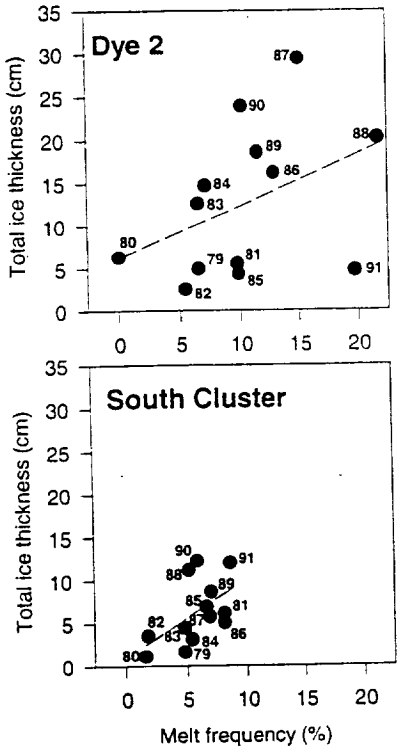

Fig. 3. Total ice-feature thickness in each annual accumulation layer versus the microwave-derived melt frequency for that year for the Dye 2 and South Cluster sites. Each data pair is identified by the last two digits of the year it represents.

year during which the melt took place. During the 1993 field season at Dye 2, meltwater penetrated only about 20 cm before refreezing into a nearly continuous ice layer.

For Dye 2, there seems to be a clear relationship between total ice-feature thickness in the annual layer and melt frequency, with two identifiable clusters of data: a low-frequency/low-ice cluster and a high-frequency/high-ice cluster. Upon closer inspection, these two clusters are distinct temporally, with the low/low cluster comprising the years 1979–85 and the high/high cluster comprising 1986–90. At South Cluster, the relationship between these variables is not as strong and there is no clear separation of years into groups. The low incidence of melt at this site, and on the South Dome generally (Mote, 1994), likely results in a low signal/noise ratio for the microwave-derived melt-frequency time series. This may be the reason for the less distinct separation of clusters in the data for this site. Melt-frequency values for locations at higher elevation, where melt is relatively rare, must be used with caution. However, the slope of the regression line, although not significant due to the small number of data values, is about the same for the two sites, lending some credibility to the relationship.

The last year with microwave data available, 1991, is an outlier at Dye 2, with a high frequency of melt but a low ice volume. Further inspection of the $\delta^{18}O$-derived annual layers reveals that, for both cores, the 1991 layer is approximately twice as thick as the other annual layers. A possible explanation for this is an increased number of summer storms bringing additional snowfall and reducing the time for thick ice features to develop during any one melt event. However, it must be remembered that the microwave signal yields the frequency of melt events, not the intensity of melt, and that more frequent melt does not always lead to greater total melt.

SUMMARY AND CONCLUSIONS

Shallow firn cores were obtained from the Dye 2 and South Cluster sites on the Greenland ice sheet during summer 1993. Oxygen-isotope analysis was performed to delineate annual accumulation layers. Within each annual layer, the total thickness of ice layers was obtained from the core stratigraphy as an indication of the relative amount of snow melt for that year. Using the 37 GHz data from two satellite microwave radiometers, the occurrence of snow melt was identified using a threshold technique based on the increased emissivity caused by the formation of liquid water in the snowpack. Seasonal melt frequencies were determined for the two locations for each year from 1979 to 1991. Comparisons were then made between the two melt proxy-data sets.

Both the microwave-derived melt frequencies and the ice thicknesses obtained from the shallow firn cores show that the late 1970s and early 1980s had less melt than the late 1980s. Thus, the microwave-derived melt frequencies appear to represent a viable method of monitoring snowpack melt on the Greenland ice sheet. Continued monitoring of snow melt combined with measurements of accumulation and runoff will provide the data necessary for a better understanding of the mass balance of the ice sheet.

ACKNOWLEDGEMENTS

This research was funded by National Aeronautics and Space Administration grant NAGW-1266 and training grant NGT-30127. The authors thank R. H. Thomas of

NASA and K. C. Jezek of Ohio State University for their assistance in obtaining the South Cluster core, and H. B. Clausen of the University of Copenhagen for the oxygen-isotope analysis.

REFERENCES

Dansgaard, W., S. J. Johnsen, H. B. Clausen and N. Gundestrup. 1973. Stable isotope glaciology. *Medd. Grønl.*, **197**(2).

Jezek, K. C. *and 6 others*. 1991. Comparison between SSMR and SSM/I passive microwave data collected over the Antarctic ice sheet. *Byrd Polar Research Center. Technical Report* 91-03.

Mote, T. L. 1994. Variations in passive microwave measurements of melt on the Greenland ice sheet and associated Northern Hemisphere atmospheric circulation. (Ph.D. dissertation. University of Nebraska–Lincoln.)

Mote, T. L. and M. R. Anderson. 1995. Variations in snowpack melt on the Greenland ice sheet based on passive-microwave measurements. *J. Glaciol.*, **41**(137), 51–60

Stiles, W. H. and F. T. Ulaby. 1980. The active and passive microwave response to snow parameters. 1. Wetness. *J. Geophys. Res.*, **85**(C2), 1037–1044.

Tiuri, M. and H. Schultz. 1980. Theoretical and experimental studies of microwave radiation from a natural snowfield. *In* Rango, A., *ed. Microwave Remote Sensing of Snowpack Properties. Proceedings of a Workshop ... Fort Collins, Colorado ... 1980.* Washington, DC, National Aeronautic and Space Administration, 225–234. (Conference Publication 2153.)

Ulaby, F.T. and W.H. Stiles. 1980. The active and passive microwave response to snow parameters. 2. Water equivalent of dry snow. *J. Geophys. Res.*, **85**(C2), 1045–1049.

Variations in snowpack melt on the Greenland ice sheet based on passive-microwave measurements

THOMAS L. MOTE
Department of Geography, University of Georgia, Athens, GA 30602-2502, U.S.A.

MARK R. ANDERSON
Program in Meteorology/Climatology, Department of Geography, University of Nebraska–Lincoln, Lincoln, NE 68588-0135, U.S.A.

ABSTRACT. A simple microwave emission model is used to simulate 37 GHz brightness temperatures associated with snowpack-melt conditions for locations across the Greenland ice sheet. The simulated values are utilized as threshold values and compared to daily, gridded SMMR and SSM/I passive-microwave data, in order to reveal regions experiencing melt. The spatial extent of the area classified as melting is examined on a daily, monthly and seasonal (May–August) basis for 1979–91. The typical seasonal cycle of melt coverage shows melt beginning in late April, a rapid increase in the melting area from mid-May to mid-July, a rapid decrease in melt extent from late July through mid-August, and cessation of melt in late September. Seasonal averages of the daily melt extents demonstrate an apparent increase in melt coverage over the 13 year period of approximately 3.8% annually (significant at the 95% confidence interval). This increase is dominated by statistically significant positive trends in melt coverage during July and August in the west and southwest of the ice sheet. We find that a linear correlation between microwave-derived melt extent and a surface measure of ablation rate is significant in June and July but not August, so caution must be exercised in using the microwave-derived melt extents in August. Nevertheless, knowledge of the variability of snowpack melt on the Greenland ice sheet as derived from microwave data should prove useful in detecting climate change in the Arctic and examining the impact of climate change on the ice sheet.

Submitted July 1993 and in revised form December 1993

INTRODUCTION

Scientific interest in the magnitude of melting on the Greenland and Antarctic ice sheets has grown along with concern about the potential effects of climate change. In particular, increased melting in a warmer climate may lead to rising sea levels (Bindschadler, 1985; Peltier and Tushingham, 1989). However, Zwally (1989) found that the ablation and accumulation zones of the Greenland ice sheet thickened between 1978 and 1985, as determined from radar altimetry data, and suggested the change might be a product of increased accumulation associated with a warmer climate. This reasoning also suggests that increased melting should be associated with, but more than offset by, the increased accumulation. In contrast, Braithwaite and others (1992) used stake observations at three locations near the margin of the ice sheet to argue that thickening in the ablation zone was due to decreased ablation, primarily from decreased melting.

The question of how the ice sheet responds to variations in climate, and potential climate change, can be addressed at least partially by examining the variations in snowpack melt. Unfortunately, identification of snowpack melt events on the Greenland ice sheet is accomplished only at a few isolated stations or by interpretation of shallow-ice-core records that are widely scattered. Satellite remote sensing offers a means of acquiring a ~~detailed record, both spatial and temporal,~~ of snowpack-melt occurrences. Passive-microwave remote sensing is especially suited to measuring melt occurrences due to the rapid change in microwave emission of a snowpack in response to the introduction of even a small amount of liquid water. Microwave emission, as described by a blackbody-equivalent radiometric temperature called a brightness temperature (T_B), exhibits a distinct increase at frequencies greater than 10 GHz during snowpack melt in the West Greenland percolation zone (Thomas and others, 1985). This increase in T_B stands in sharp contrast to the lower T_B observed during non-melt conditions (Gloersen and others, 1974) due to internal scattering within the snowpack (Zwally, 1977). The emissivity of snow changes rapidly with melt due to an increase in the liquid-water content of the snow. Because of the high dielectric constant of liquid water, compared to that of air and ice, melt strongly affects the dielectric constant of the ice–air–water mixture (Ulaby and others, 1986). The increase in the dielectric constant raises the absorptivity and, according to Kirchoff's law, the emissivity. The result is an increase in absorption relative to volume scattering, which reduces the scattering albedo and enhances emission (Chang and others, 1976, 1985; Foster and others, 1984).

This change in T_B with melt is frequency-dependent. Below approximately 10 GHz, a spectral region where volume scattering is small compared to surface scattering, the T_B decreases with increasing liquid-water content; near 10 GHz, the T_B is nearly insensitive to liquid-water content (Ulaby and others, 1986). The T_B becomes

increasingly sensitive to water content at higher frequencies. The frequency dependence of the T_B on liquid-water content has been used to identify the onset of melt in the seasonal snowpack. Kunzi and others (1982) found the 37 GHz T_B to be lower than the 18 GHz T_B of dry snow, but the two values are nearly equal for wet snow. Other investigators have relied on the increase in brightness temperatures at high frequencies (37 GHz) to identify melt and quantify the liquid-water content of the snowpack (e.g. Stiles and Ulaby, 1980).

Although snow density, temperature, crystal structure and crystal size all contribute to the snowpack's emissivity, changes in the liquid-water content produce the most prominent changes in T_B. For example, snow with 2% liquid-water content may produce a 37 GHz T_B more than 100 deg higher than dry snow (Hofer and Matzler, 1980). The increase in T_B with melt has been used to map regions of the Greenland ice sheet experiencing melt during a period of intense warming in 1989 (Mote and others, 1993). As a continuation of that research, we use the increase in T_B at 37 GHz to quantify the extent and frequency of melt on the Greenland ice sheet during the period 1979–91.

100K

SATELLITE MICROWAVE DATA

Measurements of snowpack melt were made using data obtained from two satellite microwave radiometers, the Nimbus-7 Scanning Multichannel Microwave Radiometer (SMMR) and the Defense Meteorological Satellite Program (DMSP) Special Sensor Microwave/Imager (SSM/I). The SMMR recorded radiation every other day in ten channels (Gloersen and Hardis, 1978), including both polarizations for 6.6, 10.7, 18.0, 21.0 and 37.0 GHz, from October 1978 to August 1987. The SSM/I, which began operation in July 1987, records radiation daily in seven channels, the vertical polarization for 22.2 GHz and both polarizations for 19.35, 37.0 and 85.5 GHz (Hollinger and others, 1987). The 37 GHz, horizontally polarized (37H) channel was used for this research due to the great sensitivity of that channel to changes in snowpack liquid-water content. Additionally, the 37H channel had the smallest relative calibration difference between the two sensors, which facilitates merging the two data sets (Jezek and others, 1991).

Please plot this on one line

The two sensors differ in view angle (50.3° for SMMR vS 53.1° for SSM/I), radiometric resolution and calibration. Due to a change in swath width (approximately 1400 km for SSM/I vS 700 km for SMMR), the number of daily overpasses of a given location is greater for the SSM/I than for the SMMR. A systematic difference in SMMR and SSM/I brightness temperatures is primarily due to the difference in calibration of the two sensors (Jezek and others, 1991). A linear regression of the brightness temperatures was used to remove this systematic difference. The regression was performed using daily, gridded SSM/I and SMMR brightness

? versus

? versus

temperatures for locations north of 70° N and at elevations greater than 2700 m a.s.l. This region, which approximates the dry-snow zone of the ice sheet, was selected to avoid the influence of melt on the regression. Data for 20 d between 11 July and 20 August 1987, the period when both sensors were operating concurrently, were included in the regression. The resulting equation for the 37H channel ($r^2 = 0.97$) is:

$$T_{B,SSMI} = 1.084 T_{B,SMMR} - 10.81 \quad (1)$$

where $T_{B,SMMR}$ is the SMMR brightness temperature (K) and $T_{B,SSMI}$ is the SSM/I brightness temperature (K). All SMMR brightness temperatures were converted to equivalent SSM/I brightness temperatures using this regression equation.

The SMMR and SSM/I data were obtained from the National Snow and Ice Data Center (NSIDC) archive of brightness-temperature grids. The orbital data were interpolated onto a 25 km × 25 km grid on a polar stereographic projection. Any data sample located within a given grid cell on a given day, beginning at 0 UTC, was averaged into the daily value for that grid cell (NSIDC, 1992). Grid cells with missing data were filled by spatially averaging the grid cells immediately adjacent. Seven days that are included in the NSIDC archive were eliminated from the analysis because of missing swaths of data.

AUTHOR: what is UTC ?

"Universal Time Coordinated", the same as GMT

A land mask was digitized from the Quaternary map of Greenland published by The Geological Survey of Greenland. This mask was used in conjunction with both the SMMR and SSM/I water and coastline masks to eliminate any grid cells not covered by at least 50% ice or with any permanently standing water. The unmasked grid cells available for analysis covered a total area of ~~1 648 000~~ 1 648 125 km², including parts of ice caps separate from the ice sheet. The ice sheet covers approximately 1 701 000 km² and ice caps cover another 65 000 km² (Weidick, 1985). Between 7 and 12% of the ice sheet and ice caps is removed from the analysis by the masking process.

MICROWAVE EMISSION OF MELTING SNOW

A simple microwave emission model was employed to determine the 37H T_B associated with snow cover containing a given volumetric water content (m_v) for each grid cell on the Greenland ice sheet. Because T_B increases with increasing m_v, a simulated T_B can be used as a threshold value to identify the occurrence of snowpack melt with microwave data. Given the lack of data on snow grain-size and density necessary for calculation of scattering coefficients, a semi-empirical approach was taken in which the emission model was first inverted under non-melt conditions to derive scattering coefficients. Ulaby and Stiles (1980) give the brightness temperature (T_{Bi}) produced by the ith snow layer of thickness d_i as:

$$T_{ai} = T_i \int_0^{d_i} \rho_i \kappa'_{ai} \sec\theta_i' \exp[-(\kappa'_{ai} + \kappa'_{si})\rho_i(d_i - h)\sec\theta_i']dh \quad (2)$$

where T_i is the thermometric temperature of layer i (K), κ'_{ai} is the mass absorption coefficient ($kg^{-1}m^3$), κ'_{si} is the mass scattering coefficient ($kg^{-1}m^3$), θ'_i is the propagation angle, h is the depth in the ith layer (m), and ρ_i is the density ($kg\,m^{-3}$). The integral can be solved analytically and expanded for multiple snow layers, ignoring diffuse scatter and multiple reflections at boundary layers, to determine the brightness temperature at the surface of the snowpack (T'_B) (Abdelrazik and others, 1981). The T_B detected by the satellite sensor is the sum of T'_B, upwelling sky radiation, reflected downwelling sky radiation, and the reflected emission from free space, and is found by:

$$T_B = T'_B e^{-\tau\sec\theta} + T_{sky} + (1-\epsilon)T_{sky}e^{-\tau\sec\theta} + (1-\epsilon)T_{sp}e^{-2\tau\sec\theta} \quad (3)$$

where T_{sky} is the sky brightness temperature at 37 GHz (25 K), T_{sp} is the averaged brightness temperature of free space (3 K), τ is the atmospheric loss factor at 37 GHz (0.05), θ is the sensor view angle, and ϵ is the bulk emissivity of the snowpack.

The increase in microwave emission of snow undergoing melt is associated with an increase in the absorption coefficient. Therefore, the absorption coefficient must be calculated under spring pre-melt and summer-melt conditions. The absorption coefficient can be found by:

$$\kappa_a = 4\pi/\lambda\left[k'_s/2\left(\left[1 + (k''_s/k'_s)^2\right]^{0.5}\right) - 1\right]^{0.5} \quad (4)$$

where κ_a is the absorption coefficient (m^{-1}), λ is the wavelength (m), k'_s is the real part of dielectric constant of snow, and k''_s is the imaginary part of dielectric constant.

The complex dielectric constant can be found by:

$$k_s = 3[a(r_w/r_a)^3(k_w - 1) - b(r_i/r_a)^3(2k_w + 1)] / [a(2 + k_w) - 2b(r_i/r_w)^3(k_w - 1) - a(r_w/r_a)^3(k_w - 1) + b(r_i/r_a)^3 (2k_w + 1)] + 1 \quad (5)$$

$$a = 2k_w + k_i \quad (6)$$

$$b = k_w - k_i \quad (7)$$

$$r_w = r_i\left[1 + \frac{0.92 m_v/\rho_s}{1 - (m_v/\rho_s)}\right]^{\frac{1}{3}} \quad (8)$$

$$r_a = r_i\left[\frac{0.92}{\rho_s}\right]^{\frac{1}{3}}\left[1 + \frac{m_v/\rho_s}{1 - m_v/\rho_s}\right]^{\frac{1}{3}} \quad (9)$$

where k_s is the complex dielectric constant of snow, k_w is the complex dielectric constant of water, k_i is the complex dielectric constant of ice, r_i is the radius of ice particles (m), r_a is the radius of air pockets (m), r_w is the radius of

water-covered ice particle (m), m_v is the volumetric water content, and ρ_s is the density of snow (kg m^{-3}). Smooth boundaries between snow layers and at the snow-air boundary were assumed, and the transmission coefficients at each boundary were calculated by:

$$\tau_s = 1 - \left[\frac{\left(\cos\theta_t - \sqrt{\epsilon_b/\epsilon_t - \sin^2\theta_t}\right)}{\left(\cos\theta_t + \sqrt{\epsilon_b/\epsilon_t - \sin^2\theta_t}\right)}\right]^2 \qquad (10)$$

where τ_s is the power transmission coefficient, ϵ_b is the relative dielectric of underlying layer, ϵ_t is the relative dielectric of overlying layer, and θ_t is the propagation angle.

The model was first inverted under spring conditions to calculate scattering coefficients for each year. Scattering coefficients were estimated for individual years to account for differences in the amount of winter accumulation, which may affect the scattering properties of the snow. Observed brightness temperatures were averaged for a period before the onset of summer melt and used in the model to calculate scattering coefficients. The observed brightness temperatures were averaged for a period in each year when the temperature profile is assumed to have been nearly isothermal, and just prior to the onset of melt. This allows estimated 10 m temperatures to be used to approximate the temperature throughout the snowpack. Based on these criteria, the first 15 d of April were selected as the most appropriate period for using the observed brightness temperatures to estimate scattering coefficients.

The 10 m snowpack temperature for each grid cell was estimated from a third-order regression equation based on latitude, longitude and elevation (Budd and others, 1982). Elevation data are from the radar altimeter aboard ERS-1 (S. Ekholm, personal communication, 1993) and from the Seasat radar altimeter (Bindschadler and others, 1989).

Absorption coefficients were based on a snowpack density of 480 kg m^{-3}, typical conditions for the top meter of moderately packed snow (Zwally, 1977), and a mean grain-size of 0.5 mm, which is appropriate for fine-grained snow (Stephenson, 1967). Changing the grain-size does not strongly affect the simulated brightness temperatures. The spatial variation in grain-size should be accounted for by the empirically derived scattering coefficients.

Using the empirically derived scattering coefficients, summer-melt conditions were simulated by the addition of 1% liquid water to the top 1 m of the snowpack. The 1% value was chosen because it is near the lower limit of the radiometer's sensitivity to changes in water content (Stiles and Ulaby, 1980). The thermometric temperature of the top 1 m was assumed to be 273 K. The model does not account for changes in the scattering coefficient due to grain growth associated with the freeze–thaw metamorphism of melt. Estimated rates of grain growth were initially incorporated into the model, and a linear increase in the scattering coefficient with grain growth

was assumed, as suggested by Rotman and others (1982), but these changes had little effect on the simulated melt T_B. Because of the limited knowledge of grain-size distributions on the ice sheet, the results presented here do not include a correction to the scattering coefficient for grain growth.

A mean map of simulated-melt brightness temperatures for the 13 years (Fig. 1) generally resembles that of the mean emissivity map for April (Fig. 2). The emissivity map was produced from observed April brightness temperatures and 10 m snowpack temperatures using the Rayleigh–Jeans approximation, which states:

Figs 1 & 2

$$\epsilon = \frac{T_B}{T} \qquad (11)$$

where ϵ is the emissivity, and T is the thermometric temperature. The relationships between the simulated-melt T_B and both the observed April T_B and April emissivity are not linear. The relatively warm underlying snowpack in the southwest results in simulated-melt T_B higher than would be expected from a simple linear relationship with the April emissivity. Conversely, the cold underlying snowpack in the far north results in simulated-melt T_B lower than would be expected based on the April emissivity. Additionally, the high spring emissivities in the southeast, in some cases near 0.85, do not increase substantially during the simulated melt. In some locations in the southeast, the simulated-melt T_B is less than 15 deg greater than the mean observed April T_B, compared to differences of 30 deg in the southwest (Fig. 3).

Fig. 3

The use of a modeled threshold T_B for each grid cell as a means of identifying melt is an improvement over the uniform step change in T_B for all grid cells used by Mote and others (1993). The use of a 31 deg change from observed January values in T_B to identify melt resulted in threshold brightness temperatures near 273 K at some locations along the southeast margin of the ice sheet. Observed brightness temperatures in this region seldom exceed 265 K, although melt is known to occur here.

The general patterns evident in both the simulated-melt T_B (Fig. 1) and April-emissivity (Fig. 2) maps result from variations in the accumulation rate across the ice sheet. The April-emissivity map (Fig. 2) closely resembles the latest accumulation map for Greenland (Ohmura and Reeh, 1991). Rotman and others (1982) demonstrated that accumulation rates could be determined from microwave emissivities for the dry-snow zone of the Greenland ice sheet. The southeast of the ice sheet experiences much higher emissions than the southwest (Fig. 2). This difference is due to increased accumulation in the southeast from the orographic lifting of moist air by the Icelandic low (Ohmura and Reeh, 1991). The microwave emissivity of the southwest is much lower due to lower accumulation rates. The regions of higher accumulation near the ice margin at 77° N and at 1500–2400 m a.s.l. from 69° N to 72° N, as identified by Ohmura and Reeh (1991), are also evident as regions of higher emissivity (Fig. 2).

AREAL MELT EXTENT

Values of the 37 GHz, horizontally polarized brightness temperatures for each day of available data were compared to the simulated-melt brightness temperatures for the given year. The simulated values for each year were used as threshold values to identify whether the snowpack in a given grid cell was experiencing melt. The spatial coverage of grid cells identified as experiencing melt each day was summed to quantify the areal extent of melt. The daily melt extents were then averaged on a monthly and seasonal (May–August) basis to produce mean monthly and mean seasonal melt extents. The mean melt extents are analogous to the average frequency of melt occurrence of all grid cells for a given month or season. This measurement does not indicate the intensity of the melt occurring in a grid cell on any given day. However, the climatic conditions averaged over months and seasons that produce intensive melt should usually be associated with more extensive and more frequent melt.

To merge the two data sets, the melt extents derived from each sensor for the period when both were operating (11 July–20 August 1987) are compared to determine the magnitude of error introduced by the sensor change. The comparison is made with and without the conversion of SMMR brightness temperatures using the linear regression of SMMR and SSM/I brightness temperatures. The mean melt extent detected by SMMR during the 20 d when both sensors were operating, after the conversion had been applied, is approximately 2.5% ~~less~~ more than that detected by SSM/I. This compares favorably to a 19% greater melt area detected by SSM/I without the conversion. With the conversion applied, the SSM/I identifies more melt on the two days of greatest melt extent, but the SMMR identifies more melt on two-thirds of the remaining days (Fig. 4). Examination of the spatial pattern of the difference in melt frequency identified by the two sensors evidences no regional bias. After the conversion is applied, the differences in melt frequency appear to be randomly distributed. The remaining differences are likely produced by the variation in the time of overpass for each sensor. The liquid water content has a strong diurnal cycle, and as a result, the T_B is also a function of the time of day during melt.

Fig. 4

In order to determine how well the microwave data can be used to represent changes in the surface climate of the ice sheet, the microwave-derived melt-extent time series was compared to the ablation rate measured at Qamanârssûp sermia. Braithwaite and Olesen (1990) published monthly values of the ablation rate at Qamanârssûp sermia (64°28′N), which were taken from a stake measurement at 790 m a.s.l. The ablation data were compared to the mean melt extent for each month for a region of the ice sheet that includes Qamañarssûp sermia. The ice sheet was divided into eight regions (Fig. 5), defined by topographic barriers that limit the

Fig. 5

transport of moisture, as shown by Ohmura and Reeh (1991). Monthly mean melt extents were calculated for each region. The ablation rate for Qamanârssûp sermia was compared to the monthly mean melt extent for Region 2. The topographic barriers that define each of these regions should serve as a barrier to sensible heat advection as well as moisture advection. As a result, changes in atmospheric circulation should have a distinctly different effect on melt occurrence in each of these regions.

An approximately linear relationship exists between the monthly mean melt extent for Region 2 and the monthly ablation rate for Qamanârssûp sermia (Fig. 6). The agreement is highly significant in June ($r^2 = 0.88$, significant at 95% confidence interval), marginally significant in July ($r^2 = 0.53$, significant at 90% confidence interval), but not significant in August ($r^2 = 0.31$). The overall agreement was statistically significant ($r^2 = 0.66$, significant at 99% confidence interval). The weaker relationship later in the season is likely the result of an increasingly heterogeneous snowpack. For example, due to the low emissivity of open water, a grid cell containing numerous meltwater ponds and wet snow may have a lower emissivity than is associated with wet snow alone. An increase in the amount of bare ice present in the analysis as the summer season progresses is another reason the relationship is weaker in August. At present, we cannot determine the occurrence of melt on bare ice with the passive microwave data. Early in the summer, much of the margin of the ice sheet and the outlet glaciers with exposed ice are excluded from analysis by the land mask. As the season progresses, the expanded area of bare ice means that more grid cells containing bare ice are included in the analysis.

Fig. 6

Given the linear relationship between the ablation rate and mean melt extent, the same climatic conditions that result in more ice ablation at Qamanârssûp sermia apparently also result in more frequent melt of the snowpack. Braithwaite and Olesen (1989) used the ablation rates at Qamanârssûp sermia as a measure of surface climate on the ice sheet. Therefore, we believe the monthly and seasonal mean melt extent values can serve as an indicator of climate variation.

In order to gain a better understanding of the spatial variation of melt occurrence, the daily melt extents were examined for extreme events, and the mean annual cycle of melt extent was calculated. The spatial extent of melt was evaluated on a daily basis first, to identify extreme events. The greatest melt extent during the 13 year period occurred on 4 and 5 July 1988. The melt extent reached 735 625 km^2 on 4 July and 711 875 km^2 on 5 July, covering approximately 44.6% and 43.2% of the unmasked area of the ice sheet, respectively. All of the ten days with the greatest melt extent during the 13 years occurred in 1988 or later (Table 1).

Table 1

The melt extent values for each day were averaged across the 13 years to produce a mean annual cycle of melt extent. Melt begins to occur in late April, and

coverage increases rapidly from mid-May until the maximum coverage occurs in mid-July (Fig. 7). The melt extent decreases rapidly from late July through mid-August, and typically terminates in late September. The time series of daily melt extent for individual years exhibit a large degree of temporal variability; this most likely results from the passage of synoptic-scale weather systems with concomitant changes in the amount of cloud cover and sensible heat advected onto the ice sheet.

Fig. 7

In order to understand the spatial variability in melt occurrence, the daily melt extent values were compiled into a map of the frequency of melt occurrence for each grid cell. The frequency of melt occurrence is defined as the percentage of days on which melt was detected during the 4 month summer period, May–August. The total area classified as melting during at least one day for the 13 years of data includes ~~1.09×10^6~~ km^2, covering approximately 66% of the unmasked area of the ice sheet. Melt was detected across the south dome of the ice sheet and as high as 3000 m a.s.l. in a region near 68° N, 37° W (Fig. 8). Melt occurred on more than 70% of the days in May–August along the ice sheet's western margin from 67° N to 70° N, but 60% of the region where melt occurred experienced melt on less than one day in 10 (Fig. 8).

1 090 000 km²

Fig. 8

The frequency of melt occurrence is probably underestimated. The land mask eliminates some snow surfaces at lower elevations that would likely experience more melt than adjacent locations at higher elevations. Also, daily averaging of the microwave data reduces the ability to identify instances in which melt occurred during only the hours of peak solar radiation or sensible-heat advection. A snowpack that experiences afternoon melt and refreezes in the evening may have a mean daily T_B for the grid cell that does not exceed the threshold value. This may be especially important early and late in the season due to the fewer hours of sunlight. The tendency of refrozen snow to have a lower T_B than fresh snow, due to increased volume scattering from the enlarged grain sizes, exacerbates this melt-detection problem. Finally, snowpack heterogeneity may cause difficulties in data interpretation with grid cells as large as 625 km^2 that may contain a large variation in elevation. A grid cell with both melting and refrozen snow may appear similar to a pixel with fresh snow, reducing the area classified as melting. This being said, the application of a uniform method over the entire time series should still allow the detection of tendencies in melt frequency and extent.

The daily melt-extent values were averaged into monthly and seasonal values to examine the melt-extent time series for inter-annual variations during the 13 year period. The most striking feature of the seasonal melt-

Fig. 9

extent time series (Fig. 9) is the apparent trend of increase in the area of average daily surface melt by approximately 5000 $km^2\,year^{-1}$. The average value of the daily melt extent for the entire 13 year period is approximately 133 000 km^2, and the linear trend represents a 3.8% annual increase. These findings are in general agreement with Braithwaite and others (1992), who suggested that the late 1980s had higher ablation rates than the early to mid-1980s. The 5 years of SSM/I data (1988–91) have a mean seasonal melt area 26% greater than the 8 years of SMMR data (1979–87). Contrary to evidence from the sensor-overlap period, it is still possible that the sensor change has contributed to some of the increase in detected melt area. However, the SMMR data alone have a positive trend of about 2500 $km^2\,year^{-1}$ in average daily melt area. (The year 1987 is included as a SMMR year because SMMR data are used from May through July to calculate the seasonal average; SSM/I data are used only in August.) All four summer months exhibited an increase in melt extent, with the most substantial increases in July and August (Fig. 10). July has a positive trend of nearly

Fig. 10

8200 $km^2\,year^{-1}$, compared to approximately 5500, 5400 and 1200 $km^2\,year^{-1}$ for August, June and May, respectively. Expressed as a percentage of the 13 year mean, August has the most positive trend, possibly indicating a longer melt season. June has the greatest variability in melt extent, from a low value of 69 800 km^2 average daily melt extent during the 1979 summer season to a high of 283 900 km^2 in 1987.

Examining the seasonal mean melt extents for each region, regions 2 and 3, which cover most of the western half of the ice sheet, ~~show~~ a statistically significant increase. The northerly regions, 4 and 5, show a slight trend toward increasing melt, but ~~this is not~~ significant. The melt-extent time series for the three southeastern regions, 6–8, remain relatively flat. In fact, region 7 shows a small, though statistically insignificant, trend toward decreasing melt over the 13 year period.

Table 2

Region 3, the largest of the eight regions and the one with the greatest mean melt extent (Table 2), has the largest trend in melt extent with a 6.7% annual increase (significant at the 99% confidence level). Region 2, located just south of region 3, showed a 4.2% annual increase over the 13 years (significant at the 99% confidence level). Regions 1 and 2, in the southwest, have the greatest percentage of area covered by melt, 24.4% and 17.2%, respectively (Table 2). The northeastern regions, 5 and 6, have the smallest percentage of mean-daily seasonal melt coverage, each at 5.3%. Monthly trends were examined for the two regions with significant seasonal trends. Region 2 had an increase of 900 $km^2\,year^{-1}$ (significant at the 95% confidence interval) in July and 500 $km^2\,yr^{-1}$ (significant at the 90 percent confidence interval) in August. Region 3 had an increase of 3000 $km^2\,year^{-1}$ (significant at the 90% confidence interval) in July and 4900 $km^2\,year^{-1}$ (significant at the 95% confidence interval) in August. The trends for both May and June were insignificant for

regions 2 and 3.

Overall, the trend of increasing mean melt area, analogous to increasing melt frequency, is confined to the southwest and west regions of the ice sheet, primarily late in the season. Because a large proportion of the total melt of the ice sheet occurs in these regions, the mean annual melt extent for the entire ice sheet also shows a positive trend.

SUMMARY AND CONCLUSION

A threshold value of 37 GHz, horizontally polarized T_B has been used to identify areas of melt on the Greenland ice sheet for 1979–91. By merging the data sets of two satellite microwave radiometers, a record of high spatial and temporal resolution of melt occurrence on the ice sheet has been developed. An examination of this detailed record provides evidence of a trend toward increasing seasonally averaged daily melt extent of about 3.8% annually. All four months examined, May–August, demonstrate a positive trend in melt coverage from 1979 to 1991, but the months of July and August account for approximately 70% of the seasonal trend. However, the agreement between the mean monthly melt extents and the measured ablation rates is weakest late in the summer season (July and August) when the trends are statistically most significant. Therefore, one must exercise caution in interpreting the melt-extent time series as indicative of increasing melt frequency or melt extent. Additionally, the apparent increase in mean melt extent is confined to the west and southwest of the ice sheet.

The loss of data near the margin of the ice sheet and the problems of diurnal variations of melt occurrence and spatial variations within a grid cell likely result in a bias toward identification of less melt than actually occurred. However, the relative melt-frequency values on a monthly and seasonal basis will prove useful in comparison to surface observations of ablation rates. These results should be used in conjunction with detailed surface meteorological observations to determine the usefulness of the passive-microwave satellite data in mass-balance studies. Continued monitoring of melt occurrence on the Greenland ice sheet is of particular value given the ongoing debate concerning global climate change. Recorded changes in melt frequency or total coverage should prove a powerful indicator of climate change in the Arctic.

ACKNOWLEDGMENTS

The authors thank S. Ekholm and the Danish National Survey and Cadastre for providing the elevation data for Greenland from the ERS-1 radar altimeter. We also thank Dr R. Braithwaite and K. Kuivinen for their useful comments on the surface conditions on the Greenland ice sheet. Additionally, we thank Dr Braithwaite, Dr M.

Palecki and an anonymous reviewer for their many constructive editorial comments on the manuscript. The SMMR and SSM/I gridded brightness-temperature data on CD-ROM were obtained from the National Snow and Ice Data Center, Boulder, CO, U.S.A. This work was supported by NASA training grant NGT-30127 and NASA grant NAGW-1266.

REFERENCES

Abdelrazik, M., F. Ulaby and H. Stiles. 1981. *A model describing the microwave emission from a multi-layer snowpack at 37 GHz.* Greenbelt, MD, Goddard Space Flight Center. (NASA CR-16708.)

Bindschadler, R. A. 1985. Contribution of the Greenland ice cap to changing sea level: present and future. *In* United States Department of Energy. *Glaciers, Ice Sheets, and Sea Levels: Effect of a CO_2-Induced Climatic Change. Report of a Workshop held in Seattle, Washington, September 13–15, 1984.* Washington, DC, National Academy Press, 258–266.

Bindschadler, R. A., H. J. Zwally, J. A. Major and A. C. Brenner. 1989. *Surface topography of the Greenland ice sheet from satellite radar altimetry.* Washington, DC, National Aeronautics and Space Administration. (NASA SP-503.)

Braithwaite, R. J. and O. B. Olesen. 1989. Detection of climate signal by inter-stake correlations of annual ablation data, Qamanârssûp sermia, West Greenland. *J. Glaciol.*, **35**(120), 253–259.

Braithwaite, R. J. and O. B. Olesen. 1990. A simple energy balance model to calculate ice ablation at the margin of the Greenland ice sheet. *J. Glaciol.*, **36**(123), 222–228.

Braithwaite, R. J., O. B. Olesen and H. H. Thomsen. 1992. Calculated variations of annual ice ablation at the margin of the Greenland ice sheet, West Greenland, 1961–90. *J. Glaciol.*, **38**(129), 266–272.

Budd, W. F., T. H. Jacka, D. Jenssen, U. Radok and N. W. Young. 1982. *Derived physical characteristics of the Greenland ice sheet.* Parkville, Victoria, University of Melbourne. Meteorological Department. (Publication 23.)

Chang, A. T. C., P. Gloersen, T. Schmugge, T. T. Wilheit and H. J. Zwally. 1976. Microwave emission from snow and glacier ice. *J. Glaciol.*, **16**(74), 23–29.

Chang, A. T. C., J. L. Foster, M. Owe, D. K. Hall, and A. Rango. 1985. Passive and active microwave studies of wet snowpack properties. *Nord. Hydrol.*, **16**(2), 57–66.

Foster, J. L., D. K. Hall, A. T. C. Chang and A. Rango. 1984. An overview of passive microwave snow research and results. *Rev. Geophys. Space Phys.*, **22**(2), 195–208.

Gloersen, P. and L. Hardis. 1978. The Scanning Multichannel Microwave Radiometer experiment. *In* Madrid, C., *ed. The Nimbus-7 User's Guide.* Washington, DC, NASA.

Gloersen, P., T. T. Wilheit, T. C. Chang, W. Nordberg and W. J. Campbell. 1974. Microwave maps of the polar ice of the Earth. *Bull. Amer. Meteor. Soc.*, **55**(12), 1442–1448.

Hofer, R. and C. Mätzler. 1980. Investigations on snow parameters by radiometry in the 3- to 60-mm wavelength region. *J. Geophys. Res.*, **85**(C1), 453–460.

Hollinger, J., R. Lo, G. Poe, R. Savage and J. Peirce. 1987. *Special Sensor Microwave/Imager User's Guide.* Washington, DC, Naval Research Laboratory.

Jezek, K. C. *and six others.* 1991. Comparison between SMMR and SSM/I passive microwave data collected over the Antarctic ice sheet. *Byrd Polar Research Center Technical Report* 91-03.

Kunzi, K. F., S. Patil and H. Rott. 1982. Snow-cover parameters retrieved from Nimbus-7 Scanning Multichannel Microwave Radiometer (SMMR) data. *IEEE Trans. Geosci. Remote Sensing*, **GE-20**(4), 452–467.

Mote, T. L., M. R. Anderson, K. C. Kuivinen and C. M. Rowe. 1993. Passive microwave-derived spatial and temporal variations of summer melt on the Greenland ice sheet. *Ann. Glaciol.*, **17**, 233–238.

National Snow and Ice Data Centre, 1992. *DMSP SSM/I brightness temperature grids for the polar regions on CD-ROM user's guide.* Boulder,

CO, National Snow and Ice Data Center.

Ohmura, A. and N. Reeh. 1991. New precipitation and accumulation maps for Greenland. *J. Glaciol.*, **37**(125), 110–118.

Peltier, W. R. and A. M. Tushingham. 1989. Global sea level rise and the greenhouse effect: might they be connected?. *Science*, **244**(4906), 806–810.

Rotman, S. R., A. D. Fisher and D. H. Staelin. 1982. Inversion of physical characteristics of snow using passive radiometric observations. *J. Glaciol.*, **28**(98), 179–185.

Stephenson, P. J. 1967. Some considerations of snow metamorphism in the Antrctic ice sheet in the light of ice crystal studies. *In* Ôura, H., *ed. Physics of snow and ice. International Conference on Low Temperature Science ... 1966, Sapporo, Japan. Proceedings. Volume I, Part 2.* Sapporo, Hokkaido University. Institute of Low Temperature Studies, 725–740.

Stiles, W. H. and F. T. Ulaby. 1980. The active and passive microwave response to snow parameters. 1. Wetness. *J. Geophys. Res.*, **85**(C2), 1037–1044.

Thomas, R. H. *and 8 others*. 1985. *Satellite remote sensing for ice sheet research.* Washington, DC, National Aeronautics and Space Administration. (Technical Memorandum 86233.)

Tinga, W. R., W. A. G. Voss and D. F. Blossey. 1973. Generalized approach to multiphase dielectric mixture theory. *J. Appl. Phys.*, **44**(9), 3897–3902.

Tiuri, M. and H. Schultz, 1980. Theoretical and experimental studies of microwave radiation from a natural snowfield. *In* Rango, A., ed. *Microwave remote sensing of snowpack properties. Proceedings of a workshop ... Fort Collins, Colorado, May 20–22, 1980.* Washington, DC, National Aeronautics and Space Center. (Conference Publication 2153.)

Ulaby, F. T. and W. H. Stiles. 1980. The active and passive microwave response to snow parameters. 2. Water equivalent of dry snow. *J. Geophys. Res.*, **85**(C2), 1045–1049.

Ulaby, F. T., R. K. Moore and A. K. Fung. 1986. *Microwave remote sensing: active and passive., Vol. 3.* Reading, MA., Addison-Wesley.

Weidick, A. 1985. *The ice cover of Greenland.* København, Grønlands Geologiske Undersøgelse. (Gletscher-Hydrologiske Meddelelser 85/4.)

Zwally, H. J. 1977. Microwave emissivity and accumulation rate of polar firn. *J. Glaciol.*, **18**(79), 195–215.

Zwally, H. J. 1989. Growth of the Greenland ice sheet: interpretation. *Science*, **246**(4937), 1589–1591.

The accuracy of references in the text and in this list is the responsibility of the authors, to whom queries should be addressed.

FIGURE CAPTIONS

Fig. 1. Mean values of the simulated 37 GHz brightness temperatures associated with summer-melt conditions for each year 1979–91. The brightness temperatures for each year are calculated from a simple microwave-emission model of the snowpack with 1% liquid-water content.

Fig. 2. Mean April microwave emissivities at 37 GHz determined from observed April brightness temperatures and estimated 10 m firn temperatures.

Fig. 3. Simulated summer-melt 37 GHz brightness temperatures minus mean observed brightness temperatures for April 1979–91.

Fig. 4. Daily melt area identified in July and August 1987 with SSM/I data vs the melt area identified by SMMR data before and after a conversion of the SMMR data to account for calibration differences between the two sensors.

Fig. 5. Eight topographically defined regions of the ice sheet, based on the ice-sheet regions defined by Ohmura and Reeh (1991).

Fig. 6. Mean monthly melt-extent values for region 2 of the ice sheet versus stake-ablation rates measured at Qamanârssûp sermia, as given by Braithwaite and Olesen (1990).

Fig. 7. A time series of the mean daily melt-extent values for the years 1979–91 demonstrating the typical annual cycle of melt coverage on the ice sheet.

Fig. 8. Percentage of days identified as melting during May–August of 1979–91 from passive-microwave data.

Fig. 9. Seasonal (May–August) averages of the daily melt extent as identified with passive-microwave data.

Fig. 10. Monthly averages of the daily melt extent as identified with passive-microwave data.

Table 1. Spatial extent of melt and percentage of ice sheet covered by melt for the 10 d of most extensive melt during 1979–91

Date	*Melt extent* km^2	*Melt extent as % of unmasked area*
4 Jul 1988	735 625	44.6
5 Jul 1988	711 875	43.2
20 Jul 1989	612 500	37.2
15 Jul 1989	606 250	36.8
9 Jul 1988	600 635	36.4
8 Jul 1988	576 875	35.0
5 Aug 1990	576 250	35.0
10 Jul 1991	575 875 575 625	34.4 34.9
6 Jul 1988	566 875	34.4
26 Jul 1990	563 125	34.2

Table 2. May–August mean melt area and per cent coverage for each of the eight topographically defined regions (within land/water mask)

Region	*Total area*	*Mean melt extent* km^2	*Mean melt extent as % of unmasked area*	*Mean Elevation* m a.s.l.
1	51 250	12 500	24.4	1633
2	69 375	11 900	17.2	2140
3	539 375	45 000	8.3	2240
4	221 875	15 000	6.8	1768
5	410 625	21 600	5.3	2046
6	105 000	5 600	5.3	2551
7	90 000	7 000	7.8	2333
8	160 625	14 400	9.0	2222
Total	~~1 670 625~~ 1648 125	~~132 900~~ 133 000	8.0	2128

Revised

Fig: 1

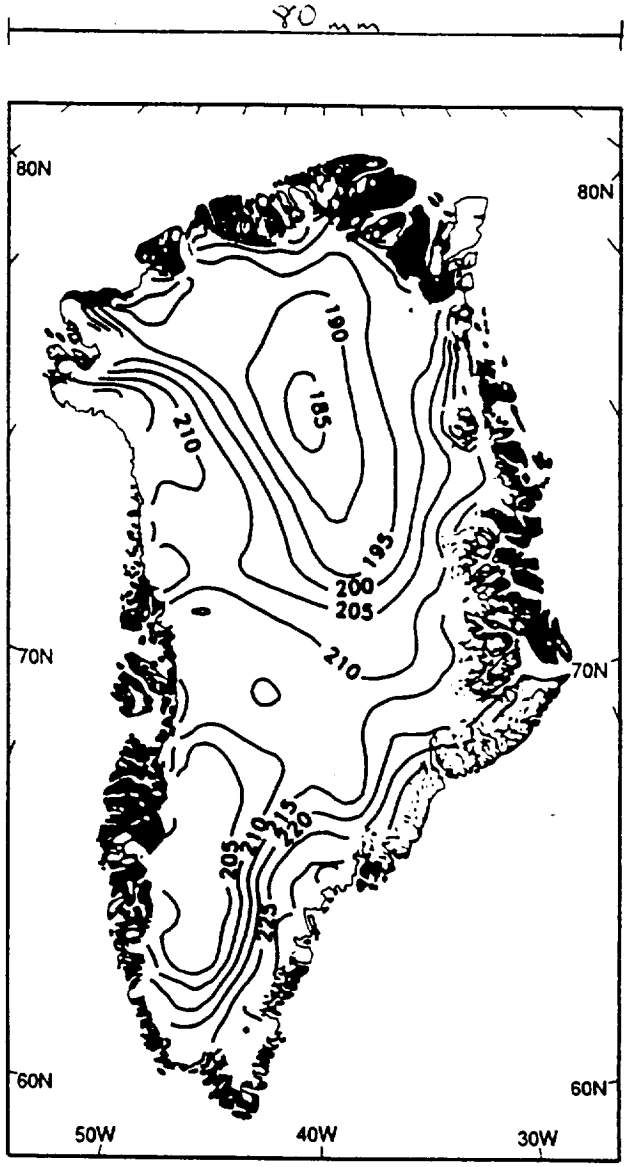

Fig. 1. Mean values of the simulated 37 GHz brightness temperatures associated with summer-melt conditions for each year 1979–91. The brightness temperatures for each year are calculated from a simple microwave-emission model of the snowpack with 1% liquid-water content.

Revised
Fig. 2

80 mm

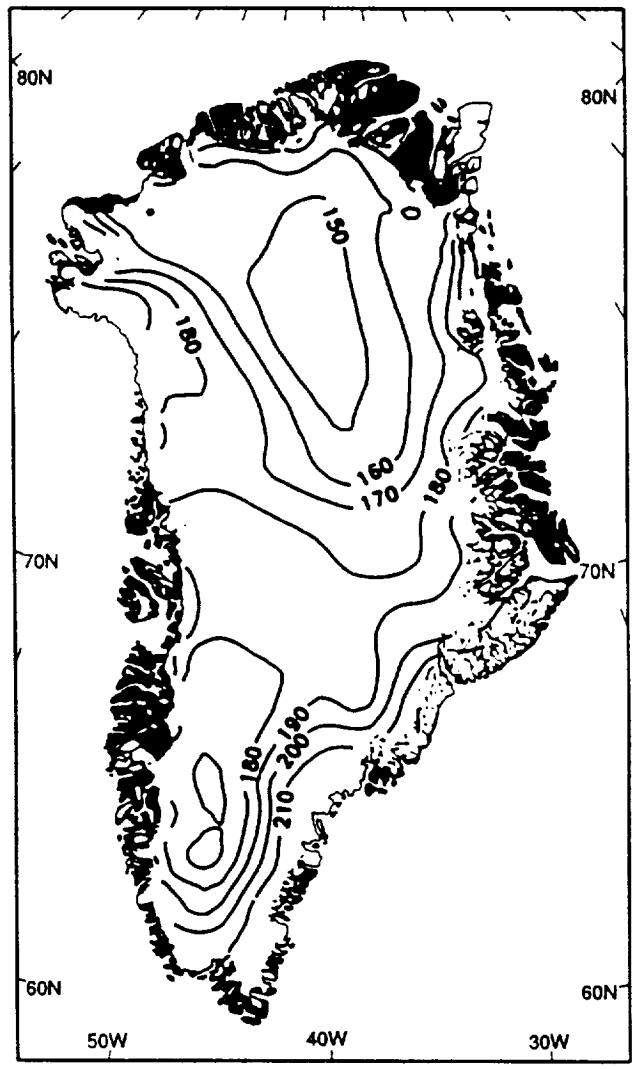

Fig. 2. Mean April microwave emissivities at 37 GHz determined from observed April brightness temperatures and estimated 10 m firn temperatures.

Revised
Fig: 3

80 mm

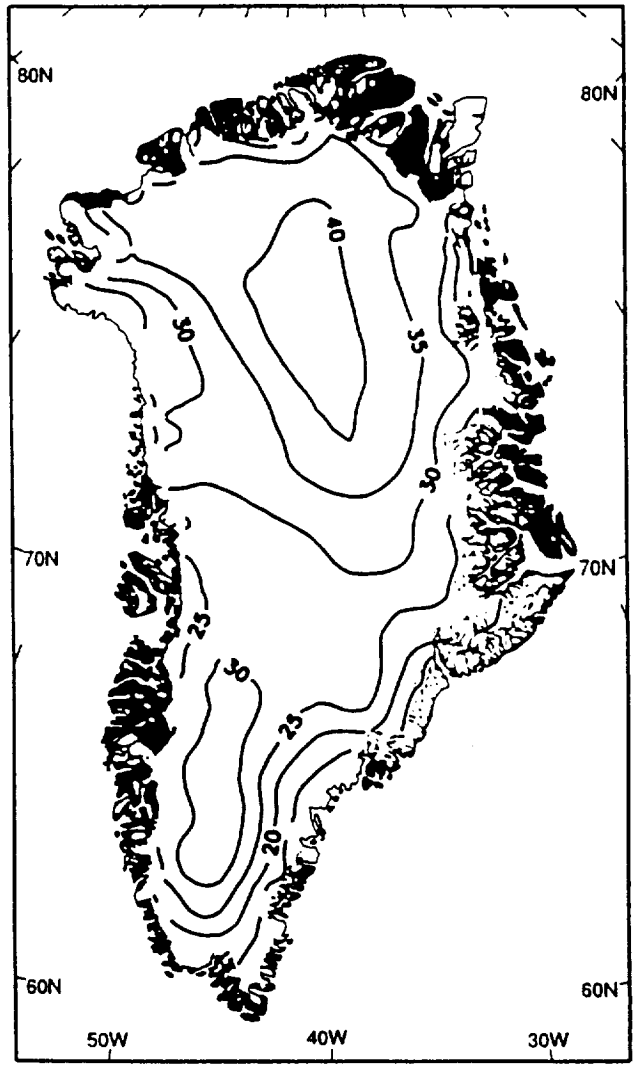

Fig. 3. Simulated summer-melt 37 GHz brightness temperatures minus mean observed brightness temperatures for April 1979–91.

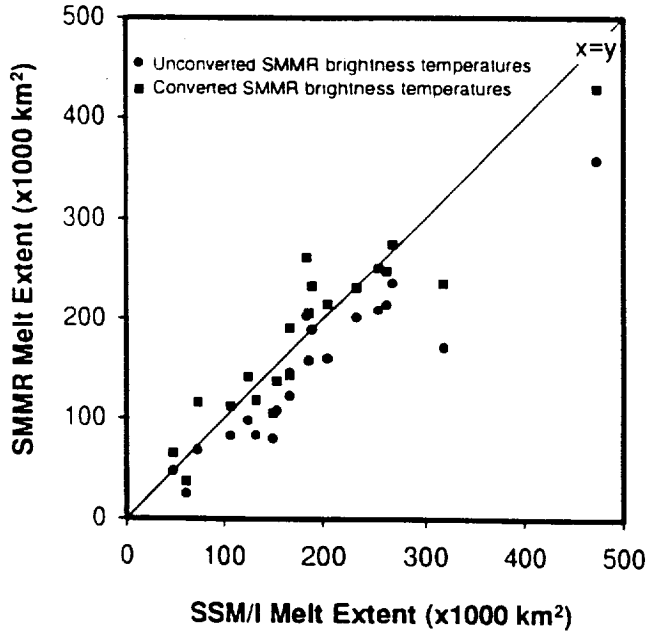

Fig. 4. Daily melt area identified in July and August 1987 with SSM/I data vs the melt area identified by SMMR data before and after a conversion of the SMMR data to account for calibration differences between the two sensors.

Revised
Fig: 5

80mm

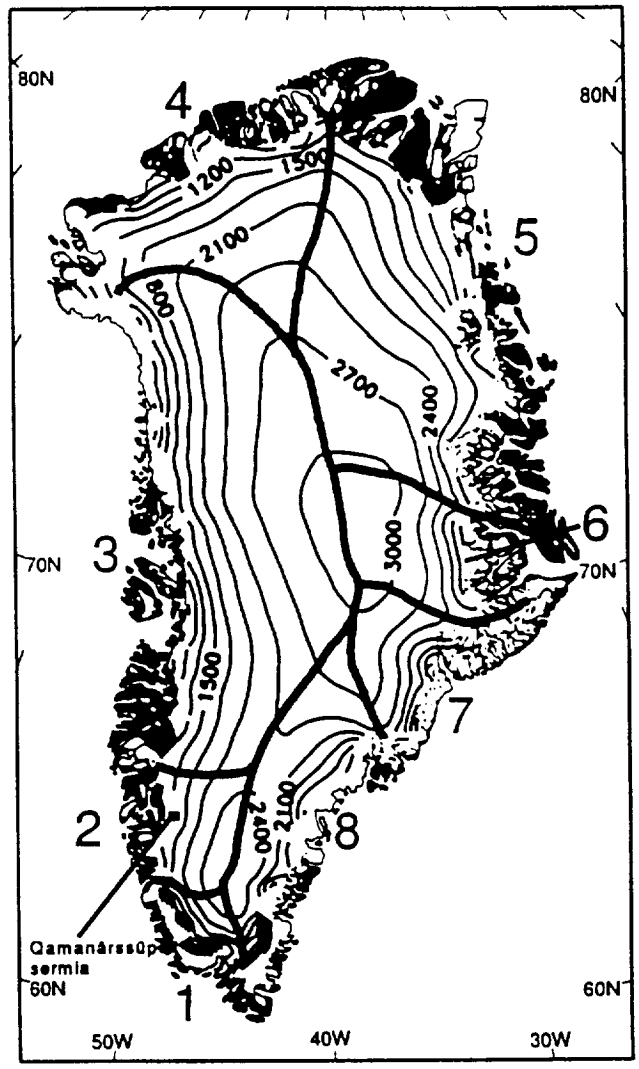

Fig. 5. Eight topographically defined regions of the ice sheet, based on the ice-sheet regions defined by Ohmura and Reeh (1991).

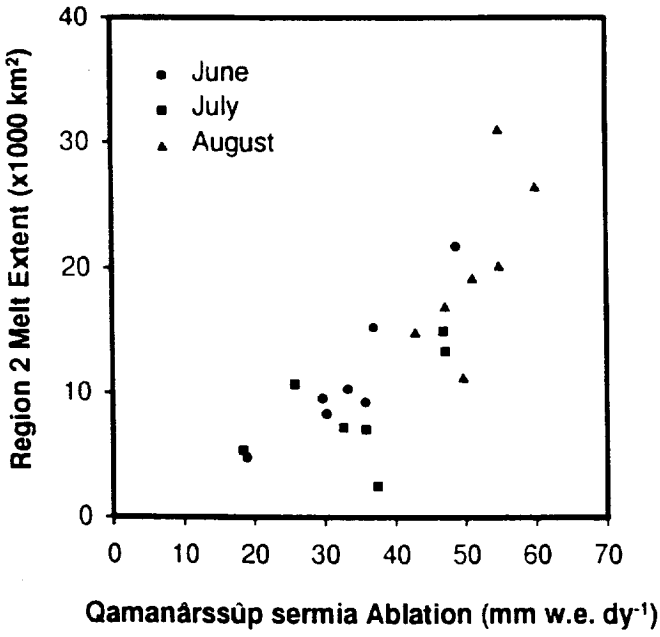

Fig. 6. Mean monthly melt-extent values for region 2 of the ice sheet versus stake-ablation rates measured at Qamanârssûp sermia, as given by Braithwaite and Olesen (1990).

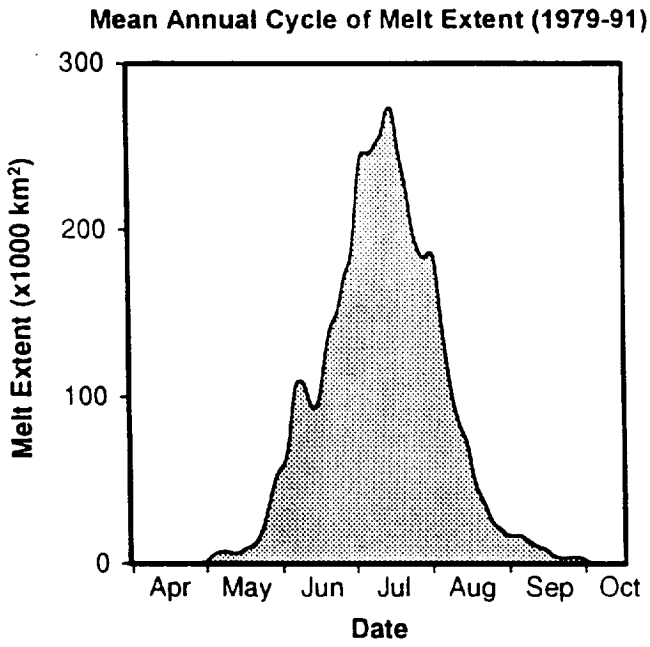

Fig. 7. A time series of the mean daily melt-extent values for the years 1979–91 demonstrating the typical annual cycle of melt coverage on the ice sheet.

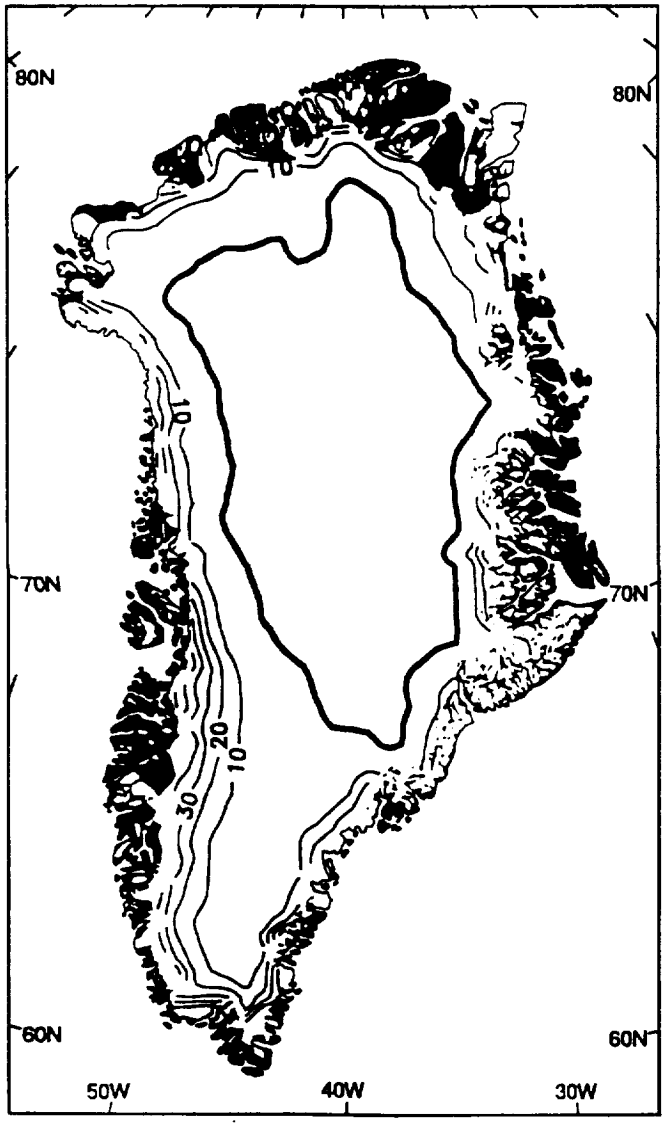

Fig. 8. Percentage of days identified as melting during May–August of 1979–91 from passive-microwave data.

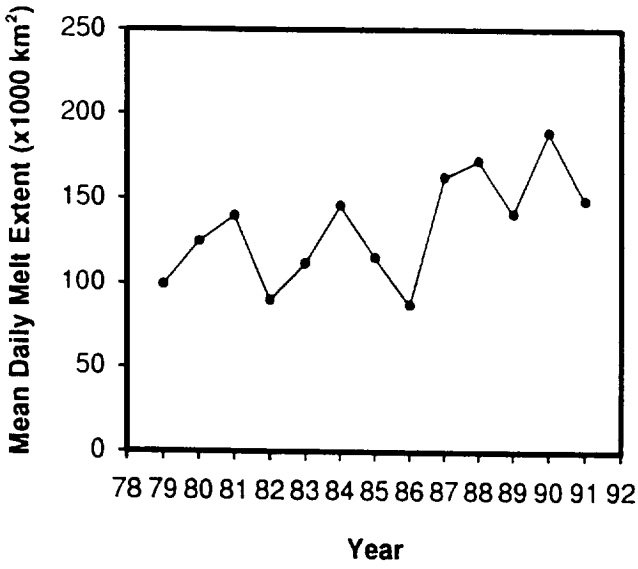

Fig. 9. Seasonal (May–August) averages of the daily melt extent as identified with passive-microwave data.

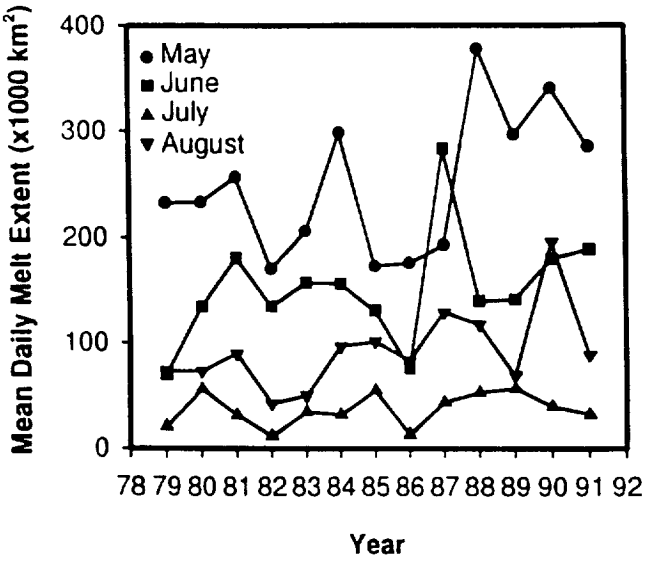

Fig. 10. Monthly averages of the daily melt extent as identified with passive-microwave data.

Reprinted from the preprint volume of the FOURTH CONFERENCE ON POLAR METEOROLOGY AND OCEANOGRAPHY, 15-20 Jan 1995, Dallas, TX. Published by the American Meteorological Society, Boston, MA.

4.5

ATMOSPHERIC CONDITIONS DURING SNOWMELT AT DYE 2, GREENLAND

Mark R. Anderson*, Clinton M. Rowe, and Kristin L. George

Meteorology/Climatology Program
Department of Geography
University of Nebraska-Lincoln

Thomas L. Mote

Department of Geography
University of Georgia

1. INTRODUCTION

Scientific interest in the potential effects of climate change on the polar regions has increased since computer simulations have shown that high latitudes are likely to experience enhanced warming. The response of the polar ice sheets to a projected warming has been of particular interest. To determine how snowmelt on the Greenland ice sheet responds to climate variations, surface snowmelt and concurrent atmospheric conditions were examined. As part of the investigation, a field program was undertaken to obtain surface weather observations and measurements of snow conditions in the late spring/early summer of 1993 at Dye 2, Greenland (66°29'N, 46°17'W, 2117m a.s.l.). Hemispheric geopotential height data for several levels and sea level pressure data were acquired for the period of field operation. Comparisons between the synoptic-scale atmospheric conditions and the surface measurements during individual melt events are presented.

2. DATA

Dye 2, Greenland was chosen because of its location in the percolation zone of the ice sheet (Benson, 1962), providing seasonal differences in snowmelt (Figure 1). An automated weather station deployed at Dye 2 recorded hourly temperature, relative humidity, wind speed and direction, downward and upward components of shortwave and longwave radiation and snowpack temperatures at 16 levels between the surface and a depth of 2m. Observations were acquired from 11 June until 13 July.

Surface and 850, 700, 500 and 250 hPa level initial analyses from the ECMWF model at 0 and 12 UTC were archived for June and July and were used to specify the atmospheric circulation. The onset, duration and extent of surface snowmelt on the Greenland ice sheet were determined using a threshold technique based on the gridded 37 GHz horizontal brightness temperatures recorded by the SSM/I sensor on board the Defense

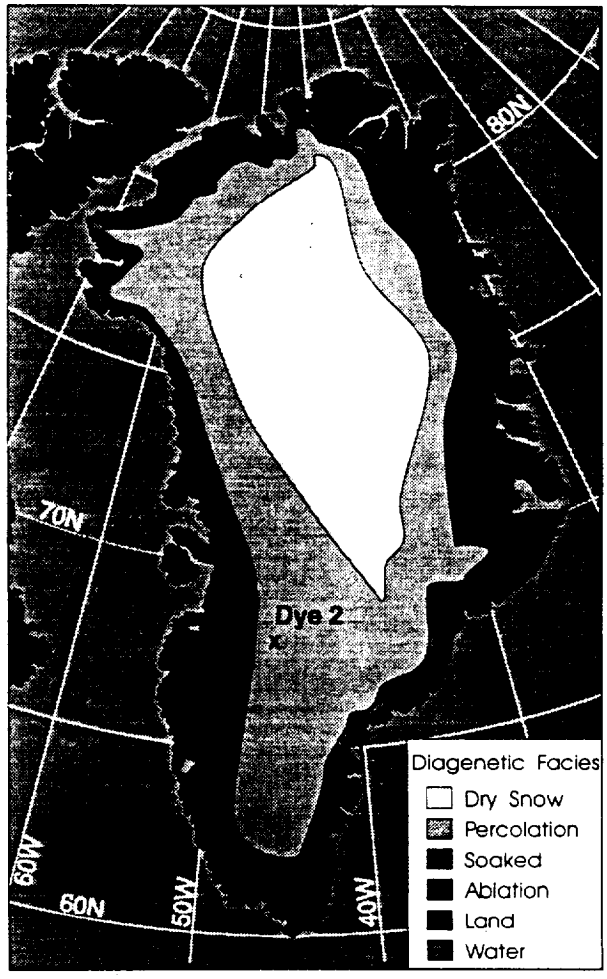

Figure 1 Location map of Dye 2 on the Greenland ice sheet, with snow facies after Benson (1962).

*Corresponding author address: Mark R. Anderson, Meteorology/Climatology Program, 324 Avery Hall, Univ. of Nebraska-Lincoln, Lincoln, NE 68588-0135

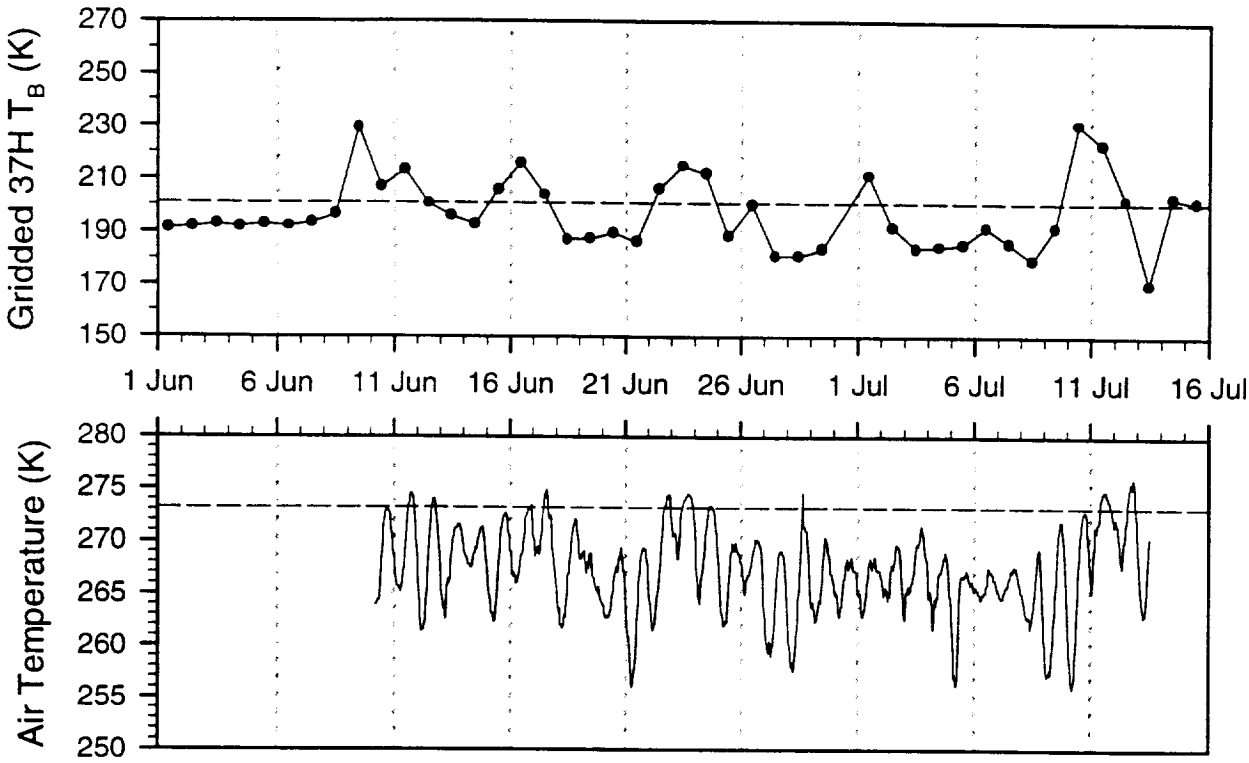

Figure 2 (a) Daily gridded SSM/I brightness temperatures for Dye 2, Greenland. Values above the threshold (dashed line) represent periods of surface snowmelt. (b) Surface air temperatures from Dye 2, Greenland.

Meteorological Satellite Program (DMSP) F-11 satellite (Mote, 1994, Mote and Anderson, 1994). The brightness temperatures for the grid cell containing Dye 2 were used to specify periods of snowmelt between 11 June and 13 July. Brightness temperatures across the ice sheet were examined to determine the melt extent on selected days.

3. RESULTS

The first melt event at Dye 2 during the study period began on 9 June, 1993 when the observed gridded microwave brightness temperature surpassed the threshold value (Figure 2a) and continued for the subsequent 3 days. This was also the first time during the study period when surface air temperatures reached or exceeded freezing at Dye 2 (Figure 2b). Analysis of the microwave data for the entire ice sheet during 6-9 June shows that surface snowmelt occurring to the southwest of Dye 2 progressed northeastward to the site by 9 June. During this melt event a surface low was moving up the Newfoundland coast toward southern Greenland (Figure 3a) and, at 700 hPa, a ridge was present over Greenland. Together, the surface and upper air flow combined to produce strong southerly flow and warm air advection over southern Greenland (Figure 3b).

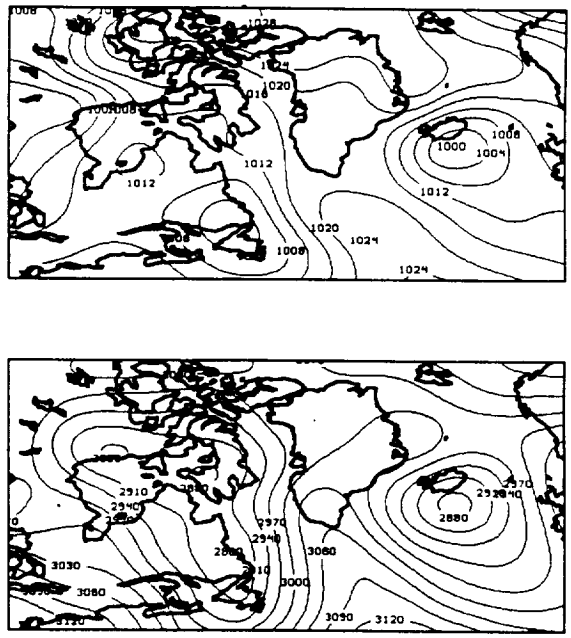

Figure 3 (a) Mean sea level pressure and (b) 700 hPa analysis for 00 UTC 9 June 1993.

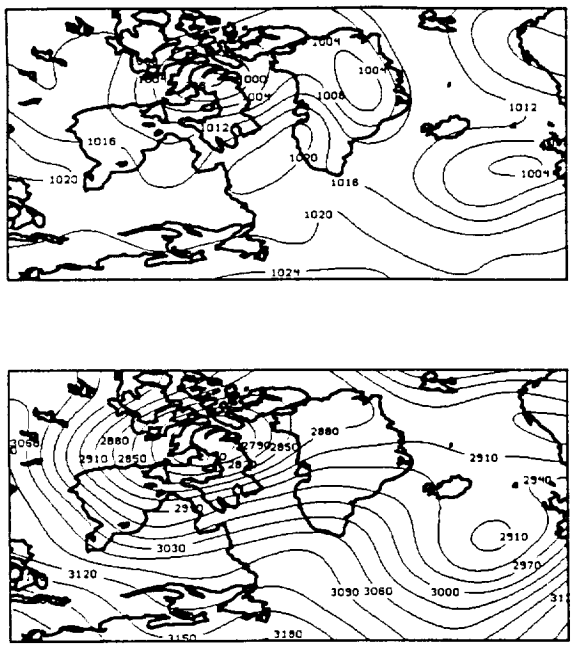

Figure 4 (a) Mean sea level pressure and (b) 700 hPa analysis for 00 UTC 18 June 1993.

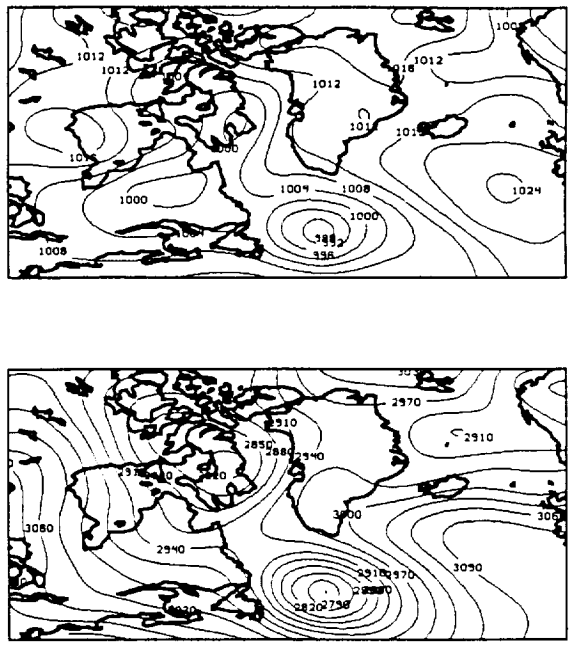

Figure 5 (a) Mean sea level pressure and (b) 700 hPa analysis for 00 UTC 22 June 1993.

On 13 June the gridded brightness temperatures at Dye 2 fell below the melt threshold and surface air temperatures stayed below freezing as the surface low and associated upper level trough moved eastward. This resulted in weaker, more easterly flow over Greenland and a retreat of the region experiencing melt. On 15 June, another surface low and associated upper level trough moved over from Hudson Bay to Baffin Bay, again bringing southerly flow. Surface air temperatures went above freezing and the gridded brightness temperatures exceeded the melt threshold. This pattern persisted until 18 June when the ridge broke down the trough moved over Greenland, causing a more zonal pattern with a west-northwesterly flow curtailing melt (Figure 4).

Another melt event occurred on 22-24 June (Figure 2a). During this period atmospheric conditions were similar to those of the earlier melt events, but with a more intense low off the Newfoundland coast and a less pronounced ridge at 700 hPa (Figure 5). As the system moved to the east-northeast, the flow turned more northerly, cold air advection replaced warm air advection, and melting stopped.

The last melt event, 10-12 July, showed similar features to the other events. Before surface snow melt started there was a strong surface low and upper level trough to the west. By the end of the melt event, the surface low and trough had moved east of Greenland. Unfortunately, during the actual melt event (8-11 July), we do not have the surface or upper air data to determine the actual path of the system and will therefore not discuss this event. However, it does appear to follow the other cases observed during the study period.

4. SUMMARY AND CONCLUSIONS

An investigation was conducted of the synoptic-scale atmospheric conditions during melt periods at Dye 2, Greenland that were identified using passive microwave data. Results indicate a strong relationship between the occurrence of surface snowmelt and the synoptic state. Warm air advection caused by a southerly component to the flow over Greenland was largely responsible for the melt events. The warm air advection resulted from low pressure systems moving northward from the Newfoundland coast to southern Greenland. Further comparisons between the synoptic-scale atmospheric conditions and satellite- or surface-based observations of melt should be useful in assessing the possible impact of climate change on the Greenland ice sheet.

5. ACKNOWLEDGMENTS

This work was supported by NASA grant NAGW-1266.

6. REFERENCES

Benson, C.S., 1962: Stratigraphic studies in snow and firn of the Greenland ice sheet, CRREL Res. Rep. 70, CRREL, Hanover, NH, 93pp.

Mote, T., 1994: Variations in passive microwave measurements of melt on the Greenland ice sheet and associated northern hemisphere atmospheric circulation. Ph.D. dissertation, 189 pages.

Mote, T. and M. Anderson, 1994: Variations in snowpack melt on the Greenland ice sheet based on passive microwave measurements. J. of Glac., (in press).

JOURNAL OF GEOPHYSICAL RESEARCH, VOL. 99, NO. C7, PAGES 14,303–14,309, JULY 15, 1994

Springtime microwave emissivity changes in the southern Kara Sea

Robert G. Crane
Earth System Science Center and Department of Geography, The Pennsylvania State University, University Park

Mark R. Anderson
Department of Geography, University of Nebraska, Lincoln

Abstract. Springtime microwave brightness temperatures over first-year ice are examined for the southern Kara Sea. Snow emissivity changes are revealed by episodic drops in the 37- to 18-GHz brightness temperature gradient ratio measured by the Nimbus 7 scanning multichannel microwave radiometer. We suggest that the negative gradient ratios in spring 1982 result from increased scatter at 37 GHz due to the formation of a near-surface hoar layer. This interpretation is supported by the results of a surface radiation balance model that shows the melt signature occurring at below freezing temperatures but under clear-sky conditions with increased solar input to the surface. Published observations from the Greenland ice cap show a surface hoar layer forming under similar atmospheric conditions owing to the increased penetration and absorption of solar radiation just below the surface layer. In spring/early summer 1984 similar gradient ratio signatures occur. They appear to be due to several days of freeze-thaw cycling following the movement of a low-pressure system through the region. These changes in surface emissivity represent the transition from winter to summer conditions (as defined by the microwave response) and are shown to be regional in extent and to vary with the synoptic circulation.

Introduction

The energy budget over sea ice is largely determined by the radiation balance at the surface. This balance changes rapidly during the melt season, when the physical properties of the surface are altered; the most dramatic effects are shown in the surface albedo during the progression from snow melt to ice breakup. The albedo for sea ice with a fresh snow cover is about 75-80%. This decreases to about 40-60% for old ice and drops to about 10% for open water. As melt progresses, there is a significant decrease in the regional albedo [*Robinson et al.*, 1986, 1992]. The springtime transition from winter to summer conditions thus represents a critical period when ocean-atmosphere interactions undergo rapid fluctuations owing to changing snow cover conditions, ice thickness, and ice concentration.

This transition period takes on added significance when one considers the results of several modeling experiments that suggest that the equilibrium ice thickness is strongly influenced by the surface albedo parameterization and the timing of the snow melt [*Shine and Crane*, 1984; *Shine and Henderson-Sellers*, 1985; *Ledley*, 1991]. Similarly, all of the current general circulation model experiments for a doubled CO_2 climate show a considerable enhancement of the warming at high latitudes, with much of the warming being attributed to the temperature-albedo feedback in the seasonal sea ice zone (SSIZ), the region of high-latitude seas that experiences a seasonal ice cover [e.g., *Dickinson et al.*, 1987]. Consequently, it becomes even more important that we develop a clearer understanding of ice processes during this period in the seasonal cycle to validate the results of both atmospheric and oceanic circulation models and of stand-alone dynamic and thermodynamic models of the polar sea ice cover.

Several hypotheses concerning spring melt could be suggested, the simplest and most obvious being that melt will follow a zonal progression related to the latitudinal change in the solar forcing with time throughout the melt season. An alternative possibility is that the melt would vary on a local basis according to regional features of the synoptic-scale atmospheric circulation. Tentative support for this second hypothesis comes from earlier work by *Crane et al.* [1982] using data from the single channel electrically scanning microwave radiometer on Nimbus 5. The synoptic pattern of snow melt over the sea ice is further demonstrated in the present paper; we suggest that spring and early summer changes in satellite-derived microwave brightness temperatures occur on a regional basis in response to the surface radiation budget and synoptic variations in cloud cover. From the perspective of passive microwave radiometry, these emissivity changes represent the start of the transition from winter to summer ice conditions.

Crane and Anderson [1989] describe the spring melt pattern in the Kara/Barents Sea in 1984, suggesting that changes in the ice cover in the Barents Sea were dominated by ice advection, while ice conditions in the Kara Sea were domi-

Copyright 1994 by the American Geophysical Union.

Paper number 94JC00381.
0148-0227/94/94JC00381$05.00

nated by surface melt processes. The present paper concentrates on the Kara Sea but focuses on microwave emissivity changes occurring in the spring and early summer. In previous work we have suggested that similar changes observed in other parts of the SSIZ might be attributed to an increase in grain size within the snow pack [*Anderson*, 1987; *Crane and Anderson*, 1989]. Earlier work by *Anderson and Robinson* [1985] also shows that the areas where this signal appears are the same regions in which snow melt first becomes apparent in the visible-band satellite imagery, but the change is observed in the microwave brightness temperatures several weeks before it can be seen in the visible-band data.

Spring/summer microwave signatures of snow covered sea ice

The sea ice data are vertically polarized brightness temperatures from the 18-GHz and 37-GHz channels of the Nimbus 7 scanning multichannel microwave radiometer (SMMR). The SMMR is a dual polarized five-frequency instrument with channels at 6.6, 10.69, 18.0, 21.0, and 37.0 GHz. The resolution is frequency dependent and varies from 148 km by 151 km at 6.6 GHz to 27 km by 32 km at 37 GHz. The present study uses the daily averaged 18-GHz and 37-GHz channels mapped to the 25-km special sensor microwave/imager grid available on CD-ROM. The sensor operated only on alternate days owing to power limitations. The data presented in Figures 1 and 2 thus represent observations made at 2-day intervals.

For microwave remote-sensing purposes, the ice cover is usually assumed to be a simple mix of first-year ice, multiyear ice, and open water. Multiyear ice in a microwave context is ice that has undergone the transition to a lower-density, less saline ice pack following brine drainage during the summer melt season. Differences in emissivity between ice and open water and the variation in emissivity with frequency for first-year and multiyear ice are used for the operational retrieval of ice type and concentration [*Cavalieri et al.*, 1984; *Gloersen and Cavalieri*, 1986]. The method is based on empirically derived functions that utilize two spectral ratios. The first is a polarization ratio with the polarization difference between ice and open water being used to estimate ice coverage. The second uses a spectral gradient ratio to derive information on ice type (the multiyear ice fraction). The gradient ratio makes use of the emissivity difference between first-year and multiyear ice, which changes as a function of frequency, with the difference between the 37-GHz and 18-GHz emissivities being positive for first-year ice and strongly negative for multiyear ice. Snow cover is usually neglected in these calculations.

The limited snow cover observations that are available suggest that snow depth generally varies from about 0 to 1.0 m with a mean of about 0.2-0.4 m [*Hanson*, 1980; *Barry*, 1983]. Since the skin depth for dry snow (in the SMMR frequency range) is of the order of 0.5 to 2.0 m, it is usually assumed that except for an unusually thick snow cover or during the melt season, snow will have little effect on the brightness temperature over sea ice [*Zwally and Gloersen*, 1977; *Chang et al.*, 1976, 1982]. During melt, however, several changes occur that do influence the emissivity. The most dramatic of these is a substantial increase in emissivity when the pack becomes "wet." As the pack warms to the melting point, there is an increase in the free-water content of the pack, which forms a thin film around the grains. This film reduces internal scatter and increases the emissivity for all ice types at all frequencies [*Stiles and Ulaby*, 1980; *Livingstone et al.*, 1987]. The resulting spike in microwave brightness temperatures is usually assumed to mark the transition to summertime ice conditions, during which time the effectiveness of the operational ice retrieval algorithms are considerably reduced. The present paper demonstrates that equally significant snow emissivity changes may occur earlier in the spring, before substantial warming has occurred, and that these changes may also have a large impact on ice retrievals.

Because of their frequency dependence, the snow emissivity effects are also observed in the gradient ratio referred to above. In this case the spectral gradient ratio uses the difference between the 18-GHz and 37-GHz vertically polarized brightness temperatures and is given by

$$GR = \frac{TB_{v,37} - TB_{v,18}}{TB_{v,37} + TB_{v,18}} \quad (1)$$

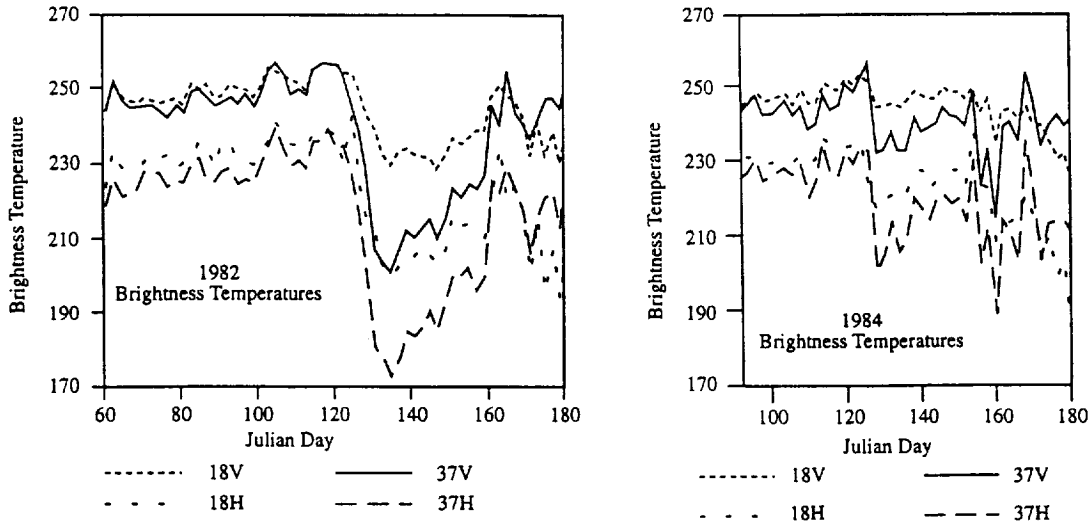

Figure 1. The 18- and 37-GHz brightness temperatures averaged over a 160 by 160 km block of pixels in the central southern Kara Sea for 1982 (a) and 1984 (b).

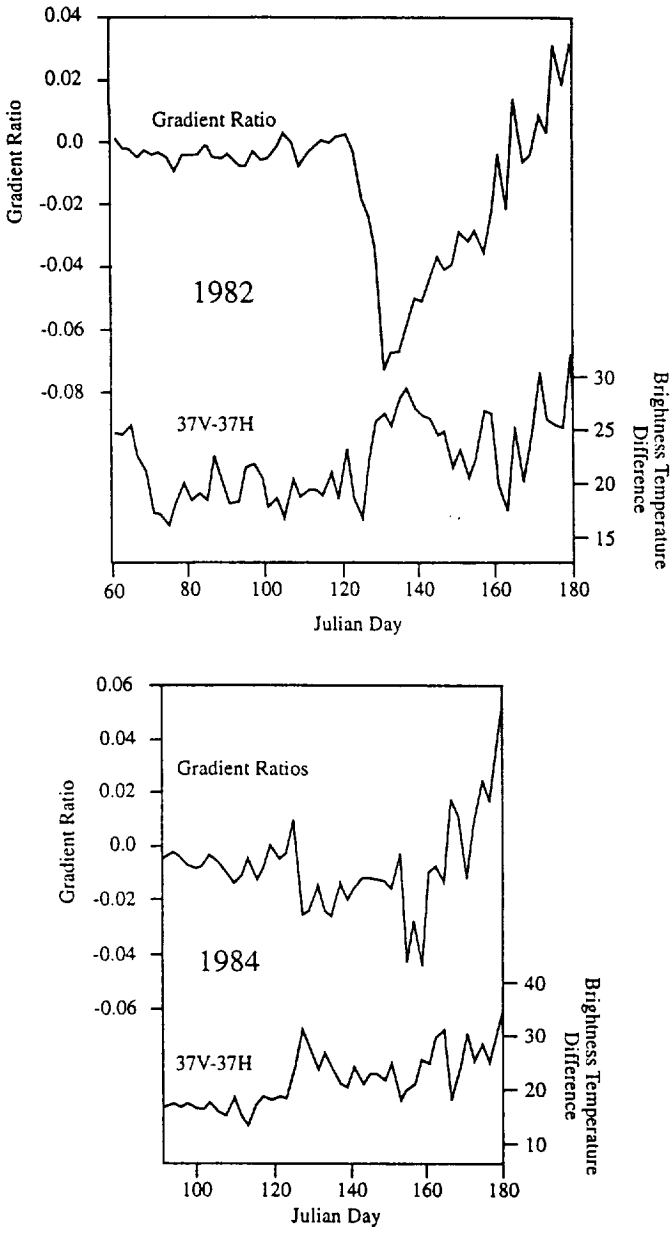

Figure 2. Gradient ratios and 37V-37H differences computed from the data in Figure 1 for 1982(a) and 1984 (b).

Using the gradient ratio isolates changes that are frequency dependent (such as changes in snow crystal size) from those that affect both frequencies together (such as a change in physical temperature). In the present case the drop in the 37-GHz channel gives rise to negative gradient ratios. As negative gradient ratios are also indicative of multiyear ice, the present discussion of snow melt applies only to first-year ice regions. First-year ice in this context is defined in terms of microwave emissivity and represents ice that has not undergone a summer melt event. Once melt occurs, brine drainage from the ice pack changes the microwave emissivity significantly, and the resulting ice is referred to as multiyear ice regardless of its age. In practical terms, therefore, this analysis is limited to the seasonal sea ice zone in areas where there is little influx of multiyear ice from the Arctic Basin.

Springtime brightness temperature changes in the Kara Sea: 1982 and 1984

For this analysis the 18-GHz and 37-GHz brightness temperatures and the vertically polarized gradient ratios are averaged for an 180 km by 180 km block of pixels in the central portion of the southern Kara Sea. The brightness temperatures are plotted as a time series in Figure 1, and the gradient ratios are shown in Figure 2. The microwave data indicate that the southern Kara Sea remained ice covered through July in 1982 but that ice cover began to decrease in late June in 1984 and the region was clear of ice by July 7 of that year. The features of interest here are the episodic drops in brightness temperature that occur in both years.

These periods of lower brightness temperature are matched by periods of lower negative gradient ratios. Although brightness temperatures decrease at both 18 GHz and 37 GHz, the drop at 37 GHz is much greater. It is this increased difference that gives the increase in negative gradient ratios that would normally be interpreted as an increase in the multiyear ice fraction. After several weeks, however, the negative gradient ratios revert to the positive ratios characteristic of first-year ice. This drop in gradient ratios occurs too early in the season to be due to the formation of multiyear ice, and furthermore, multiyear ice once formed does not revert to first-year ice as this appears to do. An examination of the total and multiyear ice concentration maps for these time periods also shows that there is no advection of multiyear ice into or out of the area (possible sources of multiyear ice would be ice advected into the Kara Sea from the northeast or fast ice that remained along the coast from the previous summer). We will show later that in 1982 these changes occur under periods of extended clear-sky conditions and are thus unlikely to be the result of an atmospheric effect. This indicates that the change in gradient ratios is due to a change in the emissivity of the first-year ice, and the most likely possibility is that it represents a change in the overlying snow cover. The timing of these emissivity changes is examined further in the present paper, using a radiative transfer model to calculate the surface radiative fluxes during this early spring period.

The surface radiation budget

The radiative transfer model is the same as that described by *Francis et al.* [1991] and uses a δ2-stream approach for calculating both solar and terrestrial fluxes. The δ2-stream solution is calculated for each layer in the model (where the column has been divided into layers having constant absorbing and scattering properties). The calculations are performed over 26 spectral intervals for the solar component (0.25 μm-4.3 μm) and for 18 intervals through the infrared spectrum from 4.5 μm to 62.5 μm. Clouds are treated explicitly as scatterers in the visible, and as absorbing features in the infrared. The clouds are assumed to be perfect absorbers outside of the 8.3-μm to 12.5-μm window and to act as gray bodies within the window region, where the emissivity is calculated as a function of cloud liquid-water content. The liquid-water content, in turn, is estimated from the visible optical depth. Infrared absorption due to ozone, carbon dioxide, and water vapor is included, and random overlap is assumed between the water vapor continuum and other absorbing species. Absorption in the visible is by oxygen, ozone, and water vapor, and random overlap is again assumed for absorption by multiple species in

the same spectral interval [*Francis et al.*, 1991; *Valero et al.*, 1989].

For the present application we assume isotropic reflectance at the surface and a solar albedo of 70%. The surface infrared emissivity is taken to be 0.98, and the calculations are performed once a day for the sun at local zenith (thus the calculations represent daily maximum values rather than daily averages). The model also requires vertical temperature and mixing ratio profiles, and these are obtained from stations surrounding the southern Kara Sea (on Novaya Zemlya to the west, Ostrov Vaygach to the south, and Ostrov Belyy to the east). These stations are located at approximately equal distances from the pixels used for the microwave samples, and the twice-daily radiosonde data are averaged for all three stations to produce the vertical profiles for the model. The cloud cover is estimated from the relative humidity profiles and compared with visible satellite imagery for 1984. The visible imagery are from the Defense Meteorological Satellite Program (DMSP) operational linescan system at 2.7-km resolution (similar imagery is not available for 1982). One hundred percent cloud cover is assumed to occur in any layer of the model that has 85% or greater relative humidity. Clouds are also included in the near-surface layers when the relative humidity is greater than 75% and is at least 40% greater than in the adjacent layers. Using these criteria, the presence or absence of clouds matches those observed in the visible imagery on about 93% of the days in 1984. Of the 3 of 45 days that do not match, all three images show low cloud over the ice that is not apparent in the soundings at the surrounding stations. The cloud physical properties used in the model are based on the observations of *Herman and Curry* [1984] for summer Arctic stratus clouds, using an effective drop size radius of 7.5 μm.

The surface fluxes computed from the radiative transfer model are shown in Figures 3 and 4. The seasonal trend is

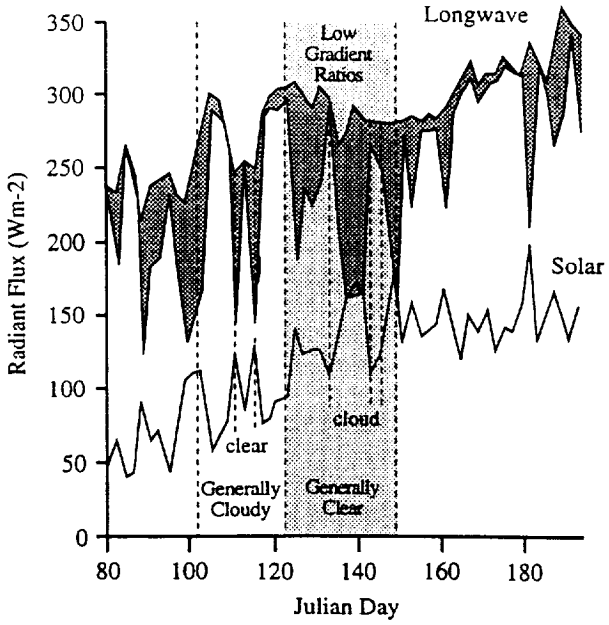

Figure 3. Radiation model results for 1982. The shaded regions correspond to the time period of strong negative gradient ratios. The upward longwave radiation is shown by the upper curve, and the shaded area gives the net longwave flux, which is usually negative (away from the surface).

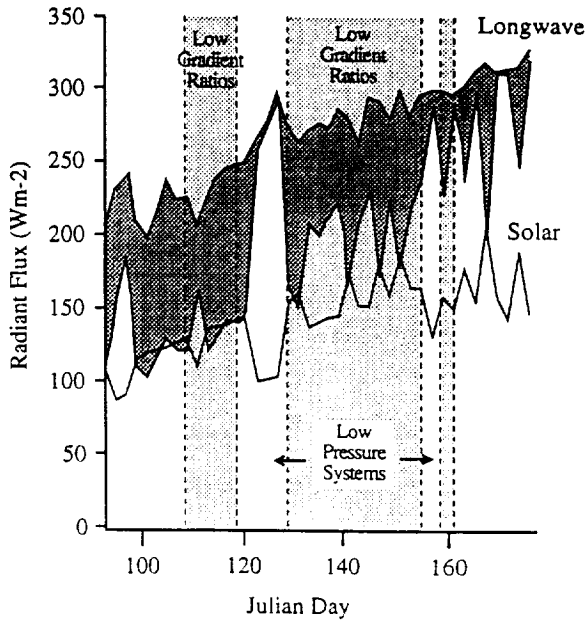

Figure 4. Radiation model results for 1984. The shaded regions correspond to the time periods of strong negative gradient ratios. The upward longwave radiation is shown by the upper curve, and the shaded area gives the net longwave flux, which is usually negative (away from the surface).

obvious in both years, with the absorbed solar radiation increasing throughout the spring and then leveling off during the summer months. The large daily to weekly variations are due to changes in cloud cover, and the nature of the cloud cover is reflected in the flux calculations. For example, the radiosonde profiles indicate that most of the 1982 cloud cover is low-level stratus; cloud temperatures are similar to surface temperatures, and the outgoing and incoming longwave fluxes at the surface are virtually equal. On clear-sky days when the absorbed solar radiation increases, the upward longwave flux shows little change, and there is a large decrease in the downward longwave flux at the surface. In 1984, on the other hand, there is an increased incidence of cyclonic systems and a greater frequency of thicker or multilayered clouds, and the cloud layer is generally cooler than the surface.

The premelt ice signature

Looking first at 1984 (Figure 2b), one observes a large drop in gradient ratios on day 128 (May 7) and a further drop from day 156 to 160 (June 4-8). The DMSP satellite imagery indicates cloud cover associated with low-pressure systems moving through the region at these times. The brightness temperatures (Figure 1b) reach a peak just prior to the first drop in gradient ratios, coinciding with the arrival of the low-pressure system and the advection of warm air over the region. The radiosonde data show that surface temperatures reach the melting point, and the combination of high temperatures and low-level cloud results in peak values of the longwave fluxes (Figure 4), with the upward and downward fluxes being approximately equal. The drop in brightness temperatures on day 128 coincides with a return to colder conditions as the low-pressure system moves out of the area. The negative gradient ratios are thus most likely to result from surface

grain size and surface roughness changes due to surface melt and freeze cycles over the preceding 4 days.

Synoptic conditions during the second drop in gradient ratios in early June follow essentially the same pattern. In this case, however, the drop in gradient ratios is followed by a rapid increase in positive ratios (indicative of open water) as ice breakup advances. Although it is not obvious, there is some indication of a slight drop in gradient ratios earlier in the spring, well before any surface melt occurs. A similar but much larger decrease in gradient ratios is found in spring 1982, and this requires a somewhat different interpretation.

Figure 2a shows that the large drop in the 1982 gradient ratios occurs after day 124 (May 4), and reaches a minimum on day 130 (May 10). The surface radiation budget indicates that the region was cloud covered from day 102 to day 122 (apart from two clear-sky days in the middle of the period). The net longwave flux during the premelt period was close to zero (Figure 3) except on the two clear days that had negative longwave budgets (upward IR > downward IR). The absorbed solar radiation was also generally low, with values of about 60-80 W m^{-2}. After day 122 and coincident with the drop in gradient ratios (Figure 2a), a reversal occurs. There is a period of generally clear skies with a few isolated days of cloud cover. The longwave budget is strongly negative, and analysis of the station data shows that the surface air temperatures are below freezing. It is reasonable to expect, therefore, that the surface temperature over the ice is also below freezing at this point. The absorbed solar radiation, however, doubles, with values ranging from 125 to 170 W m^{-2} (except for the cloudy days when values drop to about 105-110 W m^{-2}). These radiation budget calculations are discussed in relation to snow crystal growth calculations of *Colbeck* [1989a] and to observational studies done over the Greenland ice cap (*Alley et al.*, 1990]; taken together they suggest that the emissivity changes in this case are due to the formation of a near-surface depth hoar following solar radiation into the pack and warming of the upper layers of the snow cover.

The role of solar penetration in the formation of depth hoar is discussed by *Colbeck* [1989a], who calculates rates of snow crystal growth under various surface temperature conditions with a snow model that includes the effects of solar penetration. For both a seasonal snow cover and an alpine snowpack, he calculates that diurnal radiative and temperature forcing cause rapid crystal growth in the near-surface layer. The snow-covered sea ice in the Kara Sea is analogous to Colbeck's seasonal snowpack case, where the temperature at the soil/snow interface is held at 0°C, and crystal growth was calculated within a 1-m snowpack. In the present case, the radiation model shows that under clear-sky conditions the incoming solar radiation in the Kara Sea was within the ranges used by Colbeck for his model calculations. Colbeck, however, uses a 30°C diurnal temperature cycle, which is somewhat larger than would be likely over the sea ice. Colbeck also includes one polar example, for which he simulates conditions over a polar ice sheet. In this case, however, he assumes that a low value for radiative heating and depth hoar formation is linked to the annual temperature wave. The model shows penetrating radiation doubling the snow crystal growth rate at 20-cm depth over what would result from temperature cycling alone, but most of the crystal growth in the ice sheet model occurs in late summer and early fall. However, it has been shown that rapid depth hoar formation can also occur over polar ice much earlier in the summer [*Alley et al.*, 1990].

Measurements taken on Greenland in the summer of 1990 show a 5- to 10-mm-thick depth hoar forming under clear-sky conditions in less than 24 hours [*Alley et al.*, 1990]. This occurred at a depth of about a centimeter, where the solar loading caused a local temperature rise of several degrees compared to the temperature of the adjacent snow and air layers. The depth hoar formed in mid-June with maximum air temperatures well below freezing (-8°C). The observed temperature gradient was sufficient to cause a net vapor movement out of the depth hoar, the diffusive mass flux alone accounting for the removal of an estimated 100 kg/m^3 from the depth hoar layer over a 3- to 5-day period. Given also the possibility of wind pumping [*Clarke et al.*, 1987; *Colbeck*, 1989b] and thermal convection [*Johnson et al.*, 1987], *Alley et al.* [1990] conclude that the energy available was sufficient to explain the observed density loss in terms of solar warming of the near-surface layer.

The reasons for the springtime emissivity changes in the Kara Sea cannot be proven unambiguously without in situ observations; the brightness temperature changes and the radiation model results, however, are consistent with the suggestion that the emissivity changes may be due to the formation of a near-surface depth hoar as a result of solar heating of the snowpack. The radiation budget calculations show that the surface longwave budget is negative, as is the sensible heat flux implied by the temperature profile. The only energy input to the surface is the incoming solar radiation, with the levels of penetrating radiation being within the ranges used by *Colbeck* [1989a] to demonstrate hoar formation in a seasonal snowpack. The penetrating radiation heats the near-surface layer and amplifies the diurnal temperature gradient, and the resulting mass flux causes a growth in snow crystal size. This increases the microwave scatter and reduces emissivity, with the change being frequency dependent (i.e. the scatter is a function of frequency in relation to crystal size; see, for example, *Chang et al.*, [1976, 1982]). The increased scatter at 37 GHz results in a more negative gradient ratio.

Scattering in the snowpack is also polarization dependent and tends to be greater for horizontal polarizations [e.g., *Mätzler*, 1987]. Calculations of 37V - 37H are also presented in Figure 2. These show that the drop in gradient ratios is matched by an increase in the 37V - 37H difference, which further supports the suggestion that these brightness temperature changes result from a scattering effect. Why these regions of negative gradient ratios in the SSIZ should expand and then disappear is not clear. One possibility is that the near-surface layers, where the depth hoar occurs, may be further disturbed by wind action that would break down the layer and reduce the 37-GHz and 18-GHz brightness temperature differences.

Conclusions

SMMR-derived measurements over the first-year-ice region of the southern Kara Sea in spring 1982 and 1984 reveal areas of negative brightness temperature ratios that appear suddenly, persist for a couple of weeks, and then disappear. The gradient ratios in this case are calculated as the difference between the 37-GHz and 18-GHz vertically polarized brightness temperatures, and the negative ratios occur because of a sudden drop in brightness temperature at 37 GHz. These signatures are similar to occurrences reported during the early spring in other years and in other regions of the seasonal sea

ice zone [*Anderson*, 1987]. Previous studies have shown that these regions are the first to exhibit snow and ice melt later in the spring, and these signatures are interpreted as representing the initial transition from winter to summer ice conditions.

The negative gradient ratios in 1982 occur in association with clear skies and below-freezing temperatures. Calculations of the surface radiation budget for these time periods show that the longwave flux is negative and that the only energy input to the snow surface results from incoming solar radiation (the radiosonde data indicate that the sensible heat flux would also be negative). Our conclusion is that the negative ratios represent areas of depth hoar in the near-surface layers that form as a consequence of solar heating. The growth in crystal size increases the scatter and reduces emission in the 37-GHz channel, giving rise to the negative gradient ratios. For 1984 the radiation budget calculations show the possibility of surface melt and the formation of increased grain sizes and increased surface roughness following several days of freeze-thaw cycling. Why these signatures then disappear is unclear, but their disappearance may be due to further surface disturbance by wind action or precipitation.

Although the processes that give rise to the snow emissivity changes appear to be different in the two years, the significant fact is that in both years the microwave signal is regional and occurs as a response to changes in atmospheric temperature, cloud cover, and surface radiation budget. It is well known that ice retrievals are complicated in the summer by the emissivity change that accompanies the increase in liquid water in the pack. However, these results indicate that emissivity changes, which may introduce some error into the ice cover calculations, are also occurring much earlier in the spring and that the spatial and temporal distributions of these changes will be highly variable as a response to the synoptic-scale atmospheric circulation.

Acknowledgments. This work was supported by NASA grants NAGW-1042 to Robert Crane at The Pennsylvania State University and NAGW-1266 to Mark Anderson at the University of Nebraska. The SMMR gridded brightness temperature data on CD-ROM produced by P. Gloersen were obtained from the National Snow and Ice Data Center, Boulder, Colorado. We would like to acknowledge the helpful comments made on an earlier draft of the paper by the editor and two anonymous referees.

References

Alley, R. B., E. S. Saltzman, K. M. Cuffey, and J. J. Fitzpatrick, Summertime formation of depth hoar in central Greenland, *Geophys. Res. Lett. 17*, 2393-2396, 1990.

Anderson, M. R., The onset of spring melt in first-year ice regions of the Arctic as determined from scanning multichannel microwave radiometer data for 1979 and 1980, *J. Geophys. Res.*, 92(C12), 13,153-13,163, 1987.

Anderson, M. R., and D. A. Robinson, Snow melt on Arctic sea ice in 1979 and 1980 from microwave and shortwave satellite data, *Eos Trans. AGU, 66*(46), 824, 1985.

Barry, R. G., Arctic Ocean ice and climate: Perspective on a century of polar research, *Ann. Assoc. Am. Geogr., 73*, 485-501, 1983.

Cavalieri, D. J., P. Gloersen, and W. J. Campbell, Determination of sea ice parameters with the Nimbus 7 SMMR, *J. Geophys. Res., 89*(D4), 5355-5369, 1984.

Chang, A. T. C., J. L. Foster, D. K. Hall, A. Rango, and B. K. Hartline, Snow water equivalent estimation by microwave radiometry, *Cold Reg. Sci. Technol., 5*, 259-267, 1982.

Chang, T. C., P. Gloersen, T. Schmugge, T. T. Wilheit, and H. J. Zwally, Microwave emission from snow and glacier ice, *J. Glaciol., 16*, 23-39, 1976.

Clarke, G. K. C., D. A. Fisher, and E. D. Waddington, Wind pumping: A potentially significant heat source in ice sheets, *Publ. 170*, pp. 169-180, Int. Assoc. for Hydrol. Sci., Gentbrugge, Belgium, 1987.

Colbeck, S. C., Snow crystal growth with varying surface temperatures and radiation penetration, *J. Glaciol., 35*, 23-39, 1989a.

Colbeck, S. C., Air movement in snow due to windpumping, *J. Glaciol., 35*, 209-213, 1989b.

Crane, R. G., and M. R. Anderson, Spring melt patterns in the Kara/Barents Sea: 1984, *GeoJournal, 18*, 25-33, 1989.

Crane, R. G., R. G. Barry, and H. J. Zwally, Analysis of atmosphere-sea ice interactions in the Arctic Basin using ESMR microwave data, *Int. J. Remote Sens.*, 3, 259-276, 1982.

Dickinson, R. E., G. A. Meehl, and W. M. Washington, Ice-albedo feedback in a CO^2-doubling simulation, *Clim. Change, 10*, 241-248, 1987.

Francis, J. A., T. P. Ackerman, K. B. Katsaros, R. J. Lind, and, K. L. Davidson, A comparison of radiation budgets in the Fram Strait summer marginal ice zone, *J. Clim., 4*, 218-235, 1991.

Gloersen, P., and D. J. Cavalieri, Reduction of weather effects in the calculation of sea ice concentration from microwave radiances, *J. Geophys. Res., 91*(C3), 3913-3919, 1986.

Hanson, A., The snow cover of sea ice during the Arctic Ice Dynamics Joint Experiment 1975-1976, *Arct. Alp. Res., 12*, 215-226, 1980.

Herman, G. F. and J. A. Curry, Observational and theoretical studies of solar radiation in Arctic stratus clouds, *J. Clim. Appl. Meteorol., 23*, 5-24, 1984.

Johnson, J. B., M. Sturm, D. K. Perovich, and C. S. Benson, Field observations of thermal convection in a subarctic snow cover, *Publ. 162*, pp. 105-118, Int. Assoc. for Hydrol. Sci., Gentbrugge, Belgium, 1987.

Ledley, T. S., Snow on sea ice: Competing effect in shaping climate, *J. Geophys. Res., 96*(D9), 17,195-17,208, 1991.

Livingstone, C. E., K. P. Singh, and A. L. Gray, Seasonal and regional variations of active/passive microwave signatures of sea ice, *IEEE Trans. Geosci. Remote Sens., GE-25*, 159-173, 1987.

Mätzler, C., Application of the interaction of microwaves with the natural snowcover. *Remote Sens. Rev., 2*, 259-387, 1987.

Robinson, D. A., G. Scharfen, M. C. Serreze, G. Kukla, and R. G. Barry, Snow melt and surface albedo in the Arctic Basin, *Geophys. Res. Lett., 13*(9), 945-948, 1986.

Robinson, D. A., M. C. Serreze, R. G. Barry, G. Scharfen, and G. Kukla, Large-scale patterns and variability of snow melt and parameterized surface albedo in the Arctic Basin, *J. Clim., 5*, 1109-1119, 1992.

Shine, K. P., and R. G. Crane, The sensitivity of a one-dimensional thermodynamic sea ice model to changes in cloudiness, *J. Geophys. Res., 89*(C6), 10,615-10,622, 1984.

Shine, K. P., and A. Henderson-Sellers, The sensitivity of a thermodynamic ice model to changes in surface albedo parameterization, *J. Geophys. Res., 90*(D1), 2243-2250, 1985.

Stiles, W. H. and F. T. Ulaby, The active and passive response to snow parameters, 1, Wetness, *J. Geophys. Res., 85*(C2), 1037-1044, 1980.

Valero, F. P. J., T. P. Ackerman, and W. J. Y. Gore, The effects of the Arctic haze as determined from airborne radiometer measurements during AGASP II, *J. Atmos. Chem., 9*, 225-244, 1989.

Zwally, H. J., and P. Gloersen, Passive microwave images of the polar regions and research applications, *Polar Rec., 18*, 431-450, 1977.

M. R. Anderson, Department of Geography, University of Nebraska, Lincoln, NE 68588-0135. (e-mail: manderson@-crcvms.unl.edu)

R. G. Crane, College of Earth and Mineral Sciences, 103 Deike Building, The Pennsylvania State University, University Park, PA 16802-2710. (e-mail: crane@essc.psu.edu)

(Received September 25, 1992; revised September 1, 1993; accepted February 7, 1994.)

Annals of Glaciology 17 1993
© International Glaciological Society

Passive microwave-derived spatial and temporal variations of summer melt on the Greenland ice sheet

THOMAS L. MOTE, MARK R. ANDERSON, KARL C. KUIVINEN AND CLINTON M. ROWE
Department of Geography, University of Nebraska–Lincoln, Lincoln, NE 68588-0135, U.S.A.

ABSTRACT. Passive microwave-brightness temperatures over the Greenland ice sheet are examined during the melt season in order to develop a technique for determining surface-melt occurrences. Time series of Special Sensor Microwave/Imager (SSM/I) data are examined for three locations on the ice sheet, two of which are known to experience melt. These two sites demonstrate a rapid increase in brightness temperatures in late spring to early summer, a prolonged period of elevated brightness temperatures during the summer, and a rapid decrease in brightness temperatures during late summer. This increase in brightness temperatures is associated with surface snow melting. An objective technique is developed to extract melt occurrences from the brightness-temperature time series. Of the two sites with summer melt, the site at the lower elevation had a longer period between the initial and final melt days and had more total days classified as melt during 1988 and 1989. The technique is then applied to the entire Greenland ice sheet for the first major surface-melt event of 1989. The melt-zone signal is mapped from late May to early June to demonstrate the advance and subsequent retreat of one "melt wave". The use of such a technique to determine melt duration and extent for multiple years may provide an indication of climate change.

INTRODUCTION

Climate theory predicts, and climate models generally confirm, that temperature changes due to increased concentrations of radiatively active gases in the atmosphere will be greatest in high northern latitudes. Furthermore, a decrease in snow and ice cover in the Arctic may amplify any global warming by reducing the surface albedo and allowing Earth to absorb more solar radiation. Greater evaporation associated with increased temperatures in the Arctic may also lead to increased atmospheric moisture available for precipitation. In particular, the Greenland ice sheet may experience more accumulation due to increased atmospheric moisture and more ablation due to increased temperatures. An earlier and longer melt occurrence or greater spatial extent of surface melt should evidence an increase in the ice sheet's ablation. Therefore, surface melt could serve as a sensitive indicator of climate change. However, knowledge of the spatial and temporal extent of melt for the Greenland ice sheet is incomplete, in part due to the limited areal extent of surface observations spanning the onset and duration of summer melt.

Satellite remote sensing offers a means of measuring and monitoring the extent of surface melt on the Greenland ice sheet. In particular, microwave-brightness temperatures exhibit a distinct increase during surface melt. This peak in microwave emission stands in sharp contrast to the lower brightness temperatures observed under non-melt conditions for Greenland and Antarctica (Gloersen and others, 1974). The rapid increase in brightness temperatures results from changing surface-snow conditions. It is well known that the emissivity of snow changes rapidly with melt, largely due to an increase in the water content of the snow (Chang and others, 1976; Rango and others, 1979; Foster and others, 1984; Chang and others, 1985). While snow density, temperature, crystal structure and crystal size all contribute to the snowpack's emissivity, changes in the volumetric water content produce the most prominent changes in brightness temperatures.

As the snowpack melts, liquid water forms between the individual snow grains, which increases the absorption and decreases the volume scattering (Rango and others, 1979). The surface scattering is enhanced over the volume scattering by two orders of magnitude (Mätzler and others, 1984). The result is a substantial increase in the emissivity of the snow. Snow with 1–2% liquid-water content may produce 37 GHz brightness temperatures 50 K higher than dry snow (Hofer and Mätzler, 1980). Experimental work has been conducted to describe the relationship between liquid-water content and microwave-brightness temperatures. Stiles and Ulaby (1980) empirically fit an exponential function of the form:

$$T_B(m_v) = A - Be^{-cm_v} \quad (1)$$

where T_B = microwave-brightness temperature and m_v = liquid water content, for liquid-water content between 0 and 6%. The greatest increase in brightness temperatures occurs from snow with 0.5–1% liquid-water

content (Stiles and Ulaby, 1980). This conspicuous signal and its usefulness as an indicator of climate variability, and thus climate change, has led to repeated calls for scientists to map the melt zones of the ice sheets (Zwally, 1977; Thomas, 1991).

The availability of more than a decade of passive microwave data now provides a viable method of mapping the melt zone and observing the intra- and inter-annual variability of surface melt. This paper examines time series of passive microwave data during the melt season for locations within the wet- and dry-snow zones of the ice sheet. From the time series, an objective technique for determining surface melt is developed. This technique is used to map the melt-zone signal as it advances across the ice sheet during the late spring of 1989.

MICROWAVE DATA

Passive microwave data used to determine the melt zone were acquired from the Special Sensor Microwave/Imager (SSM/I), a second-generation multichannel microwave radiometer. The SSM/I records radiation in seven channels, the vertical and horizontal polarizations for 19.35 GHz (1.55 cm), 37.0 GHz (0.81 cm) and 85.5 GHz (0.35 cm) and the vertical polarization for 22.235 GHz (1.35 cm). The first SSM/I, launched on 19 June 1987, has a sun-synchronous, near-polar orbit with an altitude of 883 km, a swath width of 1400 km and a view angle of 53.1° (Hollinger and others, 1987).

The SSM/I data used in this study, from July 1987 to June 1990, were obtained from the National Snow and Ice Data Center's (NSIDC) archive of brightness temperature grids on compact disc. The 19 and 37 GHz data used in this investigation have been binned by NSIDC into a 25 km × 25 km grid. The binning process averages all observations that fall within the grid cell for each day, midnight to midnight UTC (National Snow and Ice Data Center, 1992). The coastal mask supplied with the SSM/I data was applied to eliminate pixels containing both land and water. However, pixels along the ice-sheet edge that contain land or both land and ice have not been removed from the data.

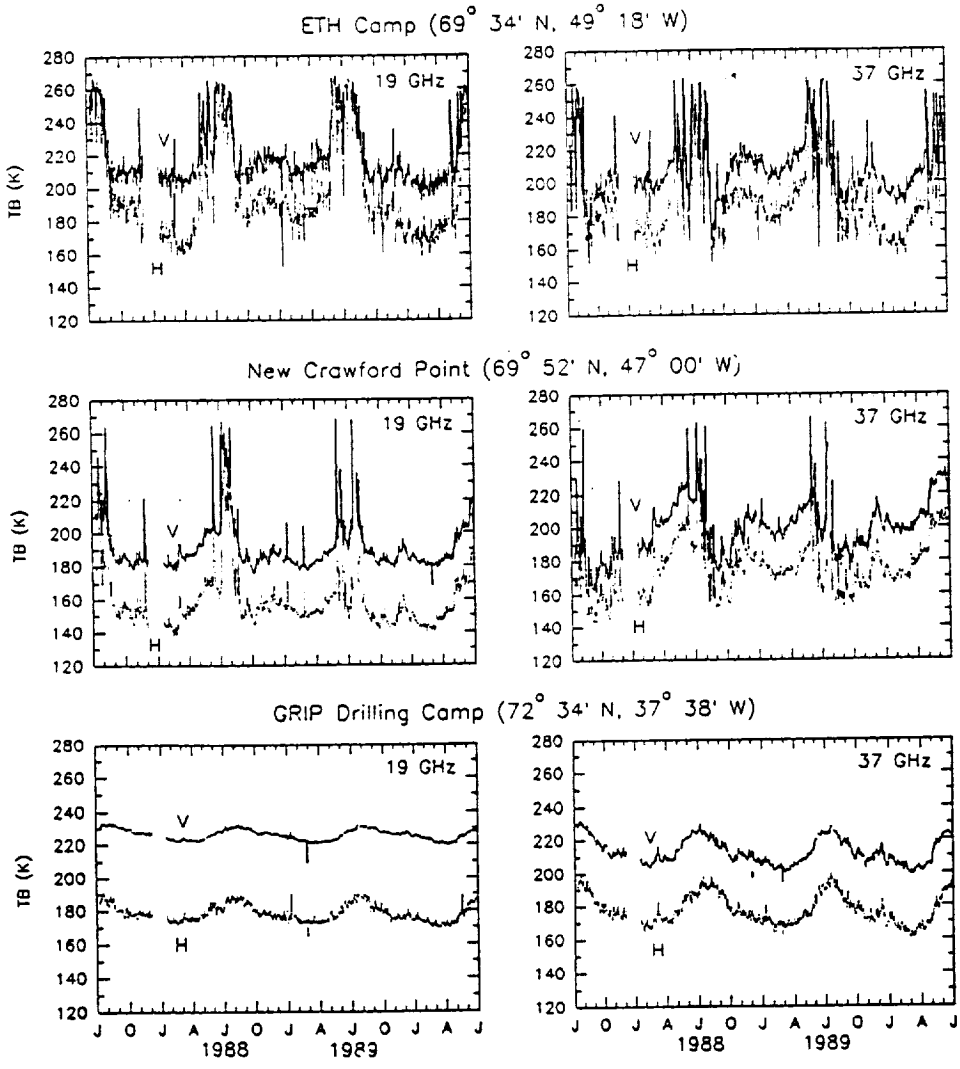

Fig. 1. Microwave-brightness temperature time series of the vertically and horizontally polarized channels at 19 and 37 GHz for three locations on the Greenland ice sheet.

EXAMINATION OF MICROWAVE MELT SIGNAL

To develop an understanding of surface melt as identified by passive microwave data, time series of SSM/I microwave-brightness temperatures were produced for three locations on the ice sheet. The locations were selected from previously occupied research sites: the Swiss Federal Institute of Technology (ETH) camp (69°34′ N, 49°18′ W; 1175 m a.s.l.), NASA's camp at New Crawford Point (69°52′ N, 47°00′ W; 1879 m a.s.l.) and the European GRIP deep ice-core drilling camp (71°34′ N, 37°38′ W; 3230 m a.s.l.). The ETH camp is of particular interest because published data on snowpack characteristics at that location by Ohmura and others (1991) overlap the available microwave data by one month, allowing some limited comparison.

The GRIP drilling camp, near the summit of the ice sheet, lies in the dry-snow zone and is generally believed never to experience surface melt. However, the ETH camp lies near the equilibrium line and New Crawford Point lies in the percolation zone; accordingly, both sites are subject to summer surface melt. New Crawford Point experiences a rapid change from the dry-snow condition of winter to the percolation of melt water during the summer, but no melt ponds formed during surface observations in June and August 1991 (personal communication from K. Jezek). At the ETH site, supraglacial lakes were observed during the summer of 1990. Surface drainage channels formed, and surface lakes filled with water by late June (Laternser, 1991).

Under the assumption that these sites are representative of wet- and dry-snow zones, time series of brightness temperatures for four channels (19V/H, 37V/H) were constructed from three years of SSM/I data (Fig. 1). These time series were examined for differences between microwave signals from locations with and without summer melt.

The most prominent features in the time series for the ETH and New Crawford Point sites are the rapid increases in brightness temperatures during late spring to early summer, the prolonged period of elevated brightness temperatures during the summer, and the rapid decrease in brightness temperatures during late summer (Fig. 1). For example, the 19V brightness temperatures for the ETH site demonstrate a rapid decline in August 1987 from values around 260 K in the summer to approximately 210 K during the winter. A rapid increase in the brightness temperatures occurs at the end of May 1988 and continues through the summer with a subsequent decline in August. This pattern is repeated for the remainder of the time series and a comparable pattern is observed in the 19H channel.

Similar transitions between seasons are observed in the vertical and horizontal 37 GHz brightness temperatures, although greater variability is present within each season for these channels. Most of the gradual increase in brightness temperatures throughout the spring is probably the result of increasing snowpack temperatures. However, examination and discussion of the smaller-scale variability is beyond the scope of this paper.

Large variations are also observed in the brightness temperatures for the New Crawford Point site (Fig. 1), though the summer plateaus are not as prolonged as those observed at the ETH site. The highest summer brightness temperatures are similar at the ETH and New Crawford Point sites. Other locations on the ice sheet had brightness temperatures near 273 K, which result from the emissivity of near unity for wet snow with a volumetric water content greater than 2%. Maximum brightness temperatures of approximately 260 K for the ETH and New Crawford sites during surface melt result from an emissivity of less than one and may be a result of liquid-water content between 0.5 and 2%, in addition to any remaining dry snow within the foot print of the sensor.

Although no rapid changes or periods of elevated brightness temperatures occur during the three-year period for the GRIP drilling site as was observed for the ETH or New Crawford Point sites (Fig. 1), the annual temperature cycle is clearly present in the brightness-temperature time series. The seasonal variation in temperature is more pronounced in the 37 GHz channels than the 19 GHz channels. For example, exclusive of the melt period, the 19V brightness temperatures range from 220 to 235 K, whereas the 37V brightness temperatures range from 200 to 230 K. This is likely due to the fact that radiation received at 19 GHz emanates from a deeper and more thermally stable layer of the snowpack than radiation at 37 GHz.

OBJECTIVE MELT DETERMINATION

In order to catalogue melt onset, duration and accumulated melt days objectively, one channel was selected to identify the brightness temperature peak. The goal in selecting that channel was to minimize the within-melt variance of the brightness temperatures and maximize the melt–non-melt difference. The brightness temperature time series for the ETH site was used to determine means and standard deviations (Table 1) separately for a winter period (1 December 1988–28

Table 1. Means and standard deviations of brightness temperatures for the ETH site

	19V	*19H*	*37V*	*37H*
1 December 1988 – 28 February 1989				
Mean	214.2	186.5	210.1	184.3
S.D.	5.9	7.8	5.6	6.8
1 June 1989 – 31 July 1989				
Mean	255.1	237.8	234.5	221.1
S.D.	10.0	12.7	23.8	24.9

February 1989) and a melt period (1 June 1989–31 July 1989). The 19V channel demonstrates the greatest difference of the means between winter and the summer melt (41 K) and has the smallest standard deviation during the melt (10 K). Therefore, the 19V channel was selected to serve as an indicator of melt.

The difference between the 19V summer and winter means was used as the basis to determine the melt threshold for two reasons. First, the differencing technique accounts for observed variations in brightness temperatures across the ice sheet prior to the onset on summer melt. Secondly, employing this difference aids in eliminating coastal land contamination due to the smaller variation in brightness temperatures for land surfaces than for snow and ice surfaces. A threshold of 31 K above the winter mean was derived by subtracting one standard deviation of the melt-period brightness temperatures from the difference in means. This was done to avoid indicating a return to non-melt conditions due to the smaller-scale variations observed during the melt period.

MELT FEATURES

The brightness temperature threshold of 31 K above the winter mean is used to identify melt periods for the ETH camp and New Crawford Point for the three years of available SSM/I data. Any day with a brightness temperature greater than the threshold was classified as melt. The length of melt, or melt season, can then be determined by the number of days between the first observation above the threshold and the last day above the threshold.

Table 2. Melt dates between 10 July 1987 and 30 June 1990 from SMM/I data for the ETH and New Crawford Point sites

	ETH Camp		*New Crawford Point*	
	Begin	*End*	*Begin*	*End*
1987		15 Aug		23 Jul
1988	15 May	17 May	9 Jun	13 Jun
	28 May	30 May	4 Jul	5 Aug
	9 Jun	16 Jun		
	29 Jun	3 Aug		
	6 Aug	21 Aug		
1989	30 May	30 Jun	30 May	2 Jun
	4 Jul	13 Aug	9 Jun	13 Jun
	17 Aug	19 Aug	14 Jul	27 Jul
1990	7 May	9 May	20 Jun	26 Jun
	29 May	1 Jun		
	8 Jun	12 Jun		
	16 Jun			

In 1988 and 1990, the first day above the threshold, the melt onset, occurred earlier at the grid cell containing the ETH site than at the New Crawford Point grid cell (Table 2). However, during 1989 the melt onset occurred on 30 May at both grid cells. The ending date for the melt season occurred on different dates for the two sites each year. In general, the last day of melt for the New Crawford Point grid cell is 20 d earlier than for the ETH site (Table 2). The earlier onset and later ending date resulted in a longer melt season for the ETH site than for the New Crawford Point site. The 1988 melt season lasted 99 d at the ETH site and 58 d at the New Crawford Point site. The 1989 melt season lasted 82 d at the ETH site and 59 d at the New Crawford Point site. The difference in the length of the melt season between the two grid cells is likely related to the elevation difference between the two locations.

During the melt season, the brightness temperatures fall below the threshold value on a number of days. This implies that the total length of the melt season may not fully characterize the duration of surface melt for each grid cell. Therefore, the total number of days classified as melt during each season, referred to here as the number of accumulated melt days, is also determined for the two sites. During both 1988 and 1989, the ETH site had more accumulated melt days than New Crawford Point. The ETH site had 76 melt days as opposed to 38 for the New Crawford Point in 1988 and 66 melt days as opposed to 23 for New Crawford Point in 1989. For the two years examined, a large inter-annual variability exists for both sites.

During June 1990, simultaneous daily ground observations were available for the ETH site (Greuell and Konzelmann, 1991). This overlap permits a comparison between the microwave-brightness temperatures and several surface parameters, particularly the water content of the snow. Due to the coarse resolution of the microwave grid, some caution must be exercised in relating the microwave data to surface observations. Nevertheless, there is close agreement between onset of the first continuous microwave peak and the published data on mean liquid-water content of the snowpack. The first continuous peak in emission for 1990 begins on 16 June, the same day the liquid-water content at the ETH camp was first reported greater than 2%. The microwave-brightness temperatures continued to rise until 24 June. Concurrently, the reported volumetric water content increased until it reached a June peak of 5.51% on 23 June (Greuell and Konzelmann, 1991). This comparison supports the conclusion that the volumetric water content of the snowpack is the dominant factor in the microwave signature during melt and therefore can be used to identify melt. Two 4 d peaks and one 5 d peak are evident in the time series between mid-May and early June, before the period of continuous summer melt. These shorter-lived peaks are likely due to radiation melting of the surface. Greuell and Konzelmann (1991) reported evidence of surface melting at the ETH camp as early as 24 May but no measurements of snow properties are available for May.

To assess the usefulness of the objectively determined threshold, the 31 K difference threshold was applied to each grid cell over Greenland to map the advance and

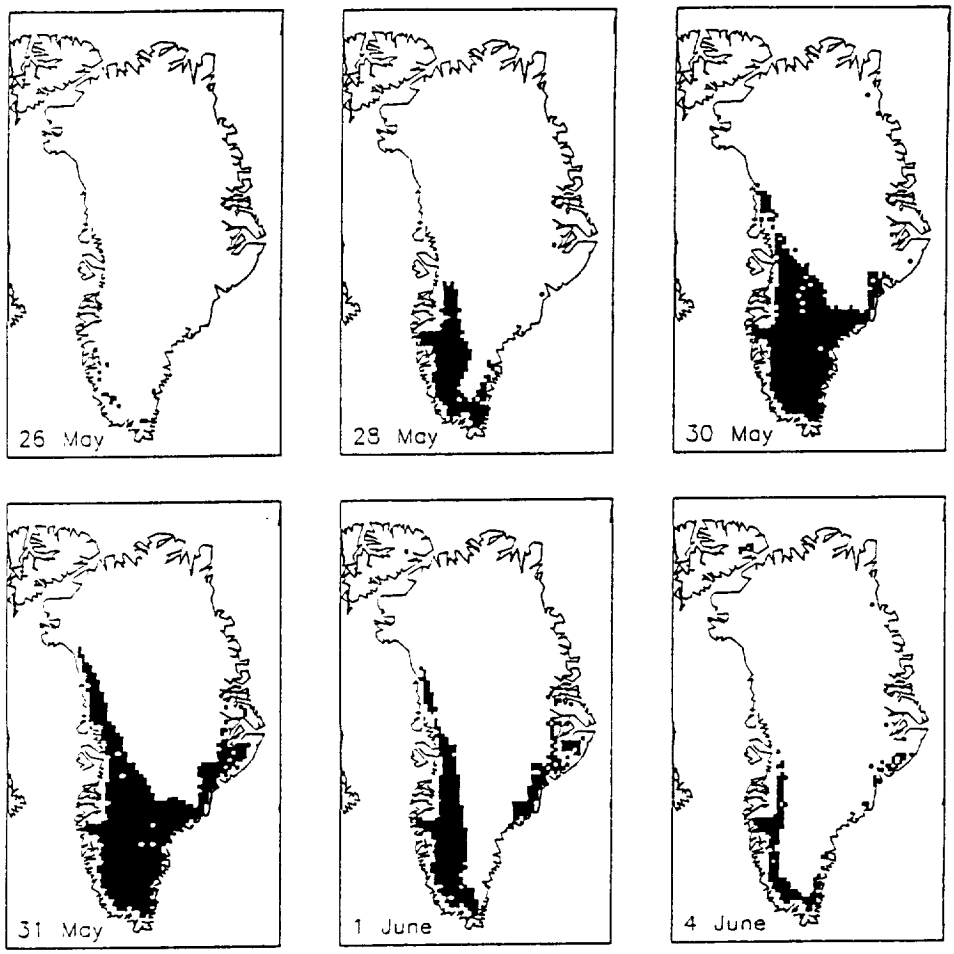

Fig. 2. Microwave-derived surface melt extent (in black) during the first major surface melt event of 1989.

retreat of one "melt wave" during late May and early June 1989. To display the spatial extent of melt, difference maps were produced using individual summer images and the 20 January 1989 image, which served as a proxy for the mean winter conditions across the entire ice sheet. Zhang and others (1989) have shown that microwave-brightness temperatures are stable throughout winter across the Greenland ice sheet; thus, a single winter image can provide a first approximation to the mean winter conditions. If the summer–winter difference for an individual grid cell exceeded 31 K, the cell was classified as experiencing melt.

A sequence of six melt-extent maps, concentrating on the period of rapid increase in melt during late May 1989, was produced (Fig. 2). The 26 May map shows only isolated grid cells in the southwestern part of the ice sheet classified as experiencing surface melt. The number of grid cells classified as melt dramatically increased between 28 and 30 May. By 30 May, the entire southern dome and much of the western edge of the ice sheet were classified as experiencing surface melt. The number of grid cells classified as melting began to decline through the last image on 4 June, when only the periphery of the ice sheet remained classified as melting. As expected, the melt advance approximately followed the elevation contours of the ice in southern Greenland due to the dependence of temperature on elevation. This agrees with the dependence of melt on elevation evident in the comparison of brightness-temperature time series for the ETH and New Crawford Point sites.

SUMMARY AND CONCLUSIONS

Time series of SSM/I data for two sites in the wet-snow zone demonstrate a rapid increase in brightness temperatures during late spring to early summer, a prolonged period of high brightness temperatures during the summer and a rapid decrease in late summer. Previous research on the microwave emission of snow as well as knowledge of the surface conditions at the two sites suggests that the peaks are associated with melting of surface snow.

A threshold based on a comparison of summer and winter time series was developed to classify melt events. This technique was applied to the two wet-snow sites, and it classified a longer and more continuous melt season at the ETH camp, the lower elevation site, than the New Crawford Point site. Additionally, corresponding surface and microwave observations during June 1990 seem to demonstrate a relationship between the volumetric water content of the snowpack and the increase in brightness

temperature. Earlier, short-lived peaks that are evident in the time series cannot be attributed directly to increases in the liquid-water content due to a lack of concurrent surface observations. These peaks may be due to localized radiation melting of the top snow layer.

An objective technique to determine melt was applied to the entire ice sheet for a 10 d period in late May and early June 1989. The results demonstrate a rapid melt advance across the ice sheet, approximately following elevation contours.

Further refinement of the technique for determining melt events from passive microwave data is warranted. This refinement process should involve co-ordinated surface and satellite observations. Additionally, the small-scale variability evident in the time series needs further examination. Following additional refinements, Scanning Multichannel Microwave Radiometer (SMMR) and Electronically Scanning Microwave Radiometer (ESMR) data could be employed to provide a sufficiently long time series to map the inter-annual variability of melt extent on the ice sheet. This should prove a valuable addition to the effort to understand climate variability and, possibly, to detect climate change.

ACKNOWLEDGEMENTS

This work was partially supported by NASA grant NAGW-1266. The SSM/I gridded brightness-temperature data on CD-ROM were obtained from the National Snow and Ice Data Center, Boulder, Colorado, U.S.A.

REFERENCES

Chang, T. C., P. Gloersen, T. Schmugge, T. T. Wilheit and H. J. Zwally. 1976. Microwave emission from snow and glacier ice. *J. Glaciol.*, **74**(16), 23–39.

Chang, A. T. C., J. L. Foster, M. Owe, D. K. Hall and A. Rango. 1985. Passive and active microwave studies of wet snowpack properties. *Nord. Hydrol.*, **16**(2), 57–66.

Foster, J. L., D. K. Hall, A. T. C. Chang and A. Rango. 1984. An overview of passive microwave snow research results. *Rev. Geophys. Space Phys.*, **22**(2), 195–208.

Gloersen, P., T. T. Wilheit, T. C. Chang, W. Nordberg and W. J. Campbell. 1974. Microwave maps of the polar ice of the Earth. *Bull. Am. Meteorol. Soc.*, **55**(12), 1442–1448.

Greuell, W. and T. Konzelmann. 1991. Mass budget. *In ETH Greenland Expedition. Progress Report No. 1: April 1990 to February 1991.* Zürich, Swiss Federal Institute of Technology, 83–93.

Hofer, R. and C. Mätzler. 1980. Investigations on snow parameters by radiometry in the 3- to 60-mm wavelength region. *J. Geophys. Res.*, **85**(C1), 453–460.

Hollinger, J., R. Lo, G. Poe, R. Savage and J. Peirce. 1987. *Special sensor microwave/imager user's guide.* Washington, DC, Naval Research Laboratory.

Laternser, M. 1991. Surface morphology. *In ETH Greenland Expedition. Progress Report No. 1: April 1990 to February 1991.* Zürich, Swiss Federal Institute of Technology, 17–20.

Mätzler, C., H. Aebischer and E. Schande. 1984. Microwave dielectric properties of surface snow. *IEEE J. Oceanic Eng.*, **OE-9**(5), 366–371.

National Snow and Ice Data Center. 1992. *DMSP SSM/I brightness temperature grids for the polar regions on CD-ROM. User's guide.* Boulder, CO, University of Colorado. Cooperative Institute for Research in Environmental Sciences.

Ohmura, A. *and 8 others.* 1991. *ETH Greenland Expedition. Progress Report No. 1: April 1990 to February 1991.* Zürich, Swiss Federal Institute of Technology.

Rango, A., A. T. C. Chang and J. L Foster. 1979. The utilization of spaceborne microwave radiometers for monitoring snowpack properties. *Nord. Hydrol.*, **10**(1), 25–40.

Stiles, W. H. and F. T. Ulaby. 1980. The active and passive microwave response to snow parameters. 1. Wetness. *J. Geophys. Res.*, **85**(C2), 1037–1044.

Thomas, R. H. 1991. *Polar research from satellites.* Washington, DC, Joint Oceanographic Institutions, Inc.

Zhang, H., L. Tondal Pedersen and P. Gudmandsen. 1989. Microwave brightness temperatures of the Greenland ice sheet. *Adv. Space Res.*, **9**(1), 277–287.

Zwally, H. J. 1977. Microwave emissivity and accumulation rate of polar firn. *J. Glaciol.*, **18**(79), 195–215.

The accuracy of references in the text and in this list is the responsibility of the authors, to whom queries should be addressed.